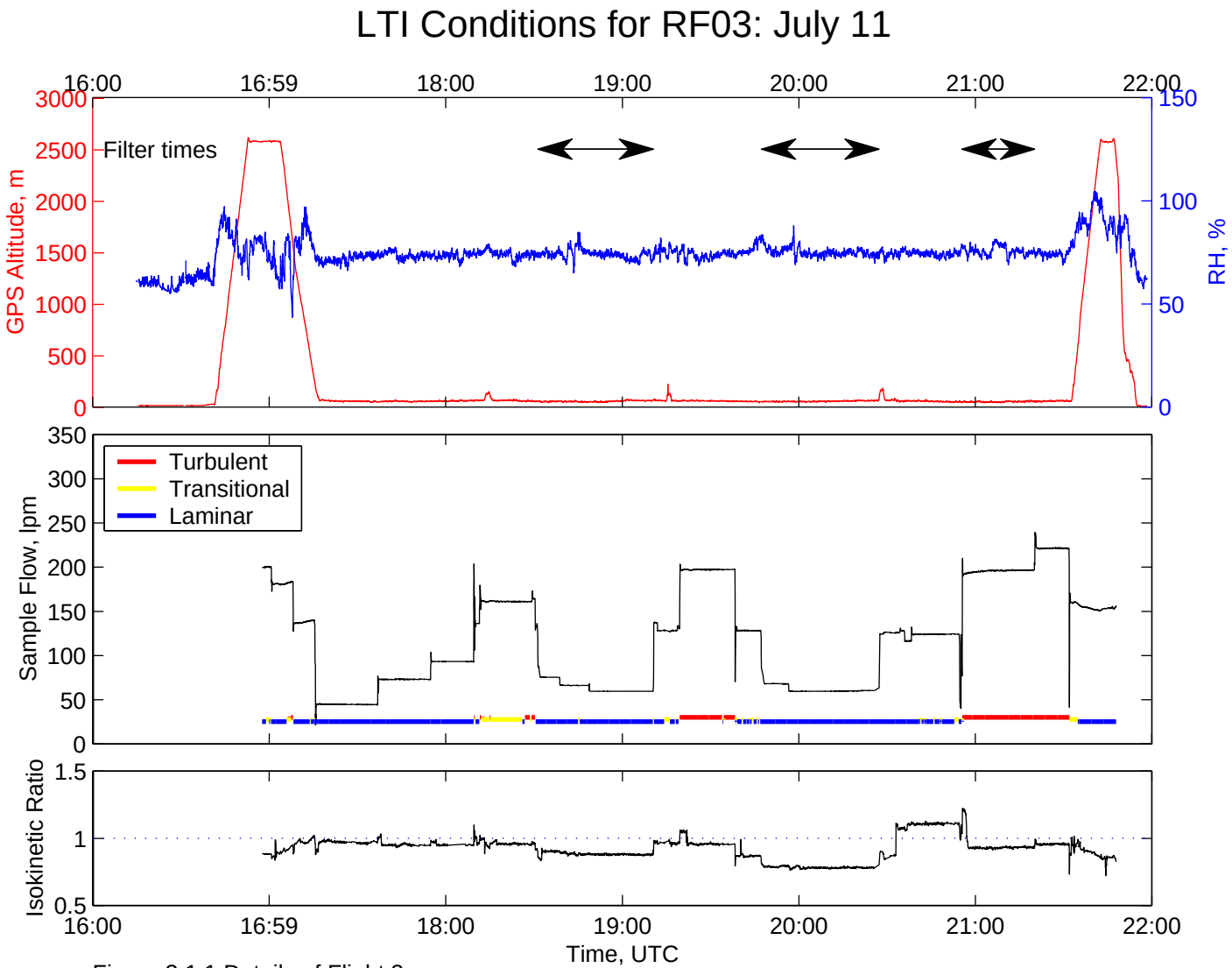

Figure 3.1.1 Details of Flight 3

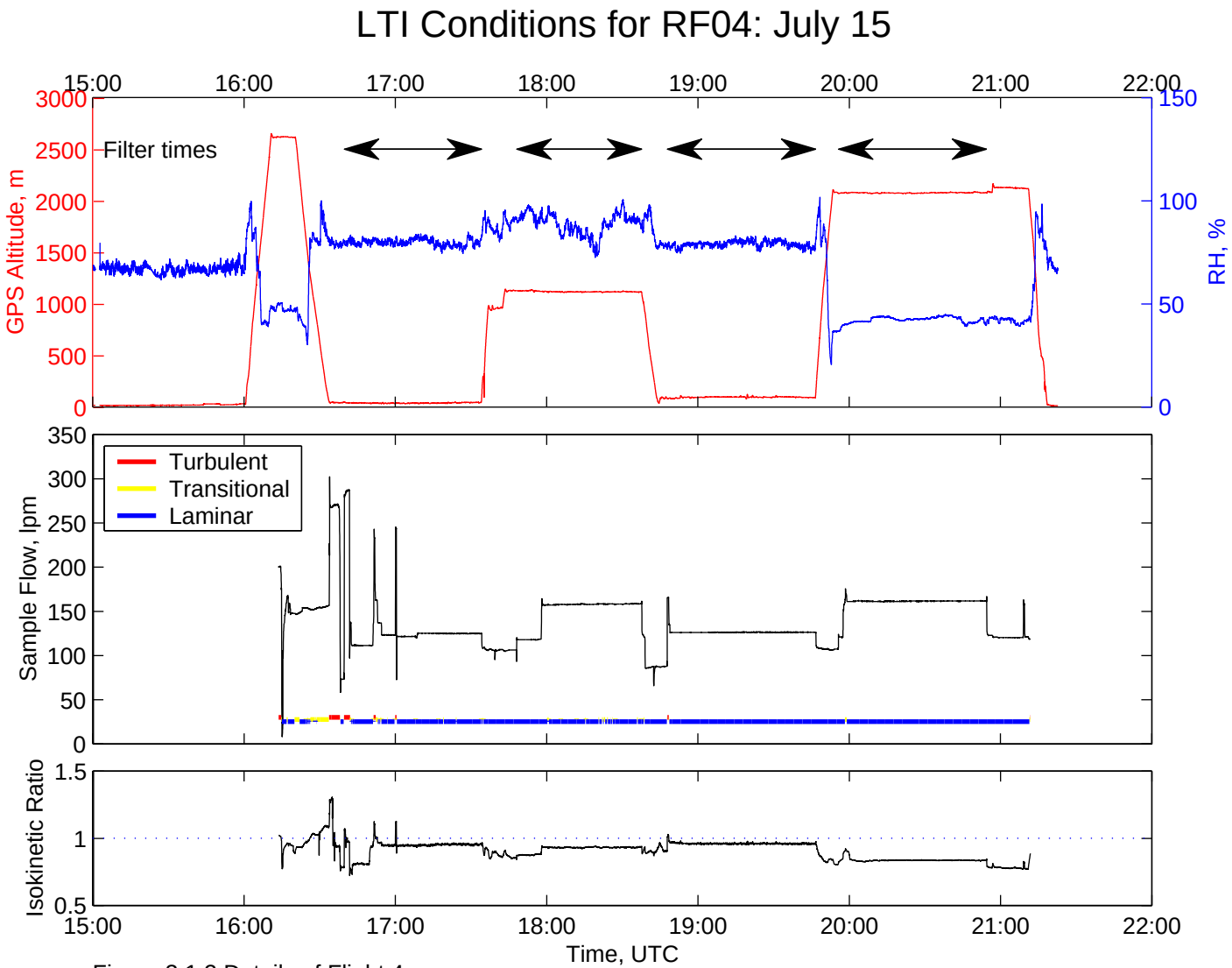

Figure 3.1.2 Details of Flight 4

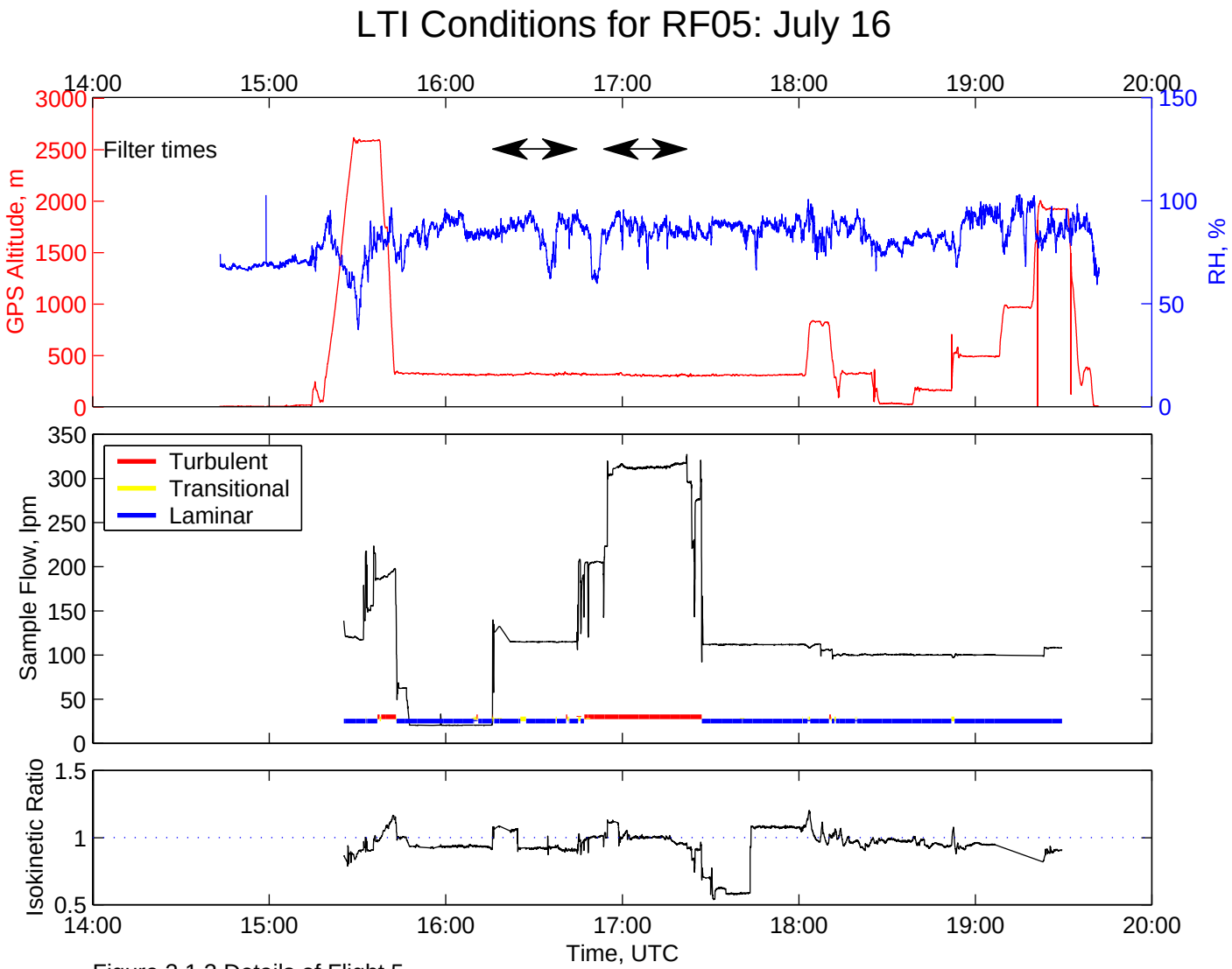

Figure 3.1.3 Details of Flight 5

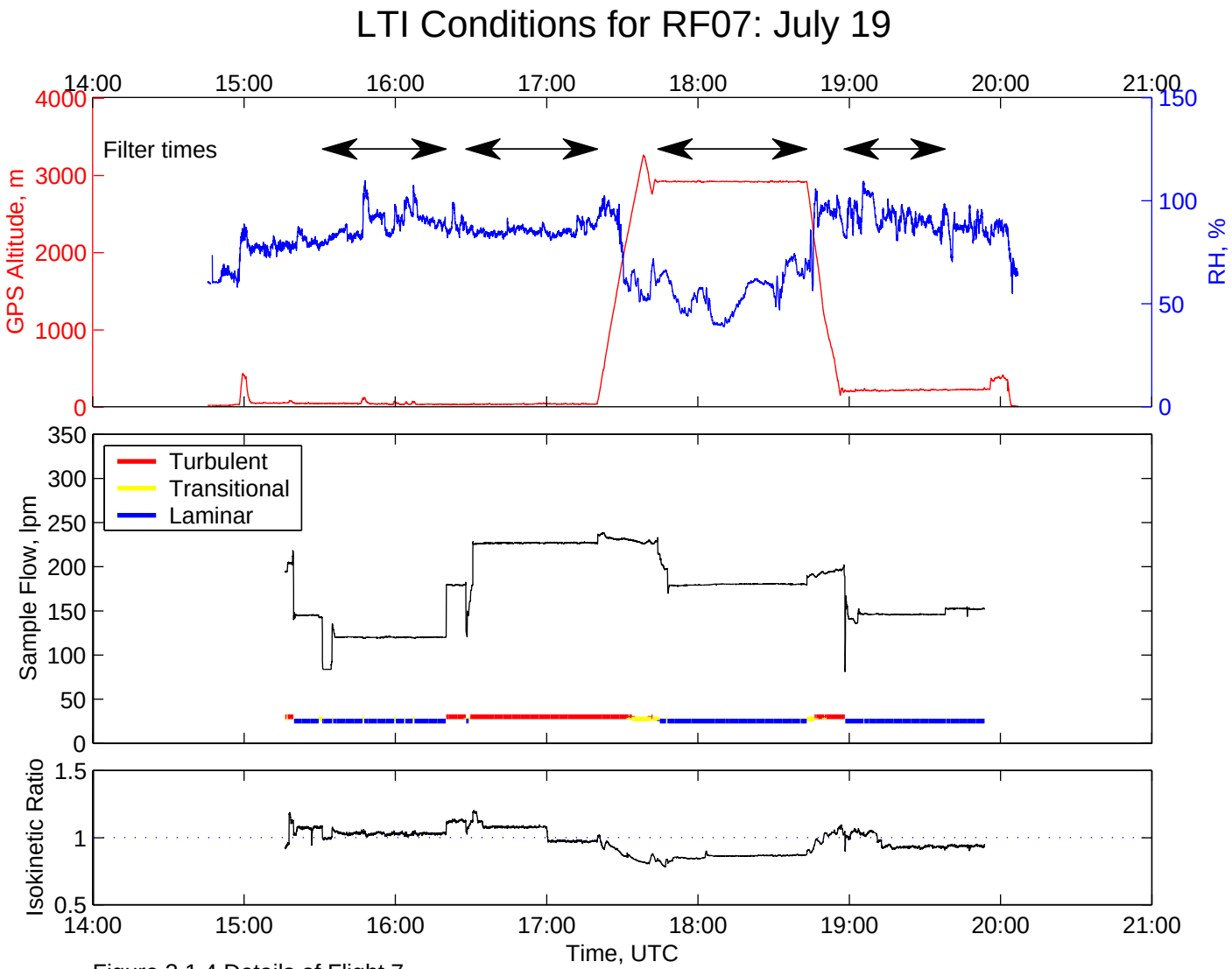

Figure 3.1.4 Details of Flight 7

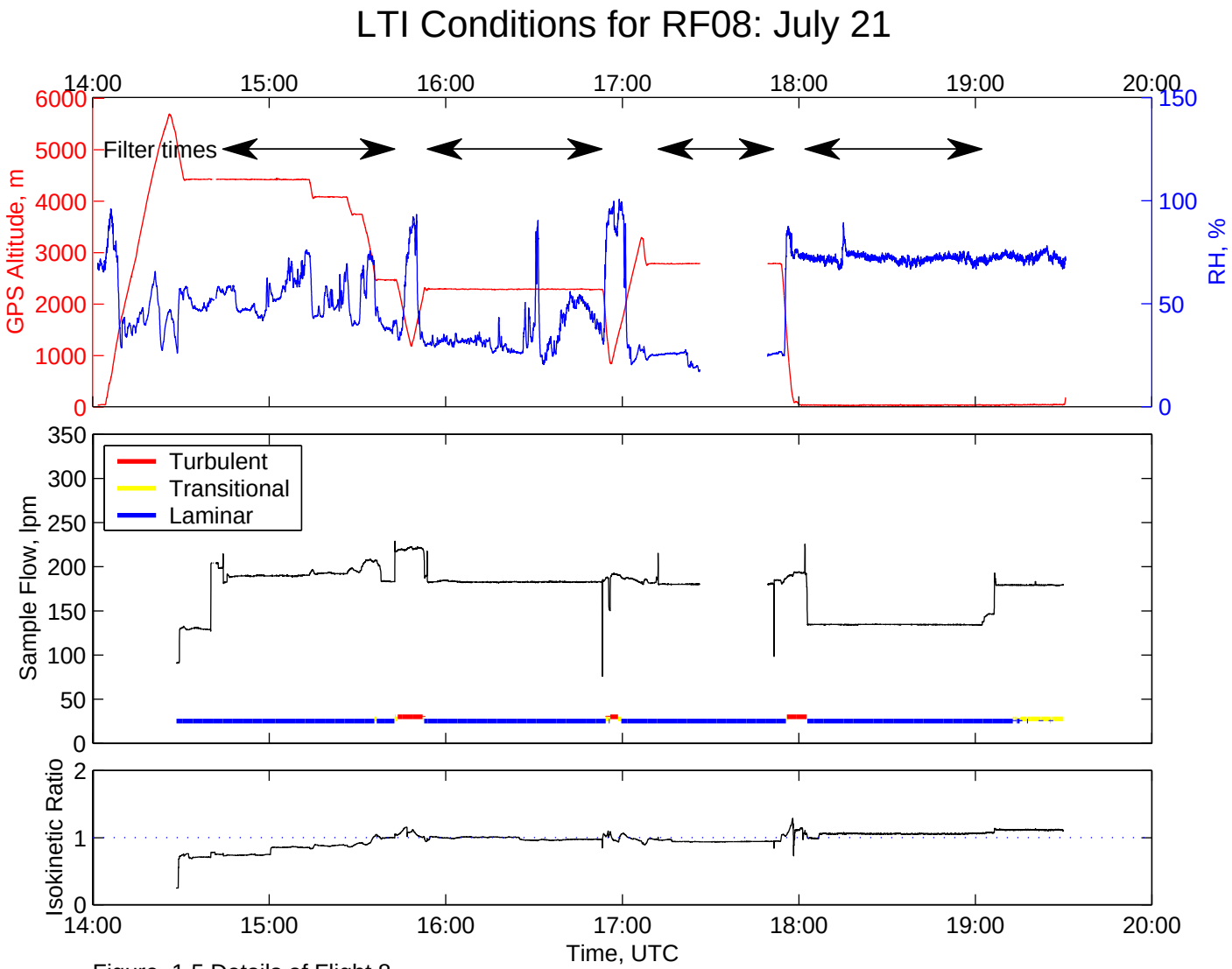

Figure .1.5 Details of Flight 8

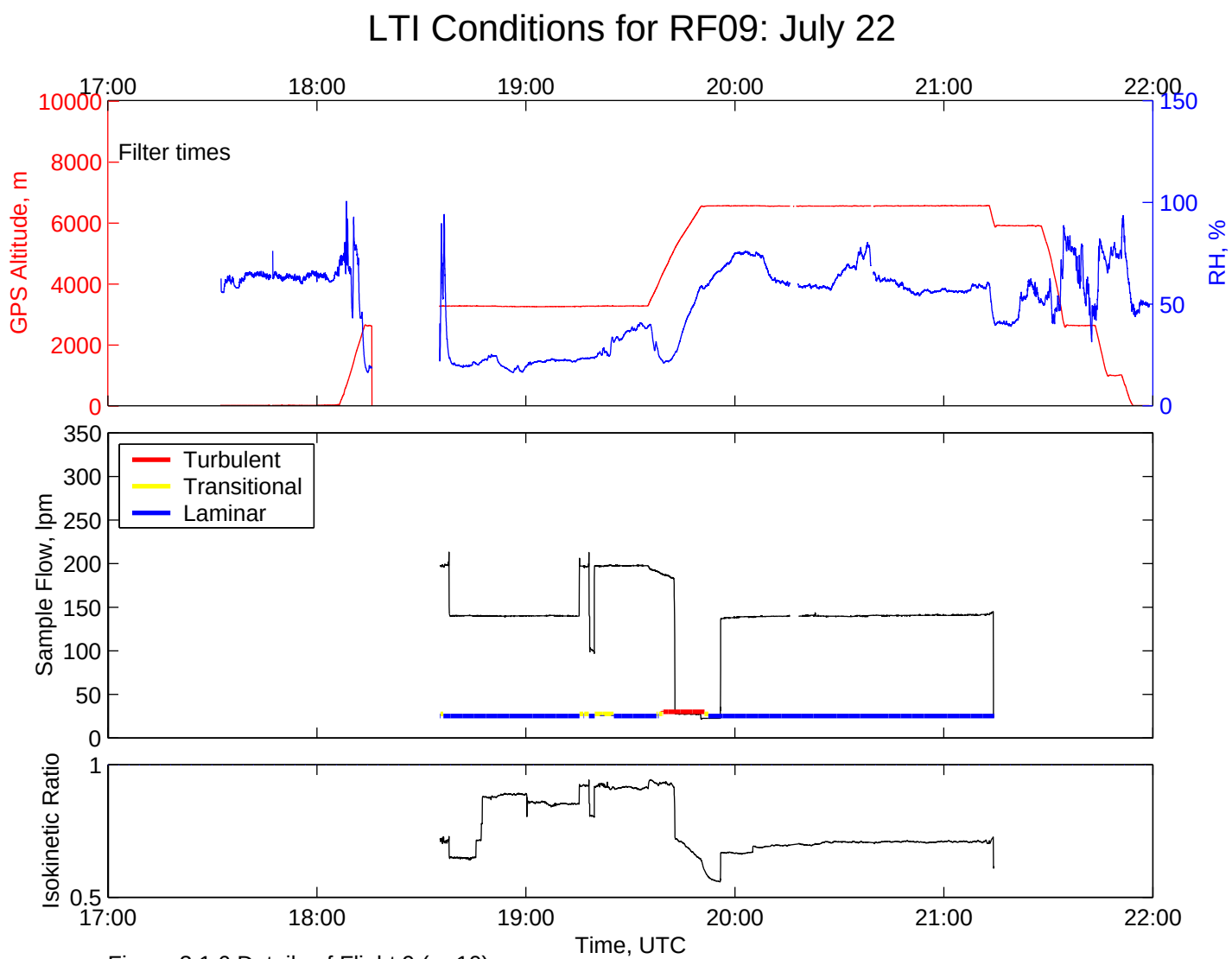

Figure 3.1.6 Details of Flight 9 (or 10)

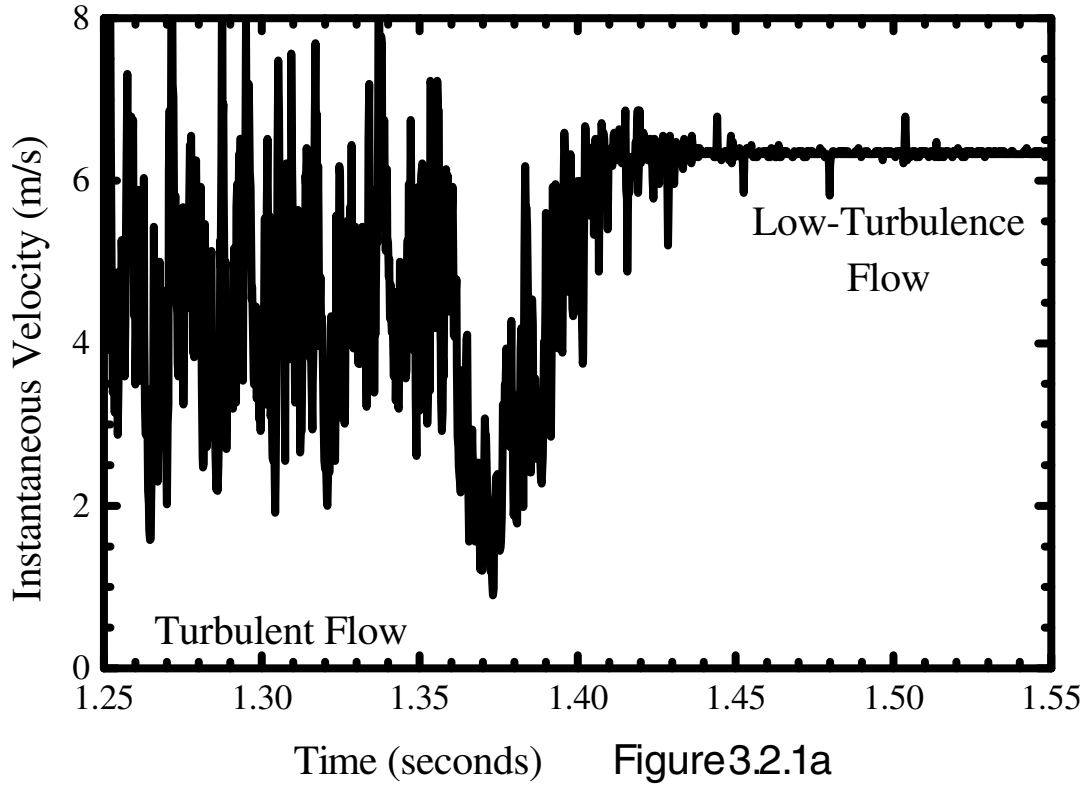

Figure3.2.1a

Hot film anemometer velocity vs time in a laboratory test of a porous diffuser. The suction valve was opened at 1.36 seconds and the flow was laminar by 1.43 seconds.

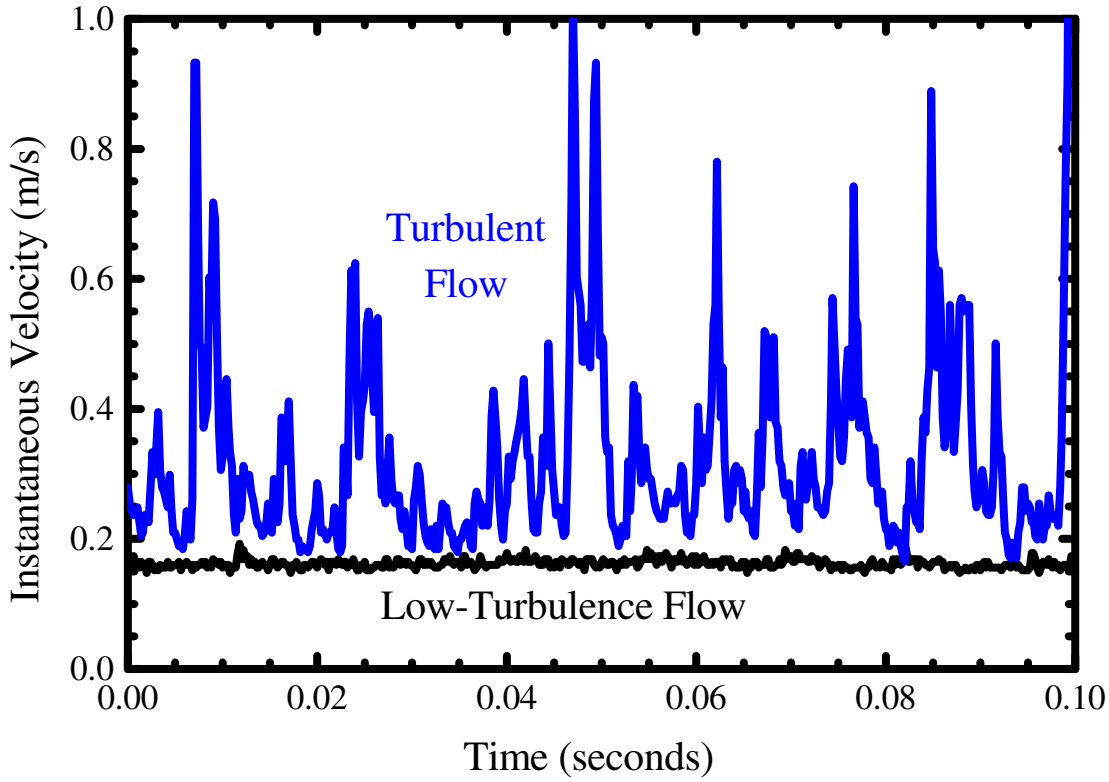

Figure 3.2.2 Hot film anemometer trace from the aircraft during PELTI. This turbulence (induced by increasing the sample flow) is far less intense than that when no suction is applied or when the inlet was used with a sharp leading edge.

Figure 3.3.1 PELTI Chloride

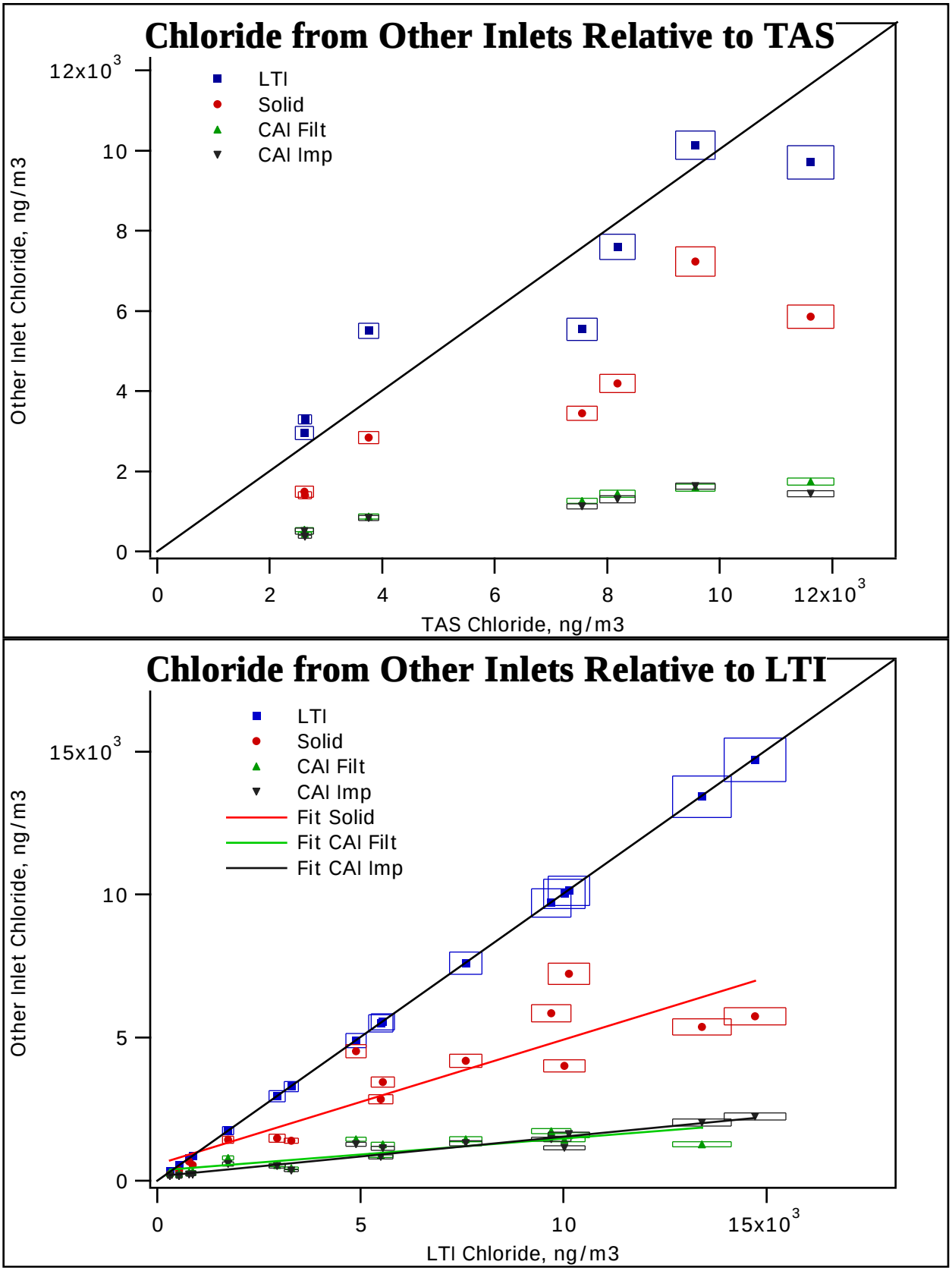

Figure 3.3.2 PELTI Sulfate

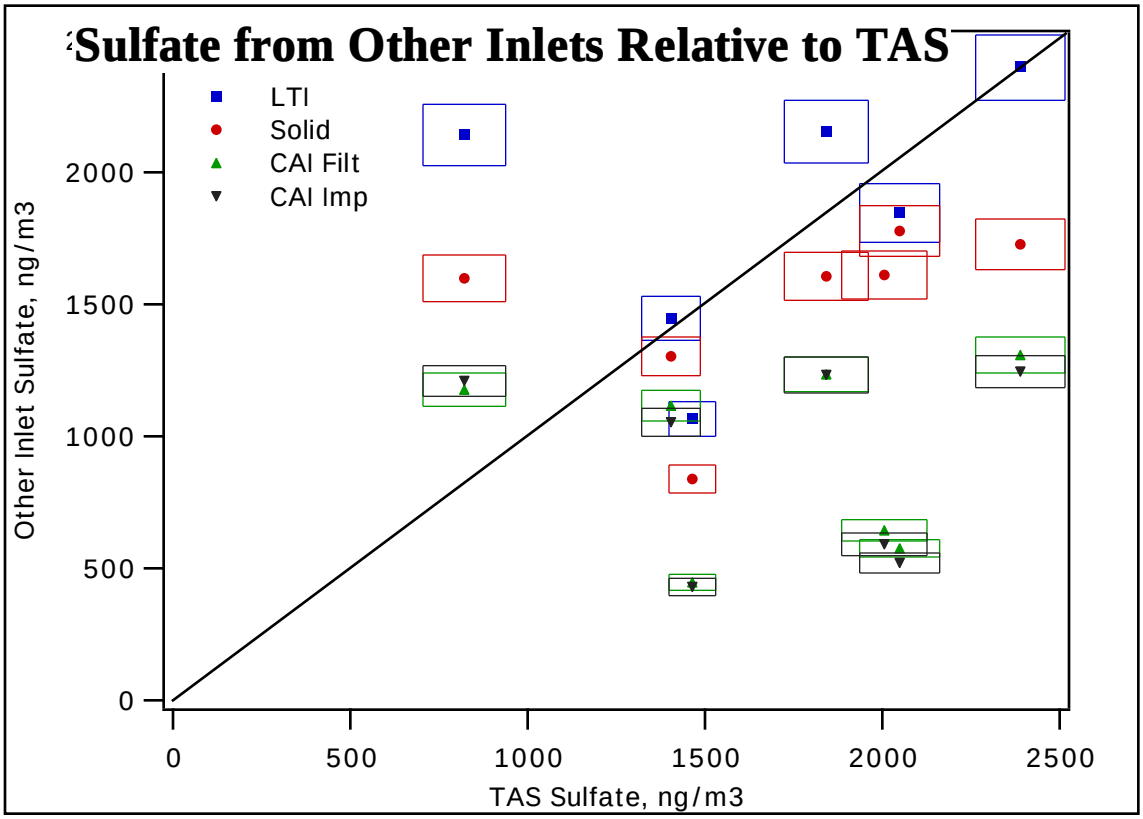

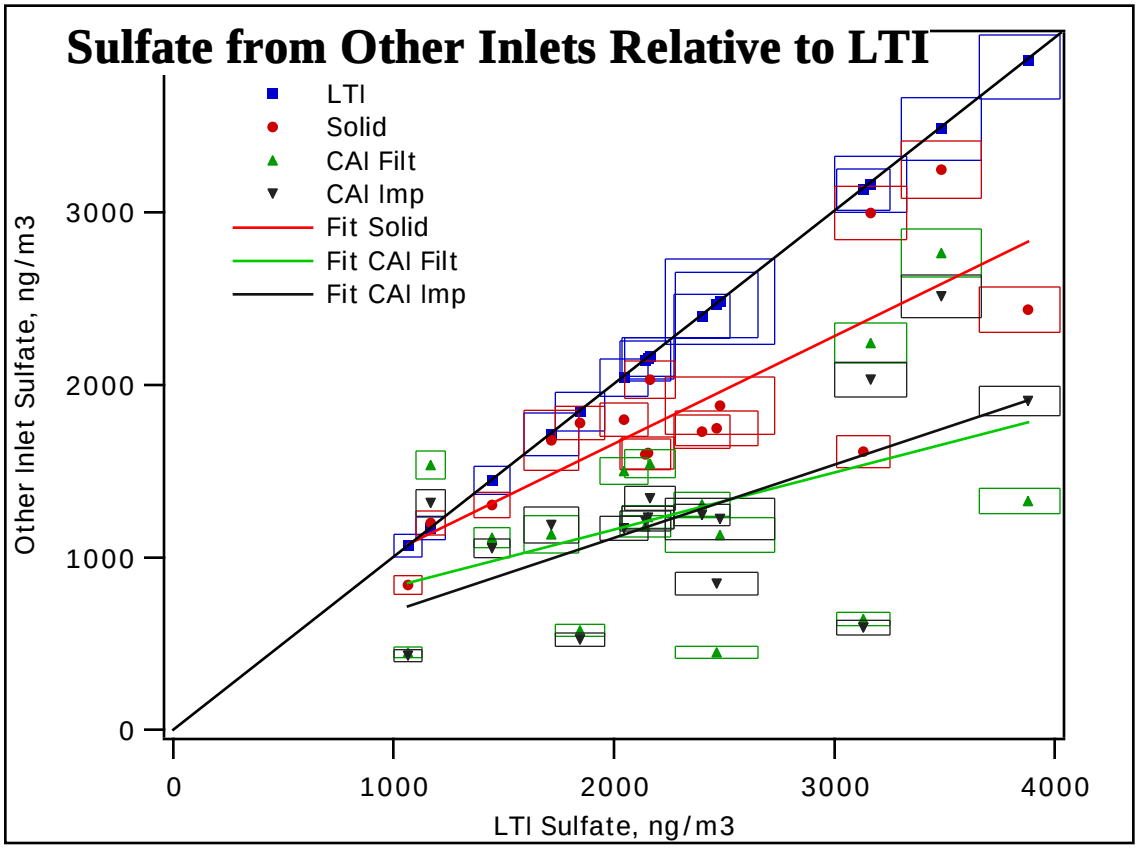

Figure 3.3.3 PELTI Sodium

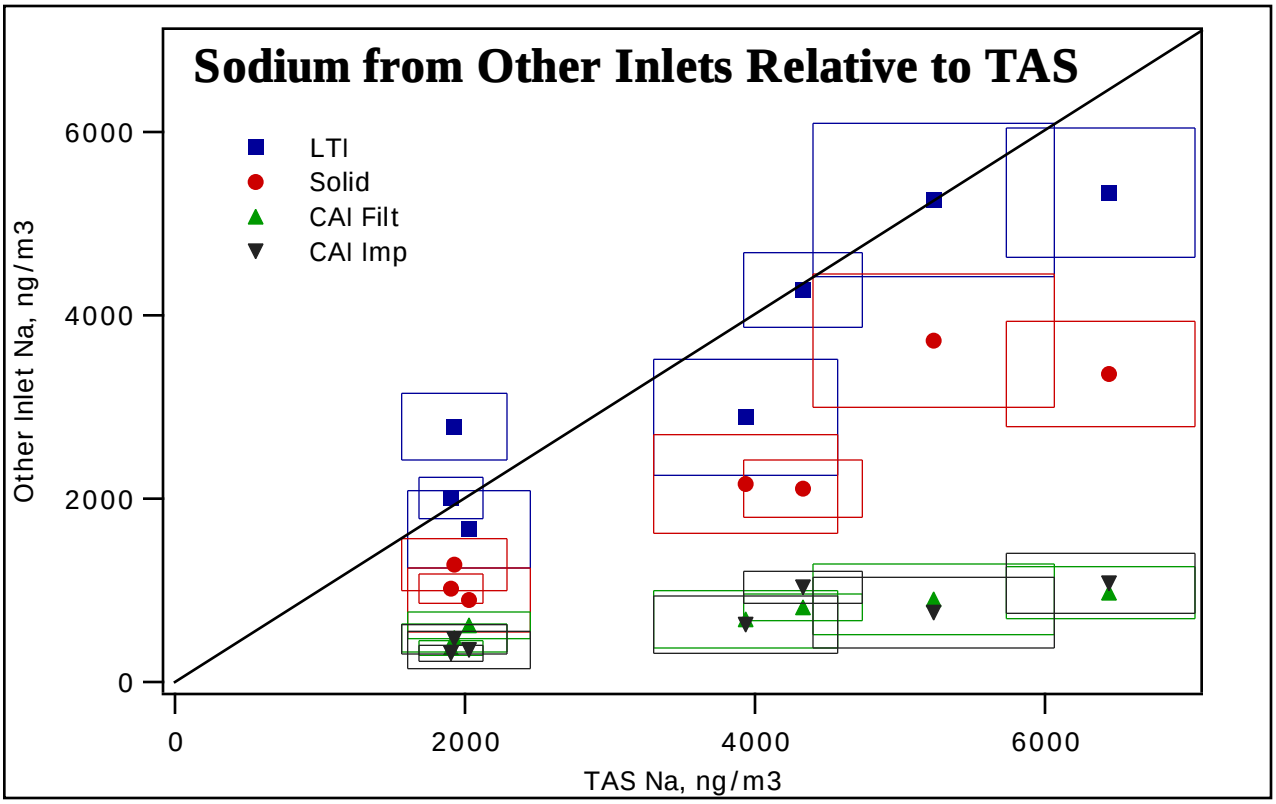

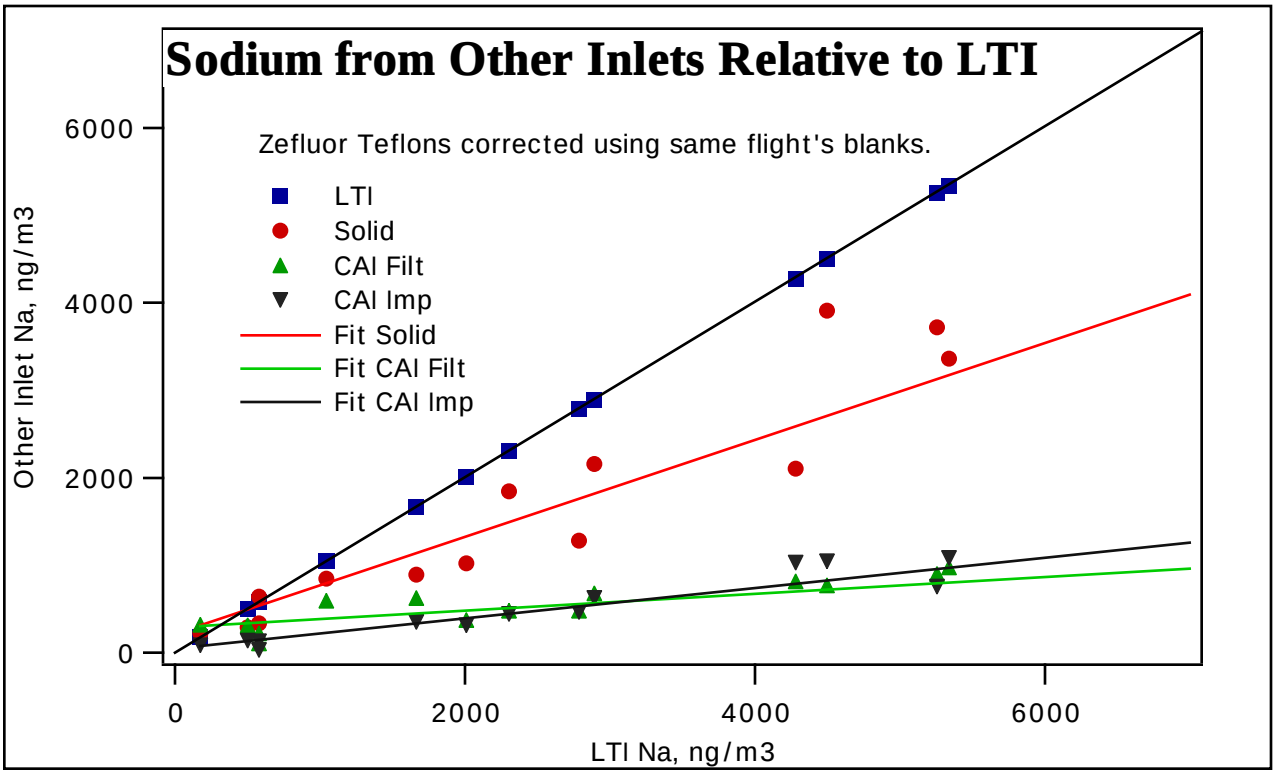

Note: We found highly variable Na contamination in this batch of Zefluor 90 mm filters, from as little as 0.2 ug Na to as high as 10 ug Na. The very high values were in <20% of the filters, so we did not identify and resolve this problem prior to the PELTI deployment. The result is a very large uncertainty on our Na data, 10-20% of which is affected by the contamination.

Figure 3.3.4 PELTI Magnesium

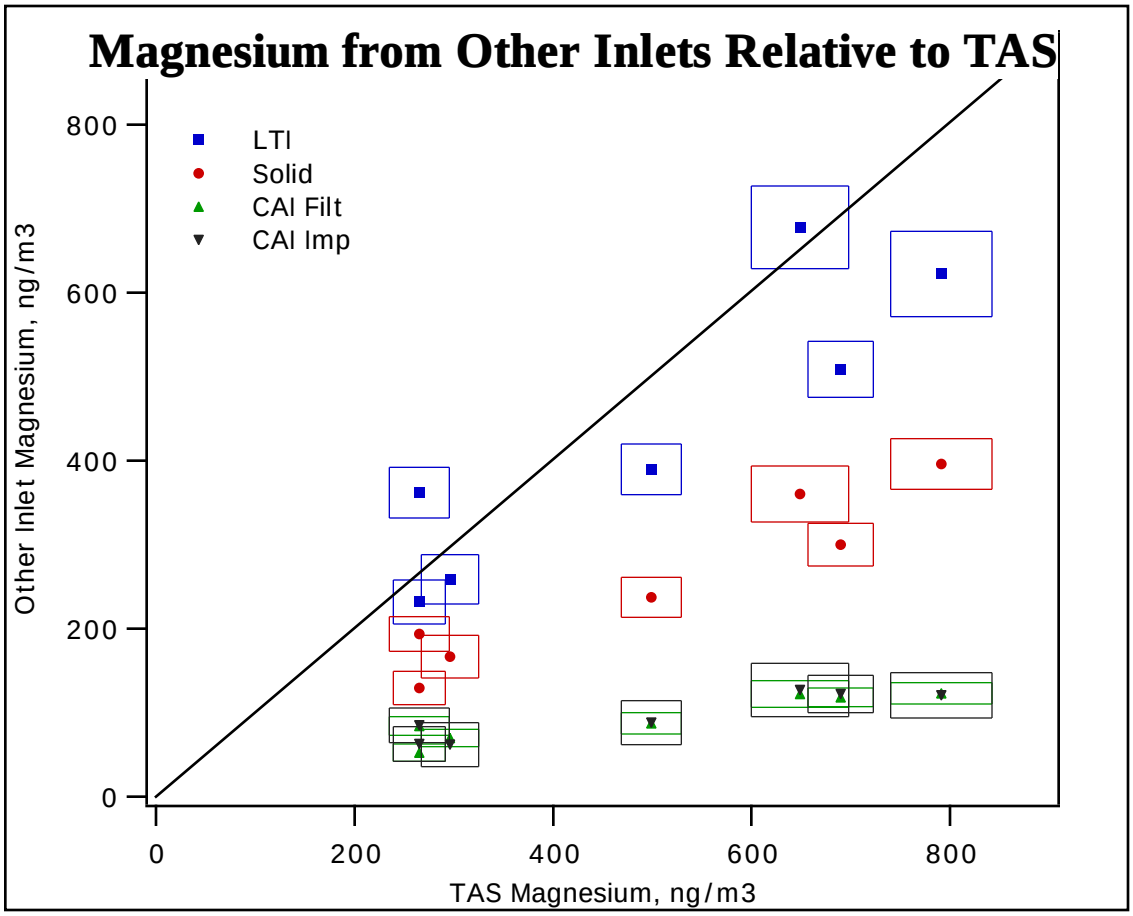

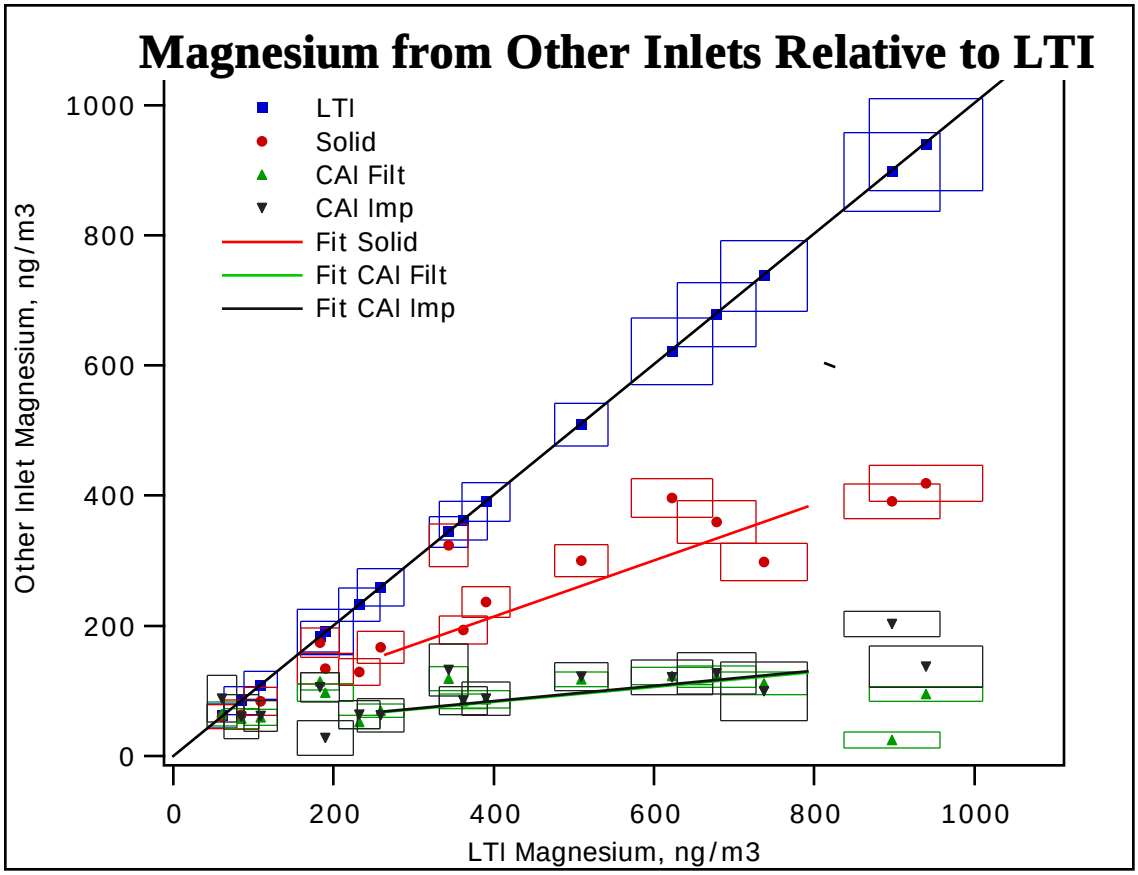

Figure 3.3.5 PELTI Calcium

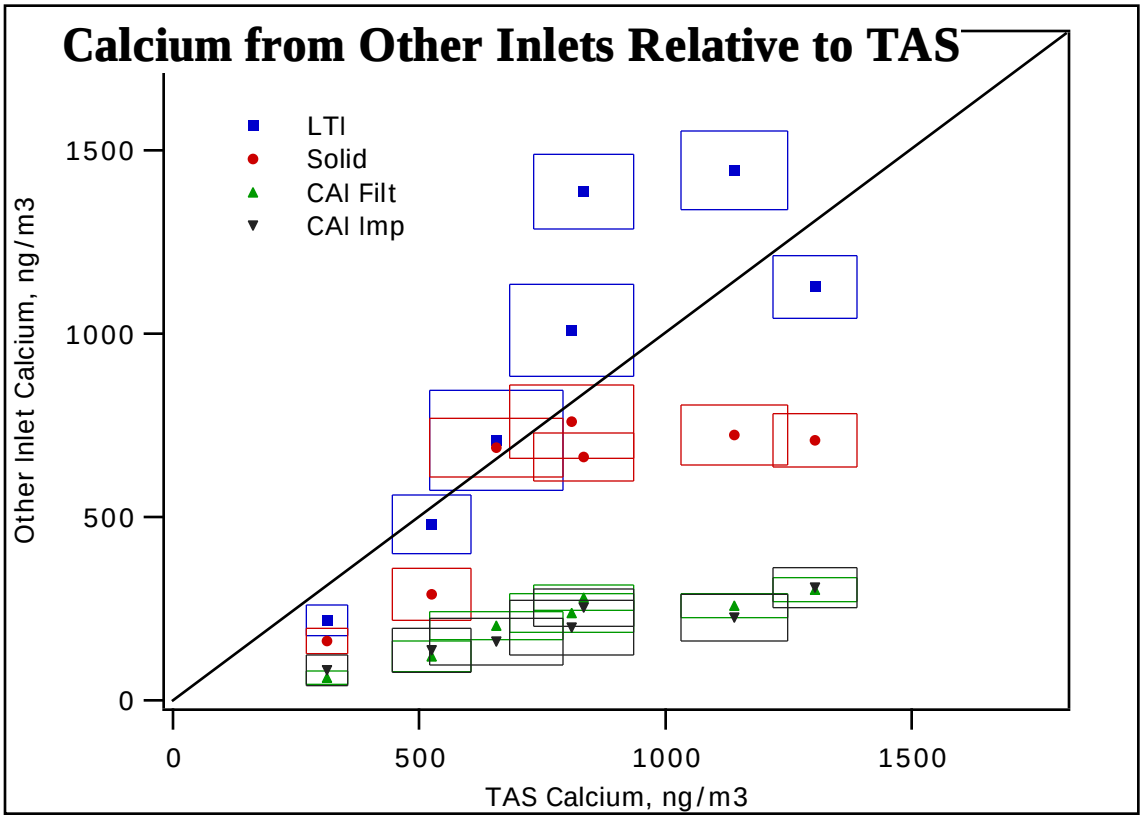

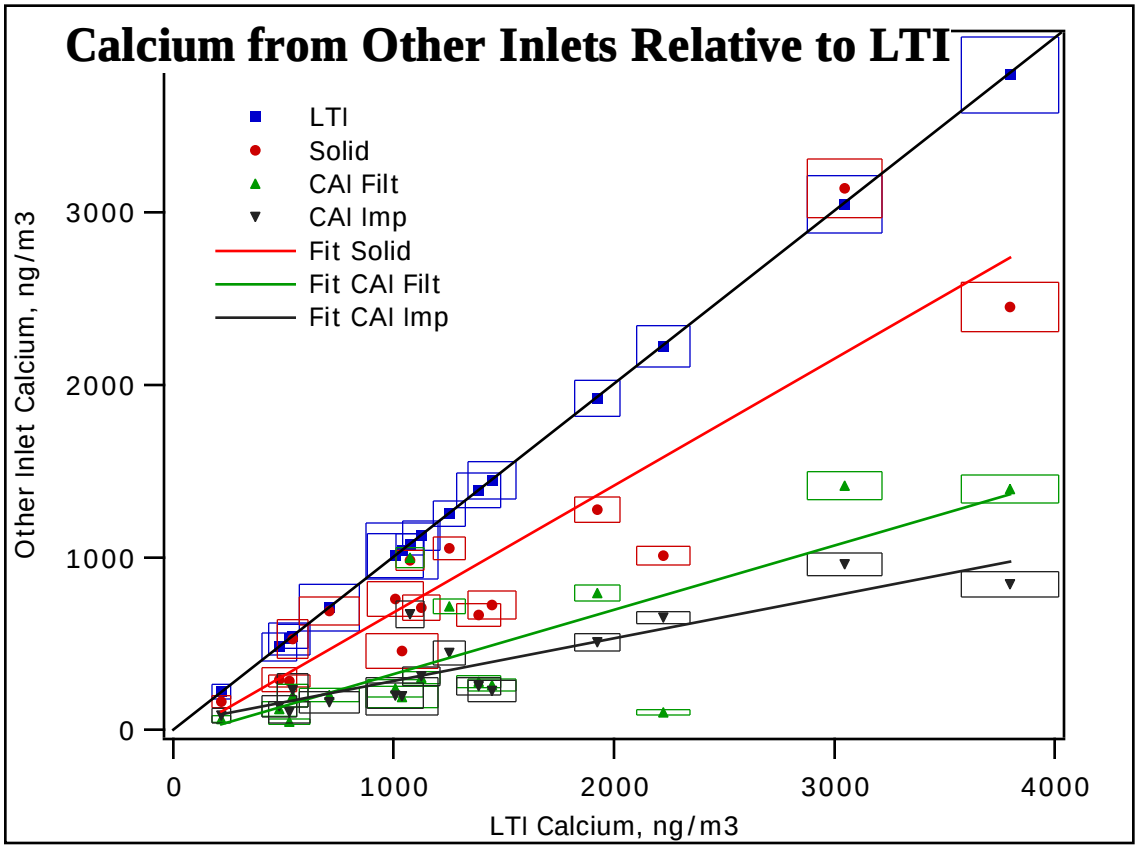

Figure 3.3.6 PELTI NSS[Mg]

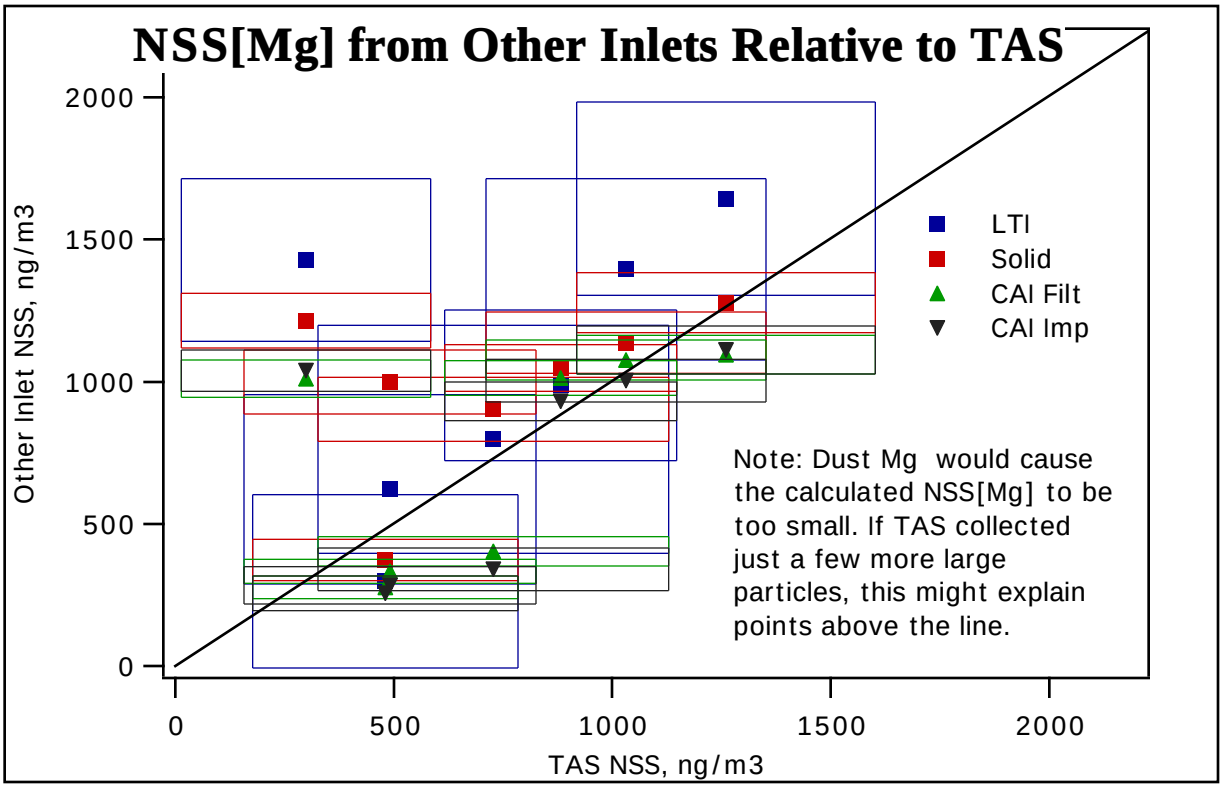

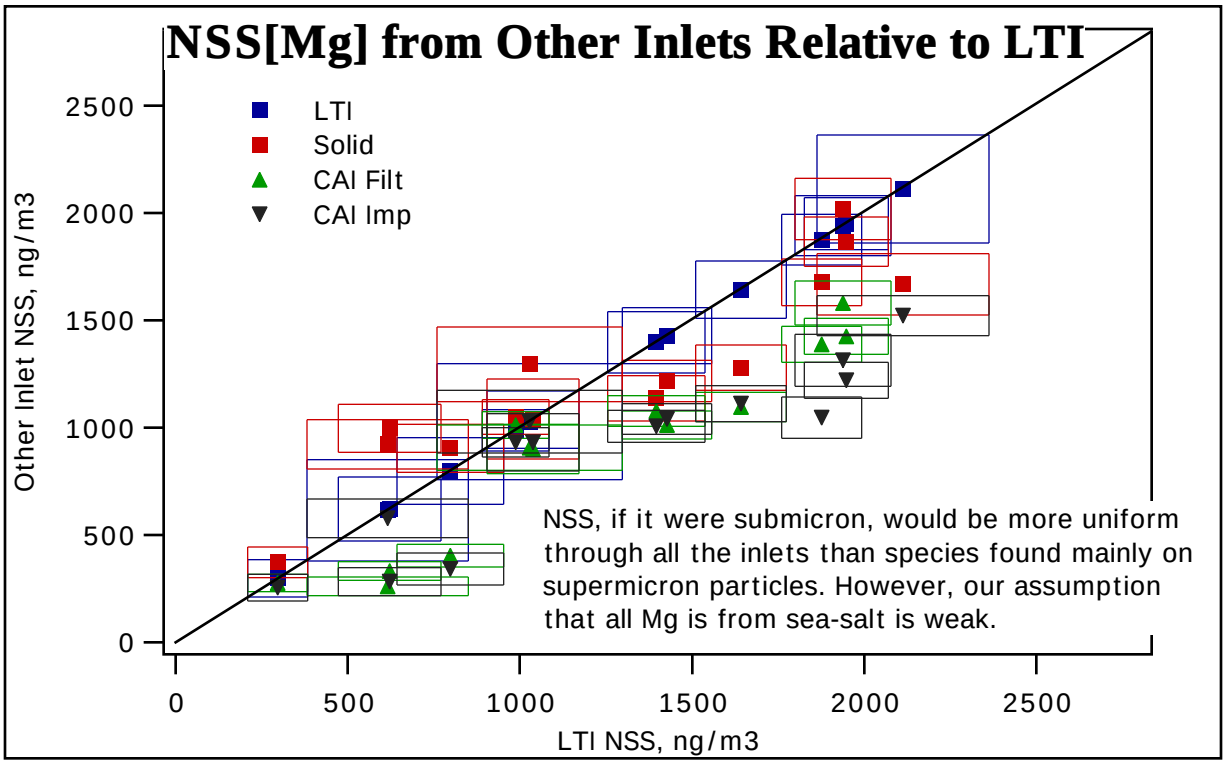

Figure 3.3.7 Impact of Turbulence on LTI Efficiency

There is just one pair of turbulent and laminar legs that have TAS samples for reference: RF07

Relative to TAS, the LTI was more efficient when laminar than turbulent.

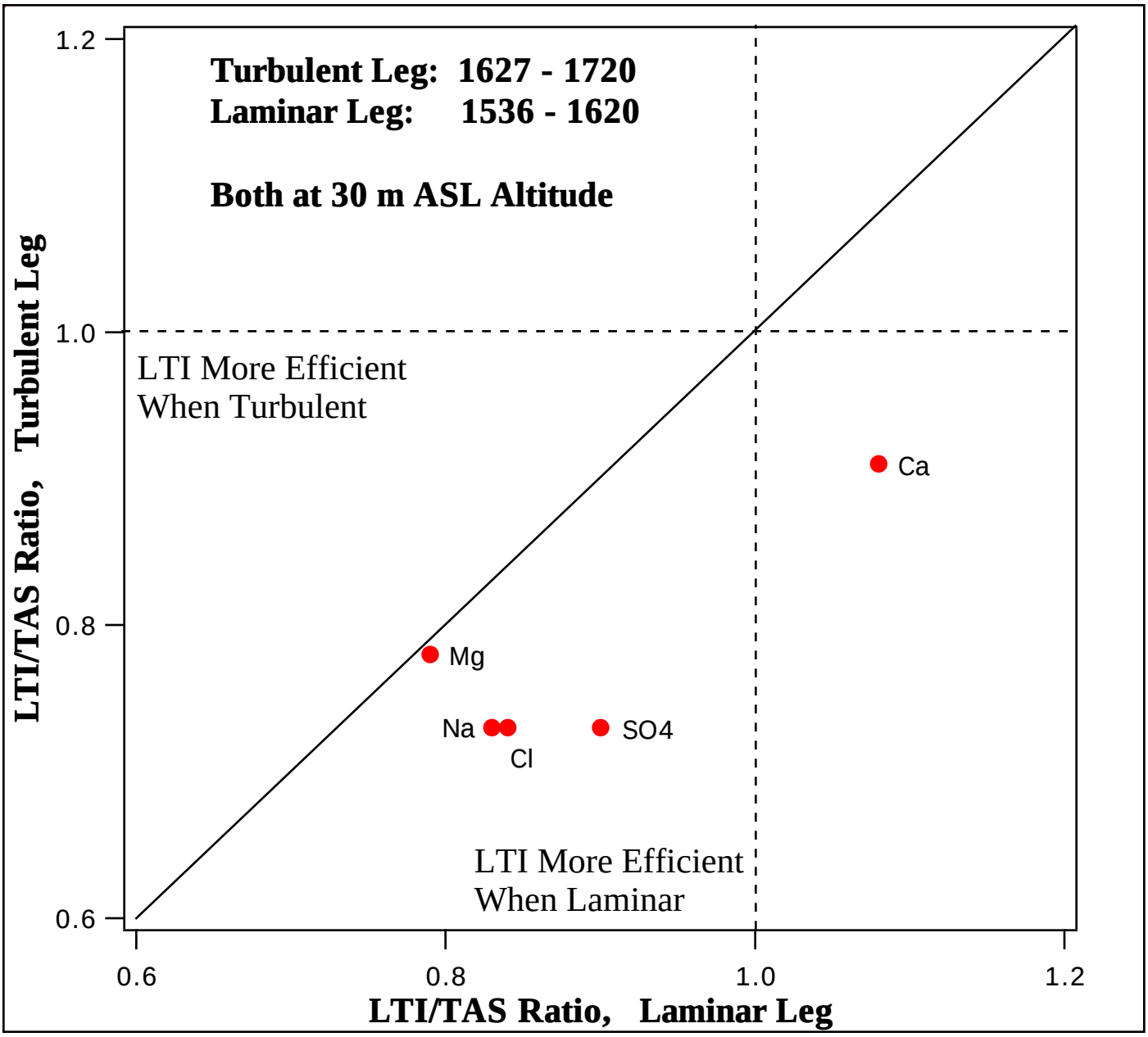

Figure 3.3.8 Impact of Turbulence on LTI Efficiency

We flew 8 laminar MBL legs and 3 turbulent MBL legs. Here the SD is used as a reference for comparison. When the LTI is turbulent, it exhibits less advantage over SD than when the LTI is laminar.

The high efficiency of the LTI is clearly due to the absence of turbulence.

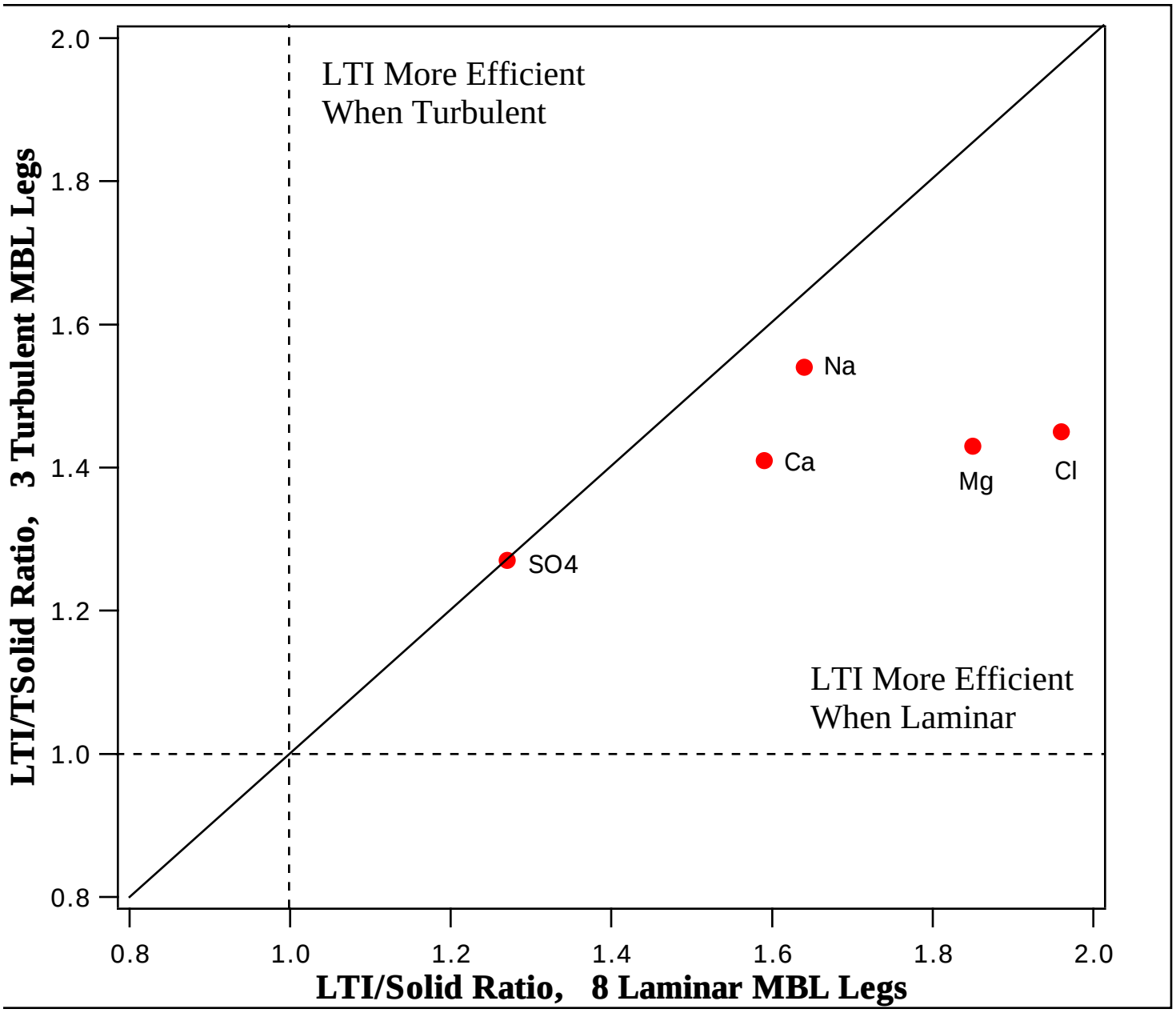

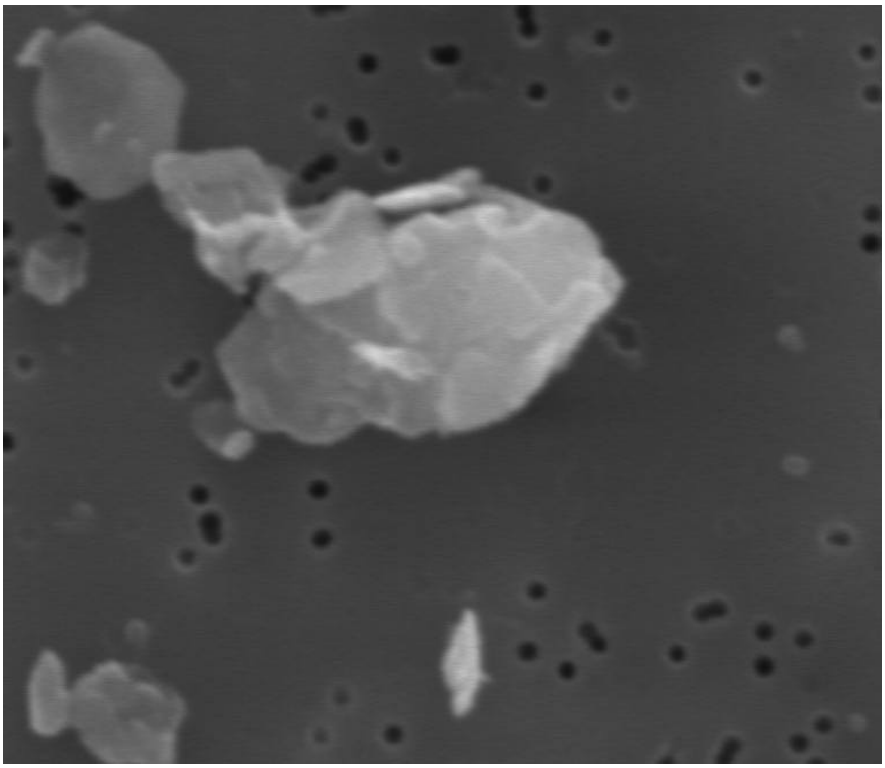

Figure 3.4.1 Secondary electron image of a clay aggregate on a TAS Nuclepore filter in RF08T1444.Field of view is 12 microns wide and filter pores are about 0.4 microns in diameter. Composition of the clay suggests it is a smectite.

Figure 3.4.1 Clay Aggregate

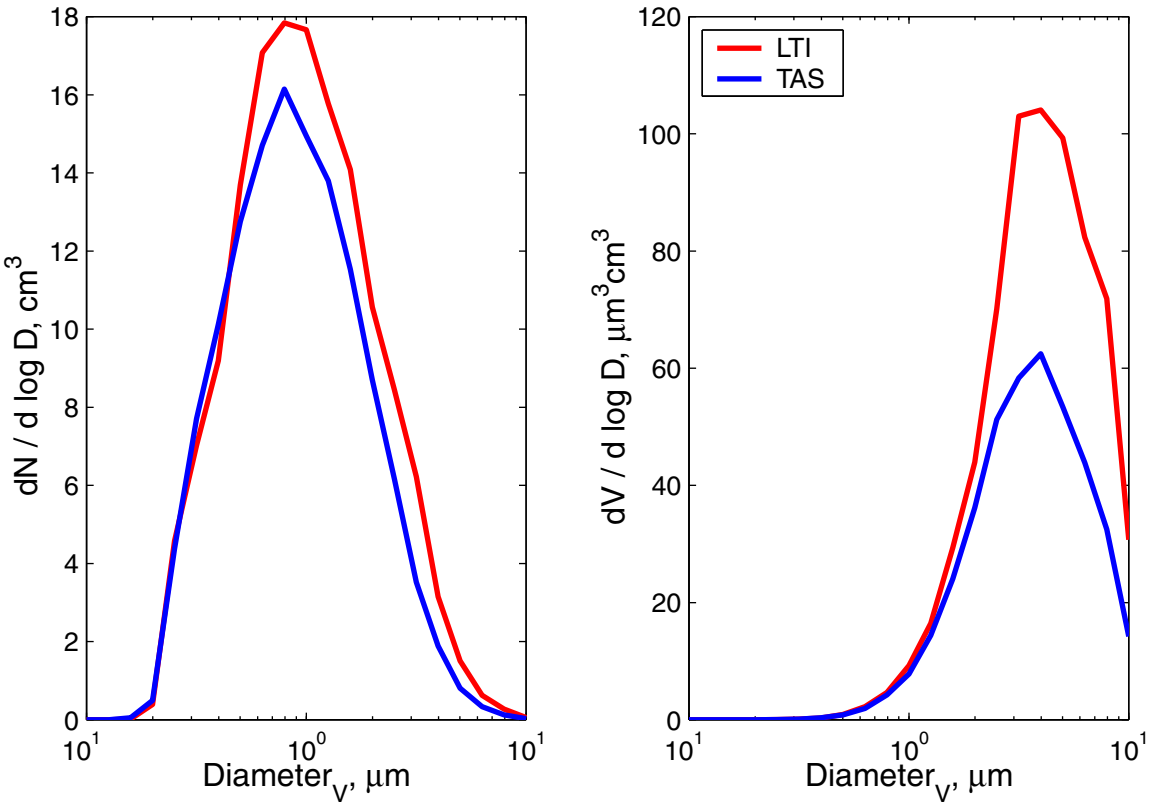

Figure 3.4.2 Size distributions via SEM for sample RF08-1553. The left panel is a number distribution, showing higher concentrations of supermicron particles behind the LTI than in TAS. The right panel demonstrates that the volume in the larger sizes is enhanced by as much as 75%. The (effective spherical) diameter is derived by multiplying the measured particle area by an assumed thickness equal to the minimum dimension to compute particle volume.

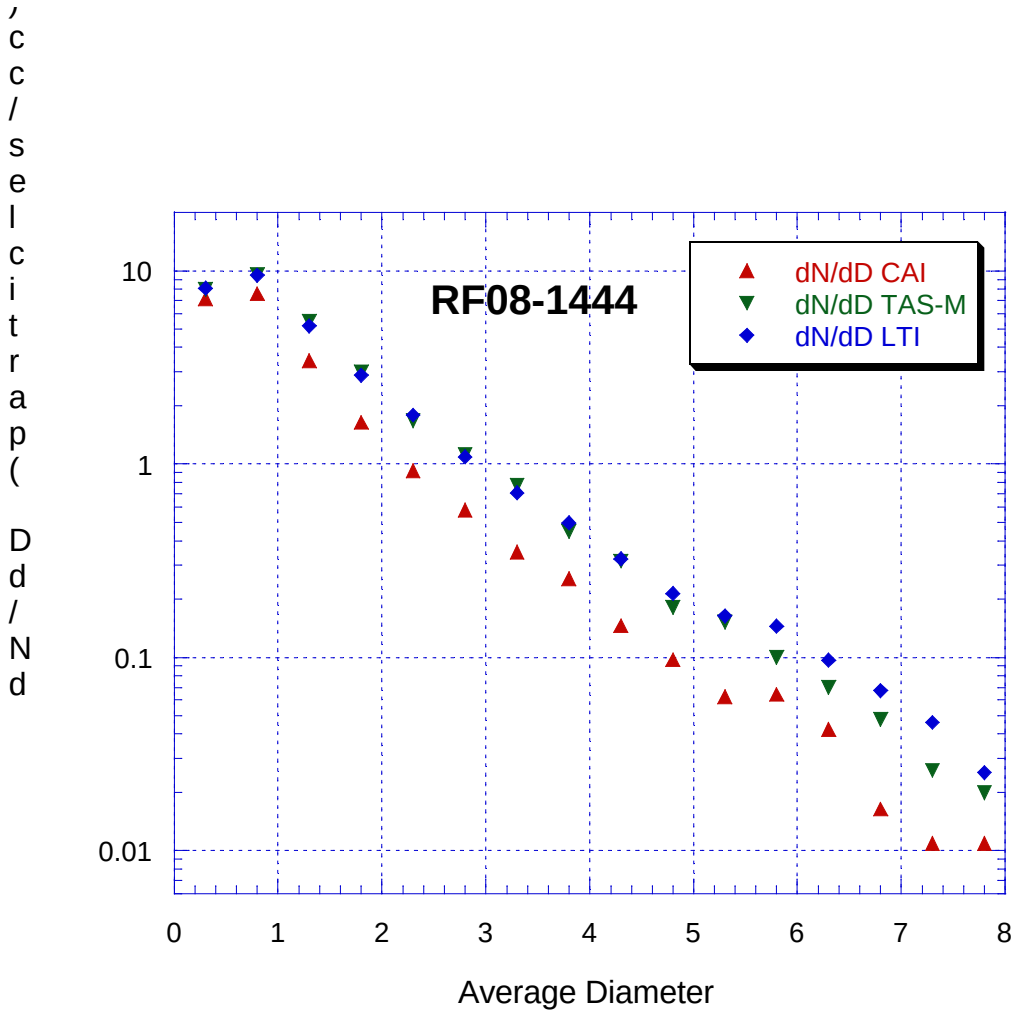

Figure 3.4.3 Size distributions for TAS middle, LTI, and CAI, sample RF08-1444. Bin width is 0.5 microns.

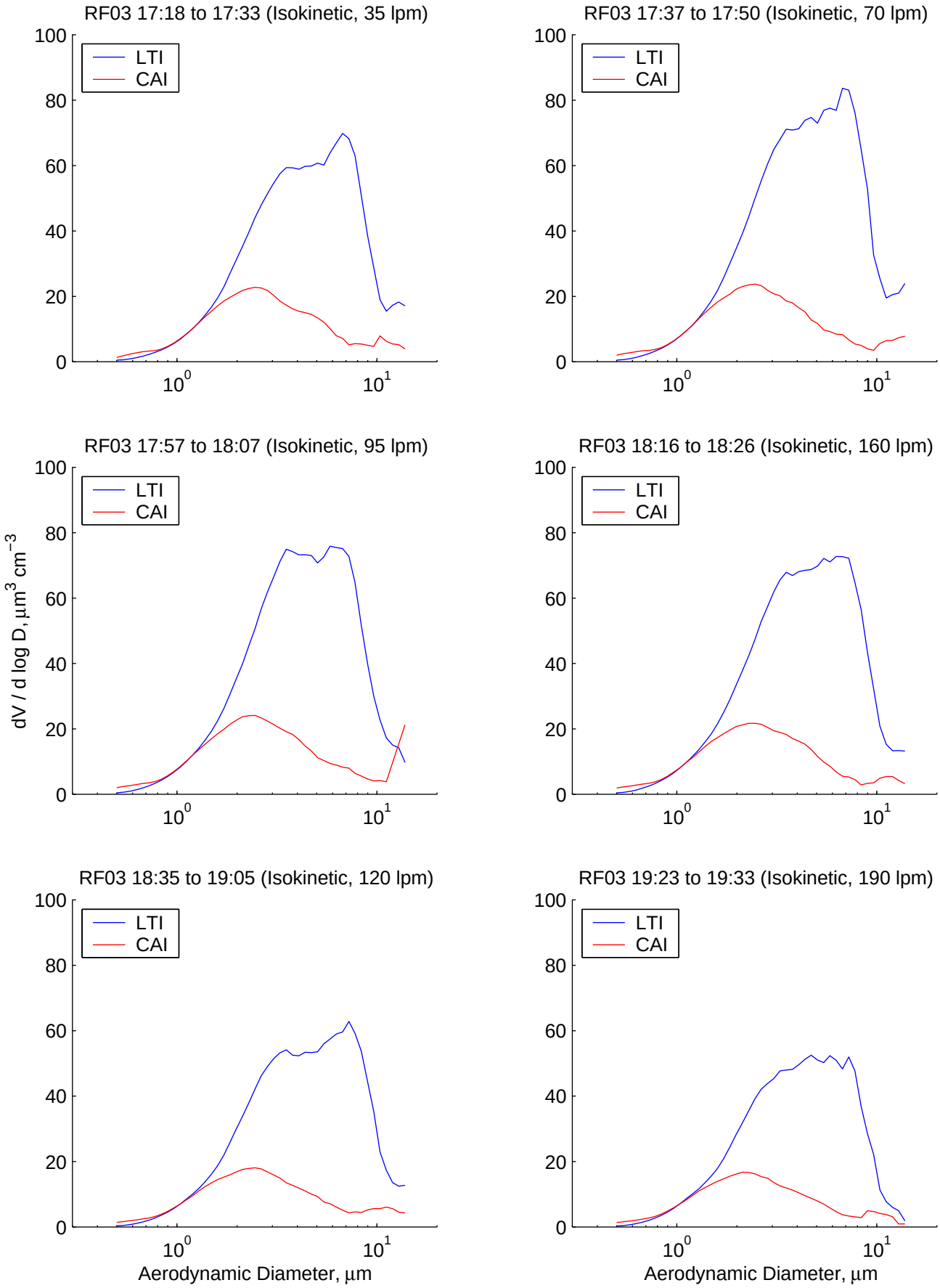
RF03 17:18 to 17:33 (Isokinetic, 35 lpm)
RF03 17:37 to 17:50 (Isokinetic, 70 lpm)
RF03 17:57 to 18:07 (Isokinetic, 95 lpm)
RF03 18:16 to 18:26 (Isokinetic, 160 lpm)
RF03 18:35 to 19:05 (Isokinetic, 120 lpm)
RF03 19:23 to 19:33 (Isokinetic, 190 lpm)
LTI
CAI
dV / d log D, µm3 cm−3
Aerodynamic Diameter, µm
0
20
40
60
80
100
10^0
10^1

Figure 3.5.1

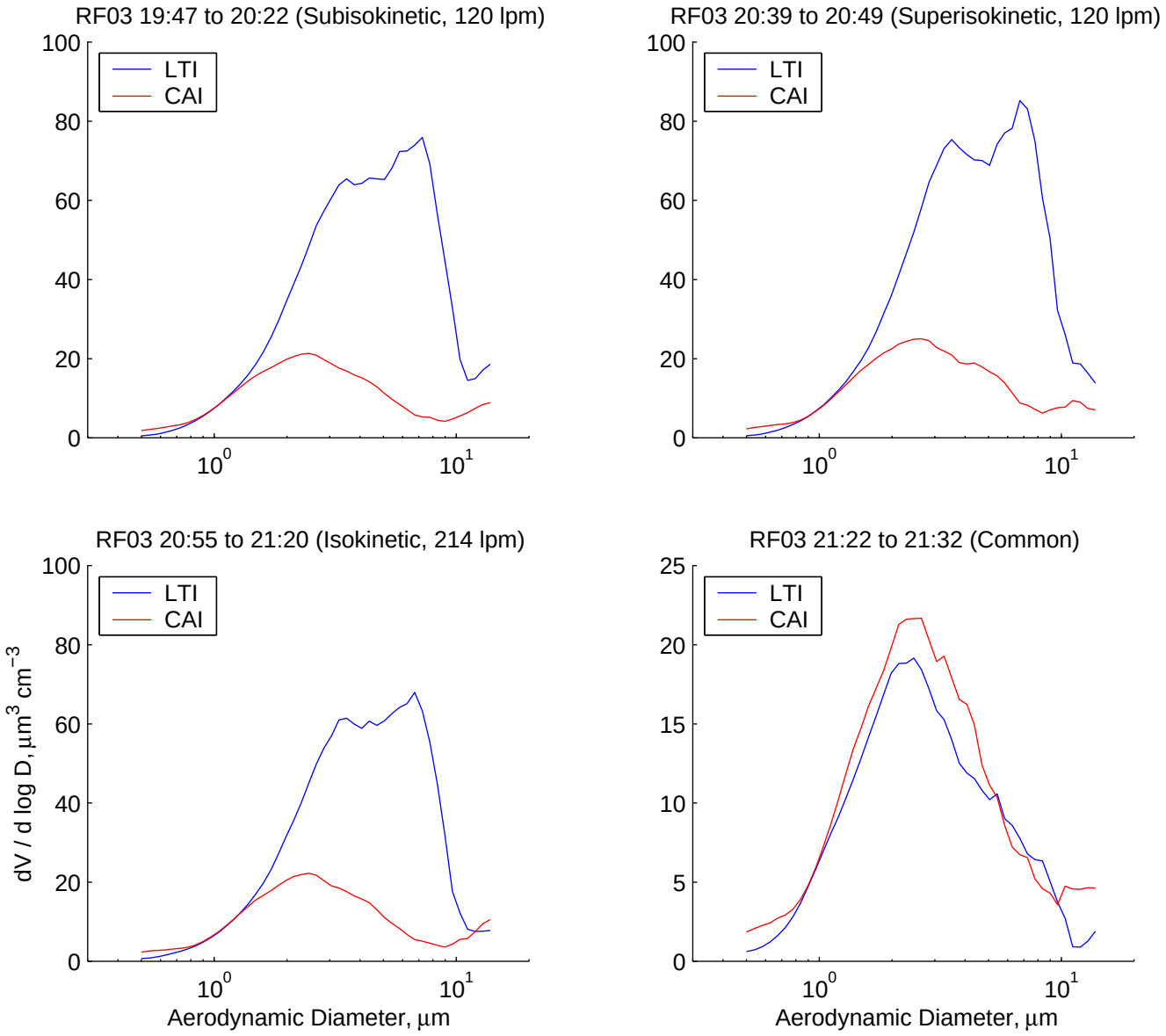

Figure 3.5.1, cont'd

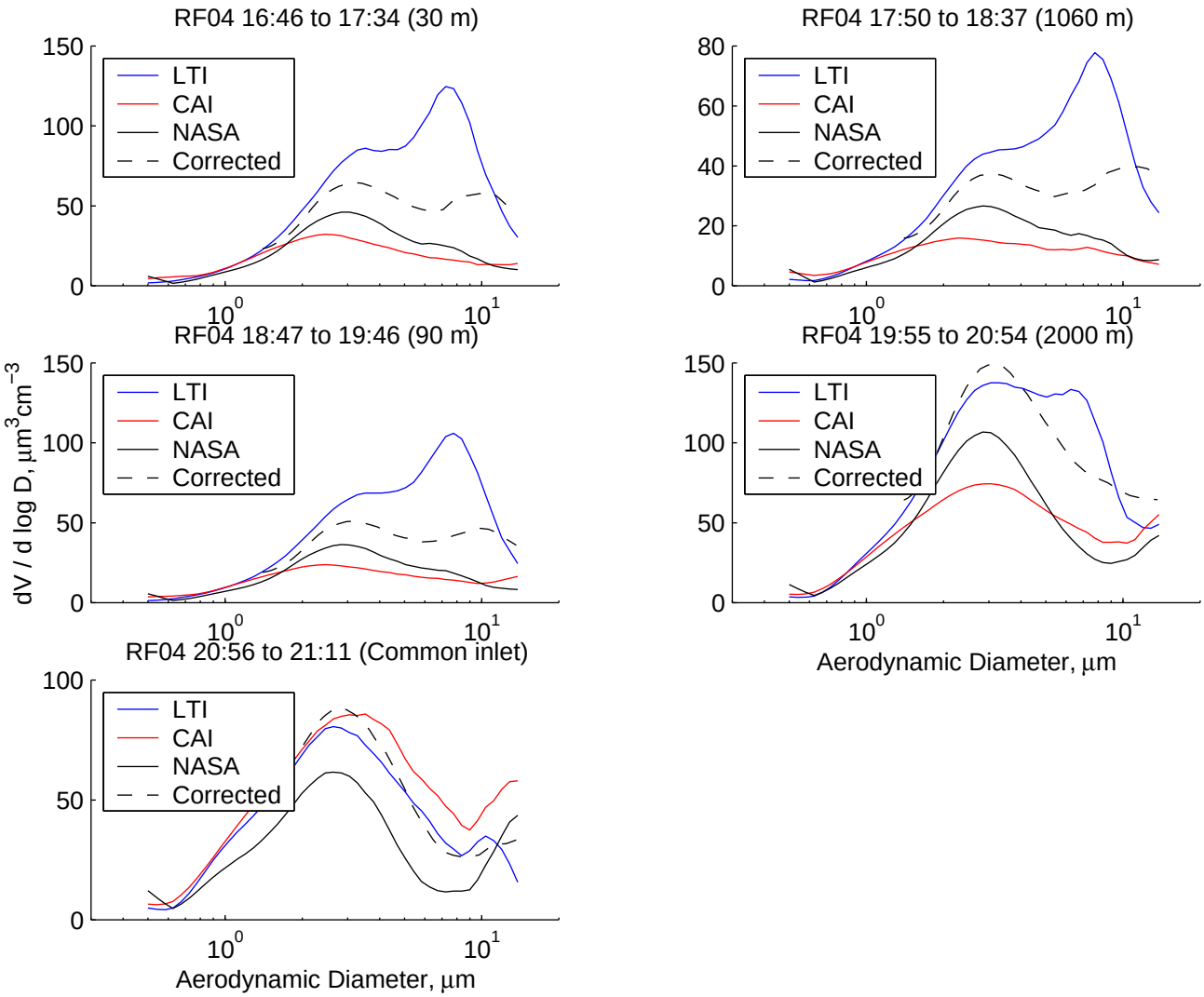
RF04 16:46 to 17:34 (30 m)
RF04 17:50 to 18:37 (1060 m)
RF04 18:47 to 19:46 (90 m)
RF04 19:55 to 20:54 (2000 m)
RF04 20:56 to 21:11 (Common inlet)
LTI
CAI
NASA
Corrected
dV / d log D, µm3cm−3
Aerodynamic Diameter, µm

Figure 3.5.2

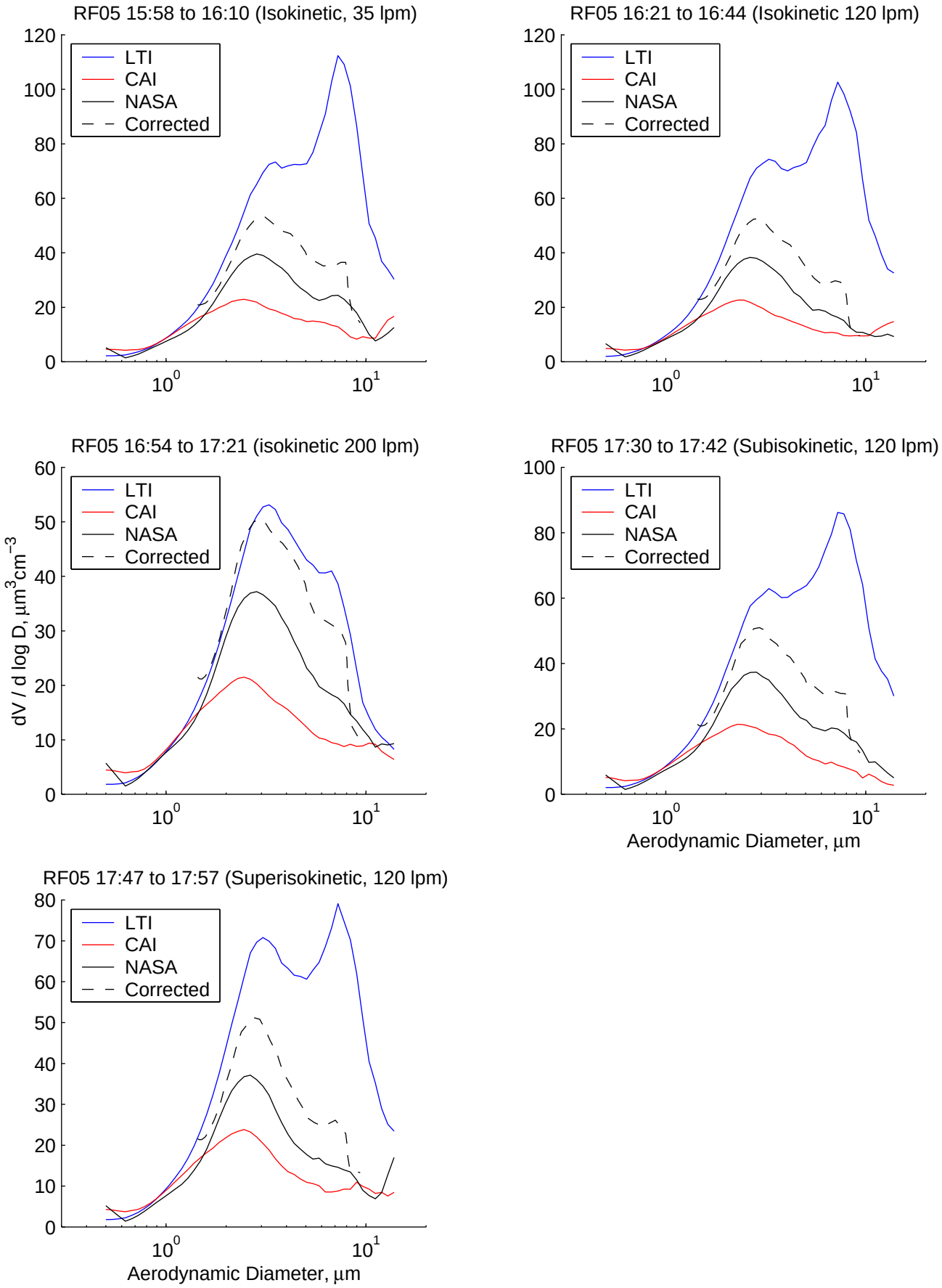
RF05 15:58 to 16:10 (Isokinetic, 35 lpm)
RF05 16:21 to 16:44 (Isokinetic 120 lpm)
RF05 16:54 to 17:21 (isokinetic 200 lpm)
RF05 17:30 to 17:42 (Subisokinetic, 120 lpm)
RF05 17:47 to 17:57 (Superisokinetic, 120 lpm)
LTI
CAI
NASA
Corrected
dV / d log D, µm3cm−3
Aerodynamic Diameter, µm

Figure 3.5.3

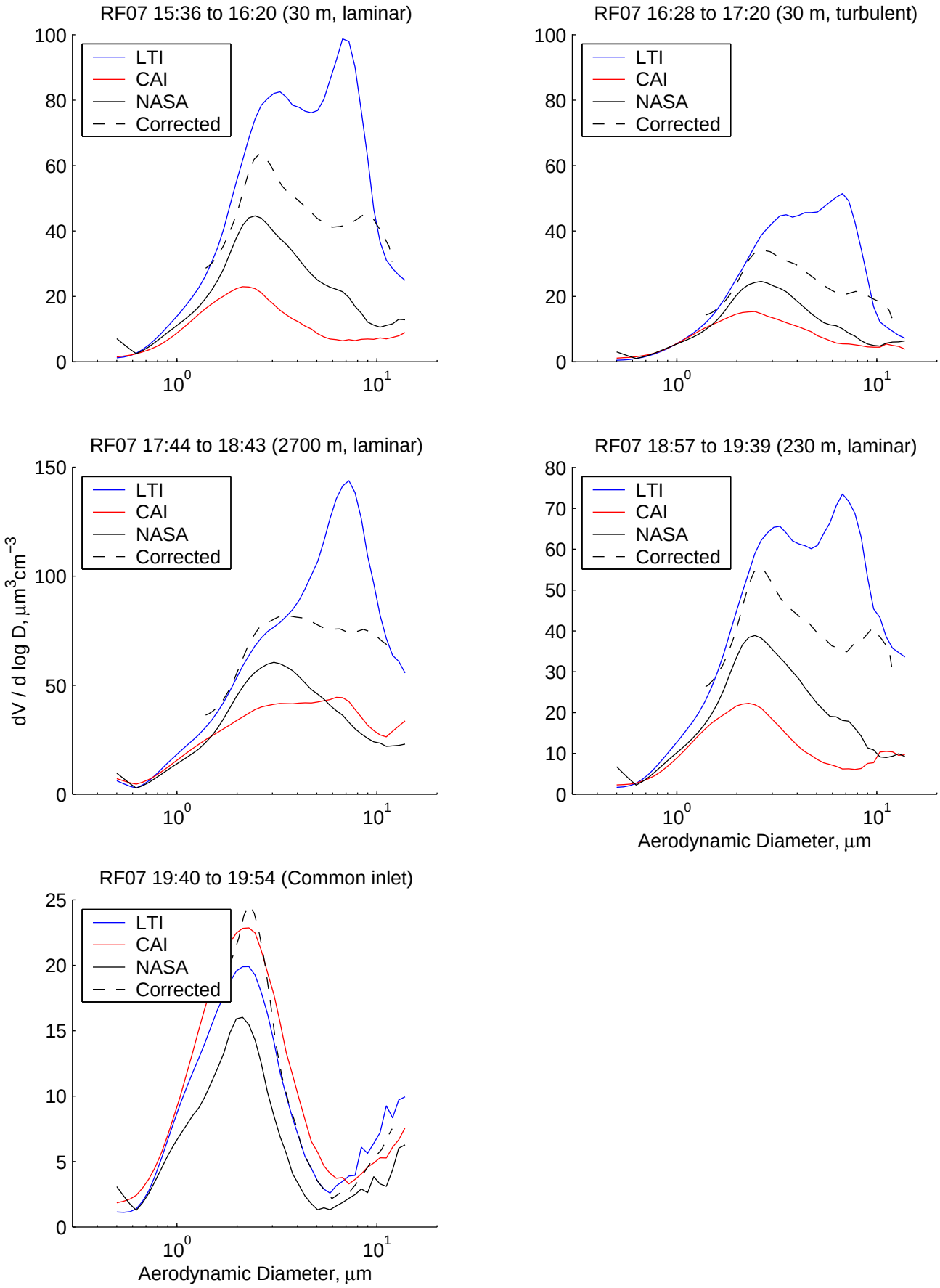
RF07 15:36 to 16:20 (30 m, laminar)
RF07 16:28 to 17:20 (30 m, turbulent)
RF07 17:44 to 18:43 (2700 m, laminar)
RF07 18:57 to 19:39 (230 m, laminar)
RF07 19:40 to 19:54 (Common inlet)
LTI
CAI
NASA
Corrected
dV / d log D, µm3cm−3
Aerodynamic Diameter, µm

Figure 3.5.4

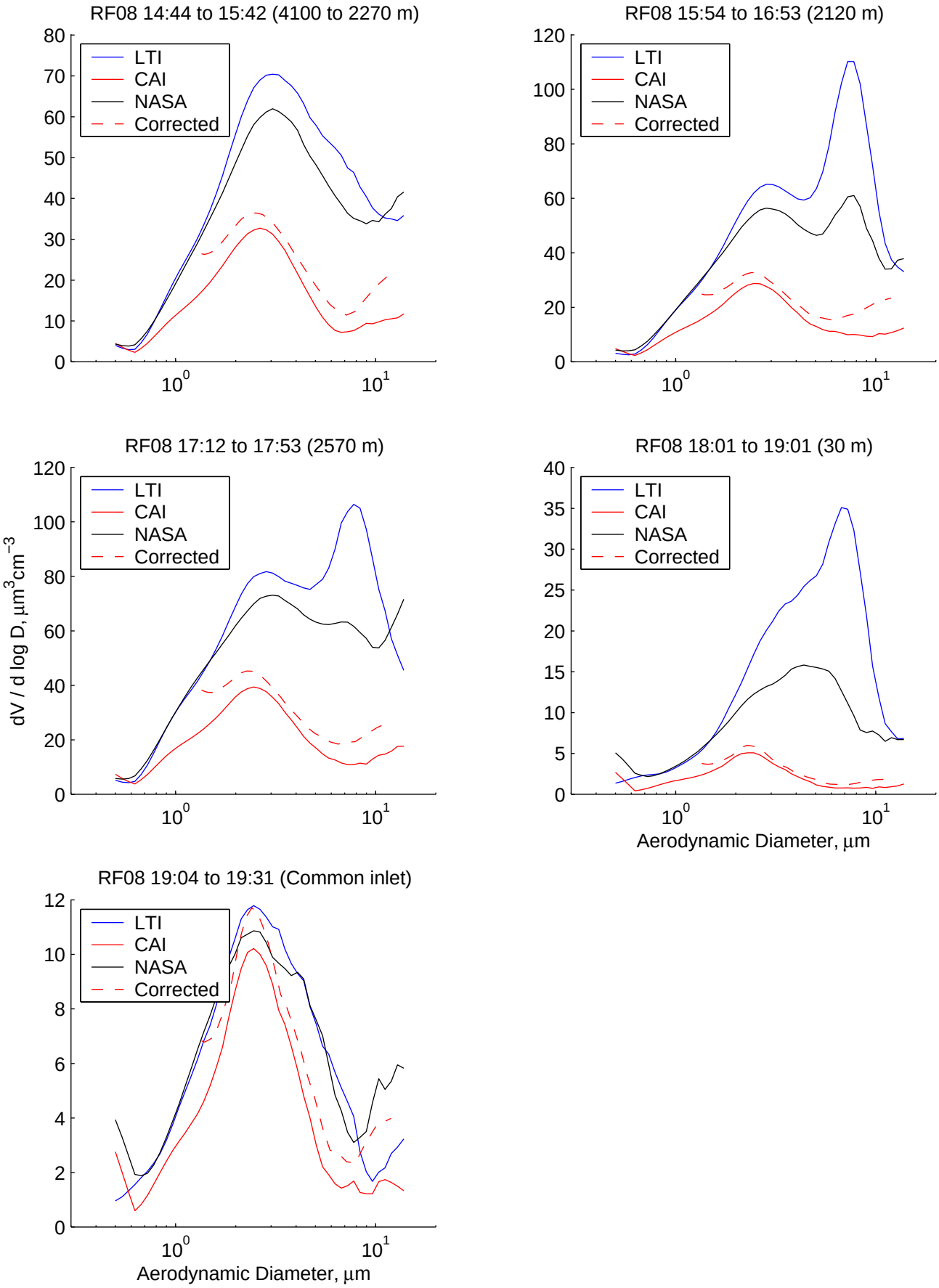
RF08 14:44 to 15:42 (4100 to 2270 m)
RF08 15:54 to 16:53 (2120 m)
RF08 17:12 to 17:53 (2570 m)
RF08 18:01 to 19:01 (30 m)
RF08 19:04 to 19:31 (Common inlet)
LTI
CAI
NASA
Corrected
dV / d log D, µm3cm−3
Aerodynamic Diameter, µm

Figure 3.5.5

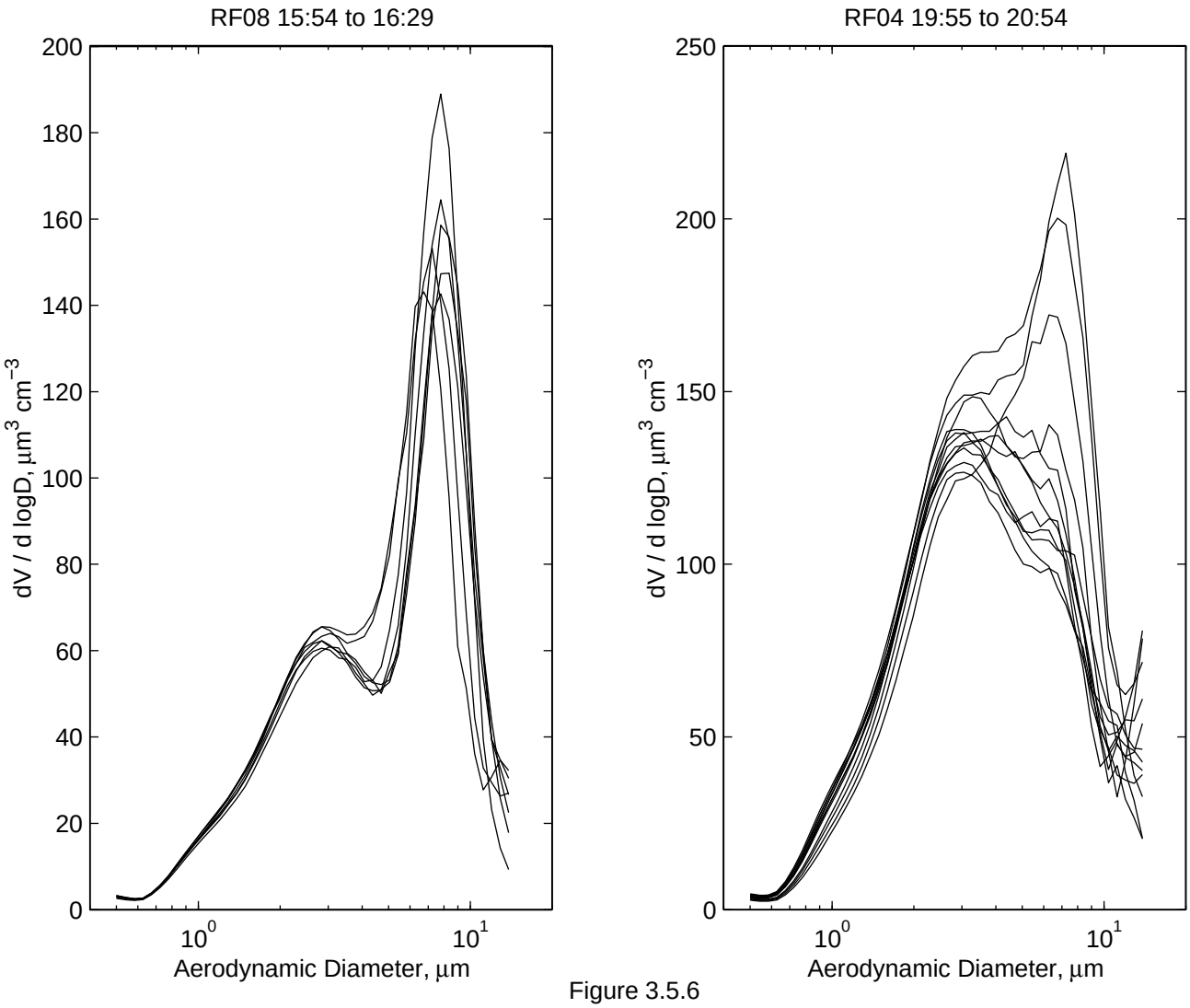
RF08 15:54 to 16:29
RF04 19:55 to 20:54
dV / d logD, µm3 cm−3
Aerodynamic Diameter, µm
0
20
40
60
80
100
120
140
160
180
200
250
150
50
10^0
10^1

Figure 3.5.6

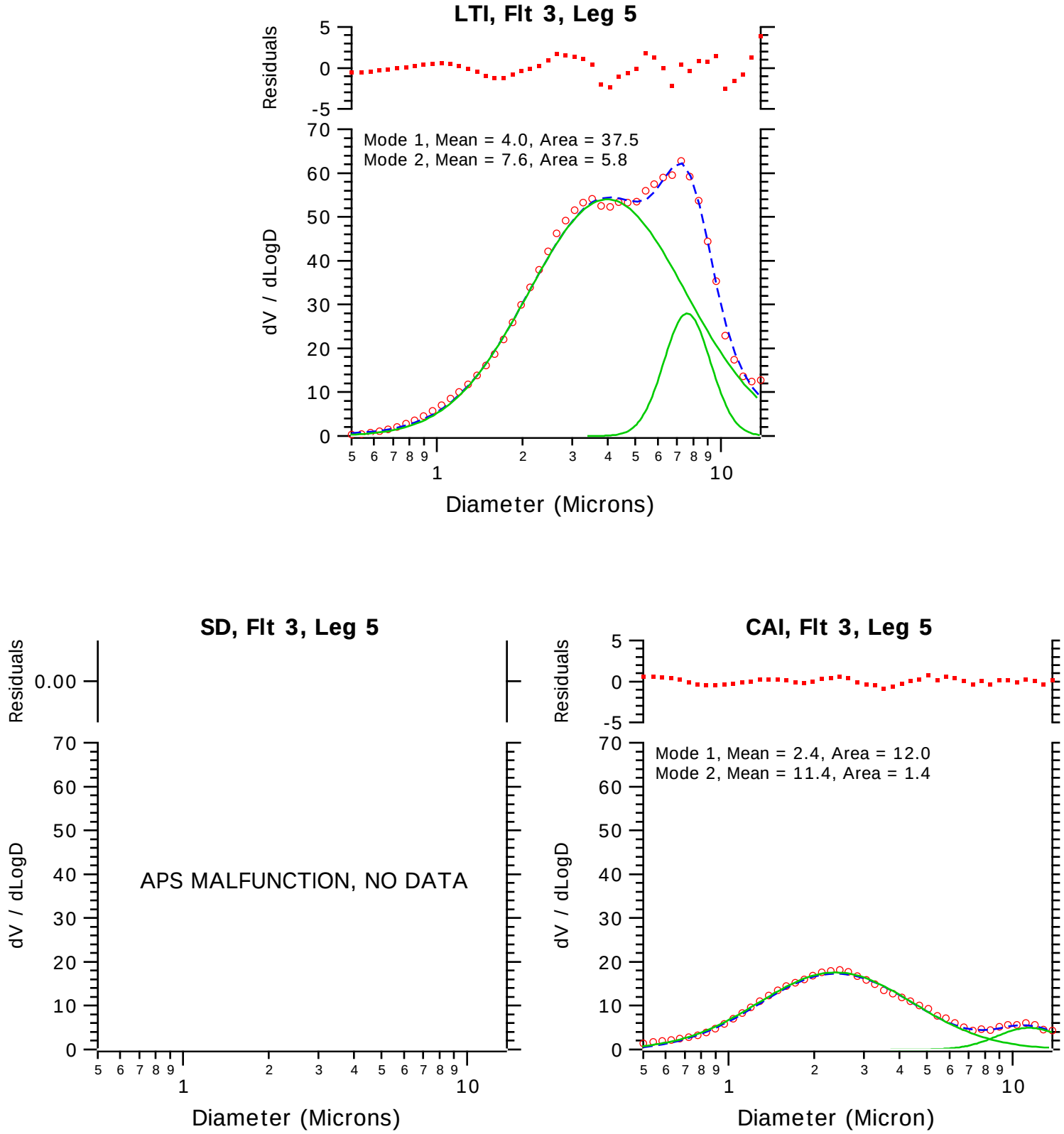

Figure 3.5.8 18:47-19:10 GMT, Laminar LTI @ 120 lpm, altitude = 60 m asl.

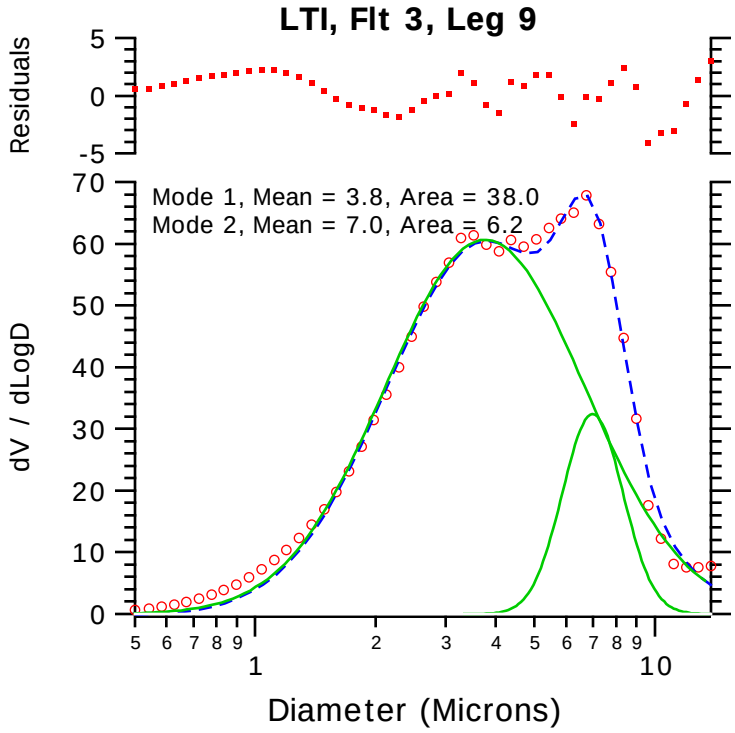

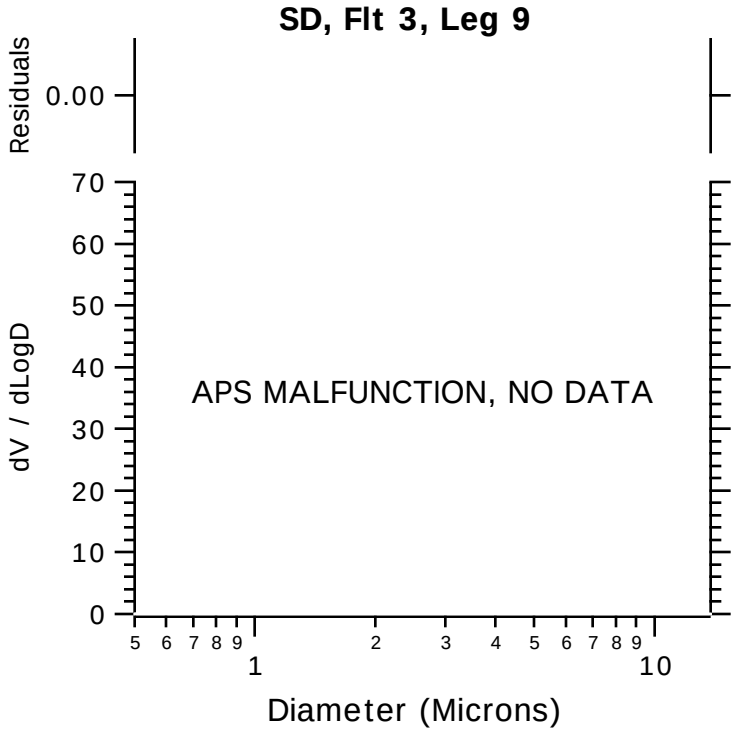

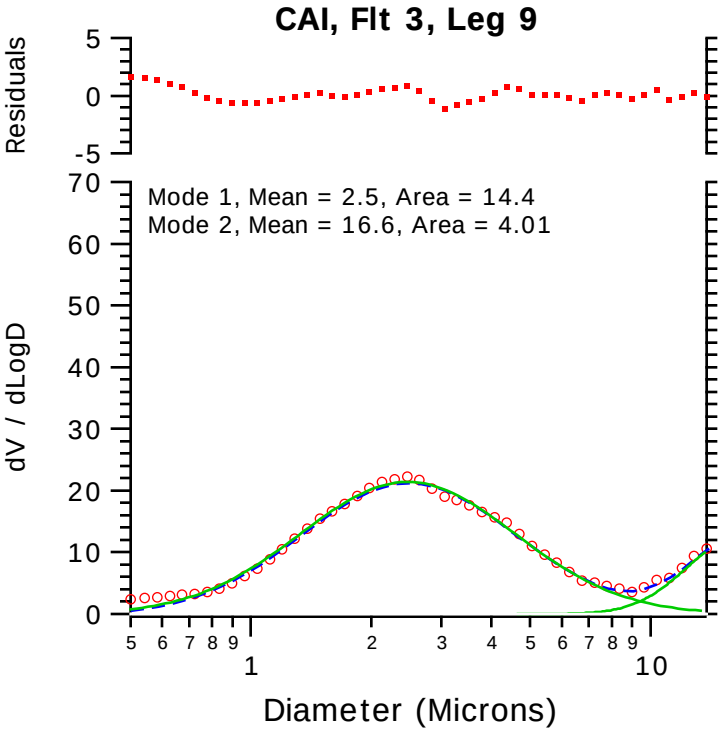

Figure 3.5.9 20:55-21:20 GMT, Turbulent LTI @ 214 lpm, altitude 60 m asl.

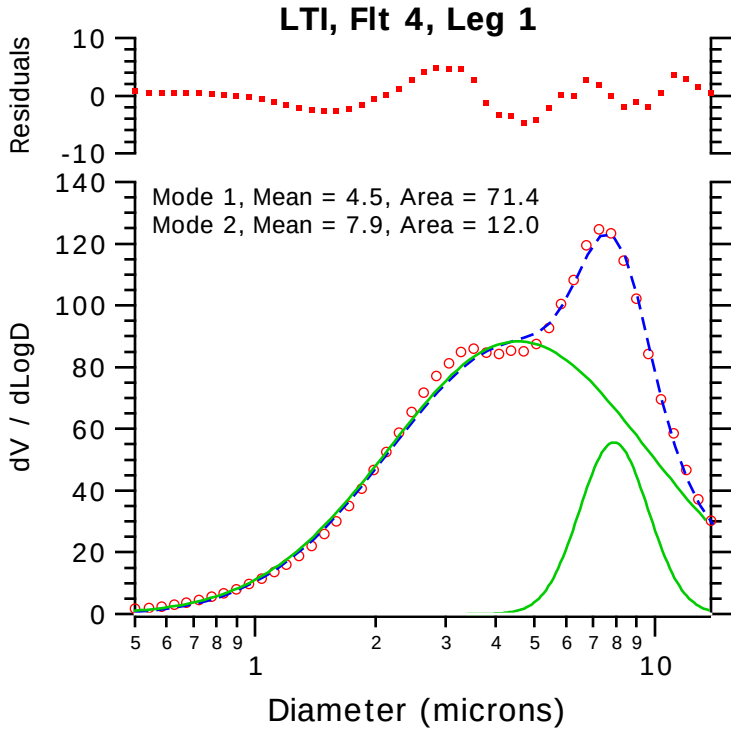

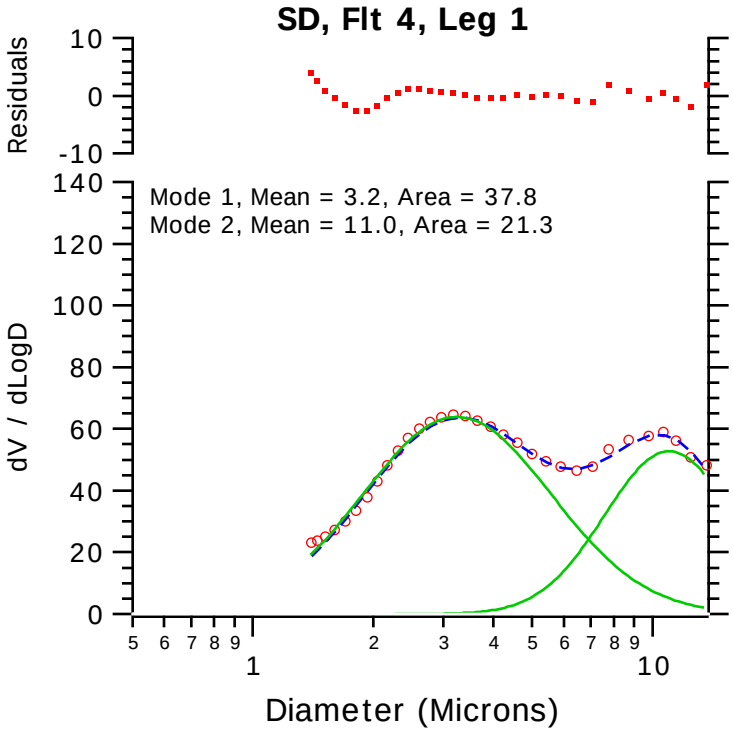

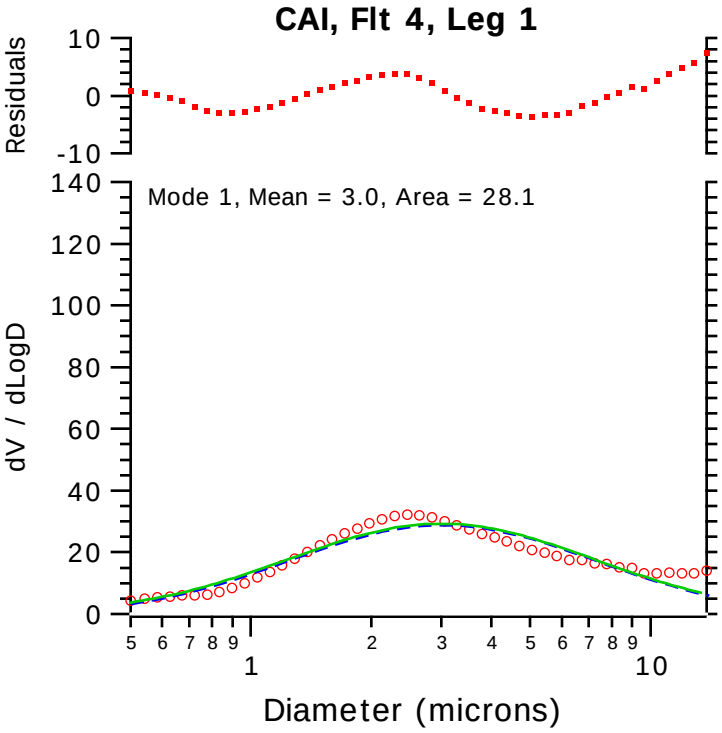

Figure 3.5.10 16:34-17:34 GMT, altitude 30 m asl

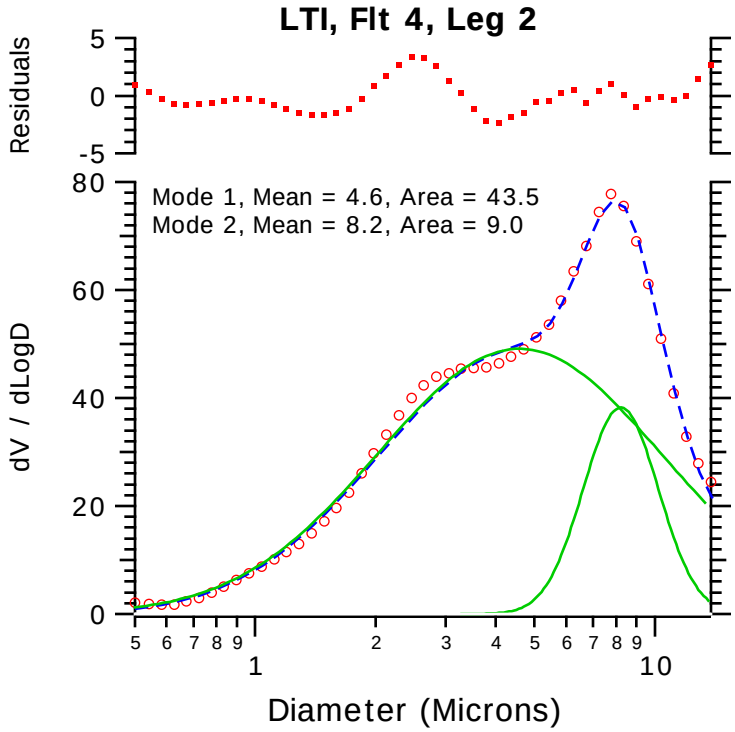

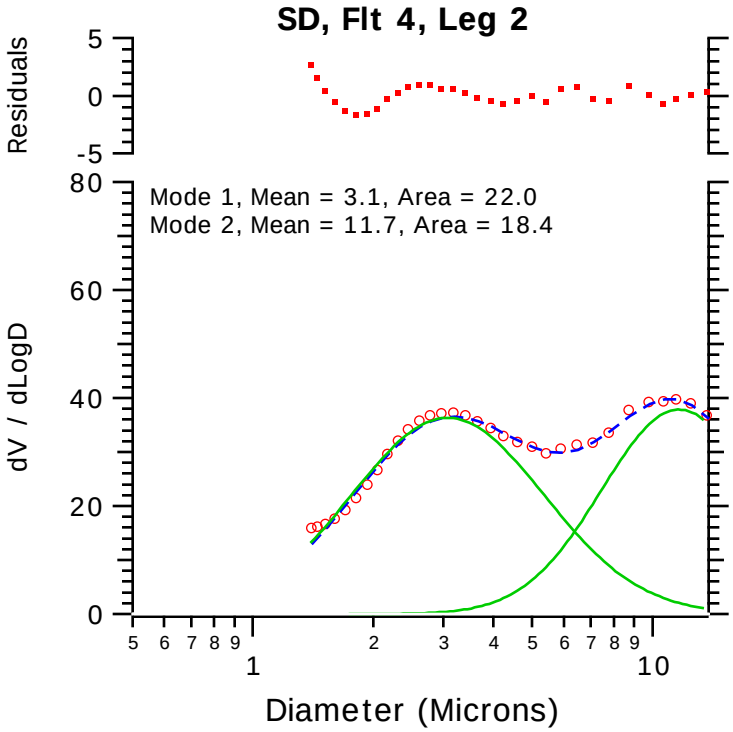

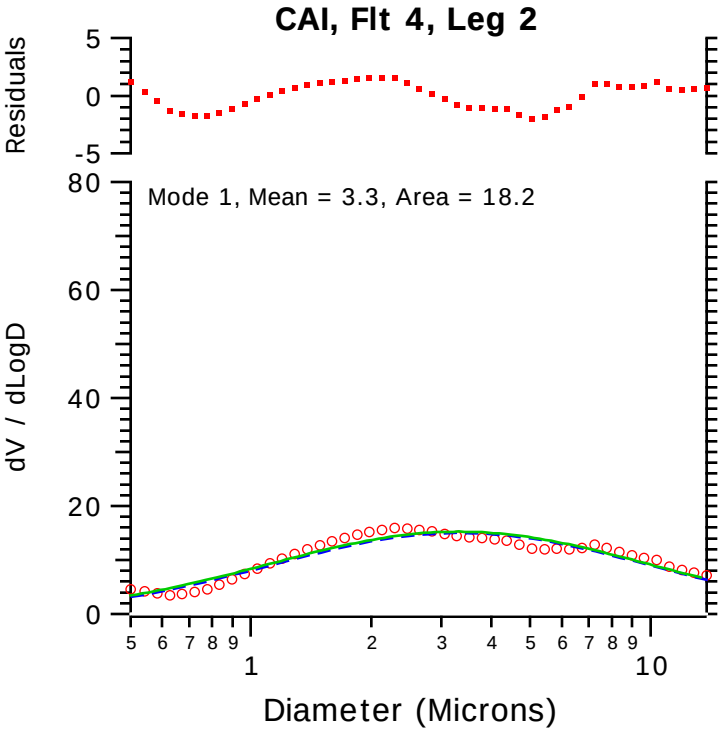

Figure 3.5.11 17:50-18:41 GMT, altitude 1060 m asl.

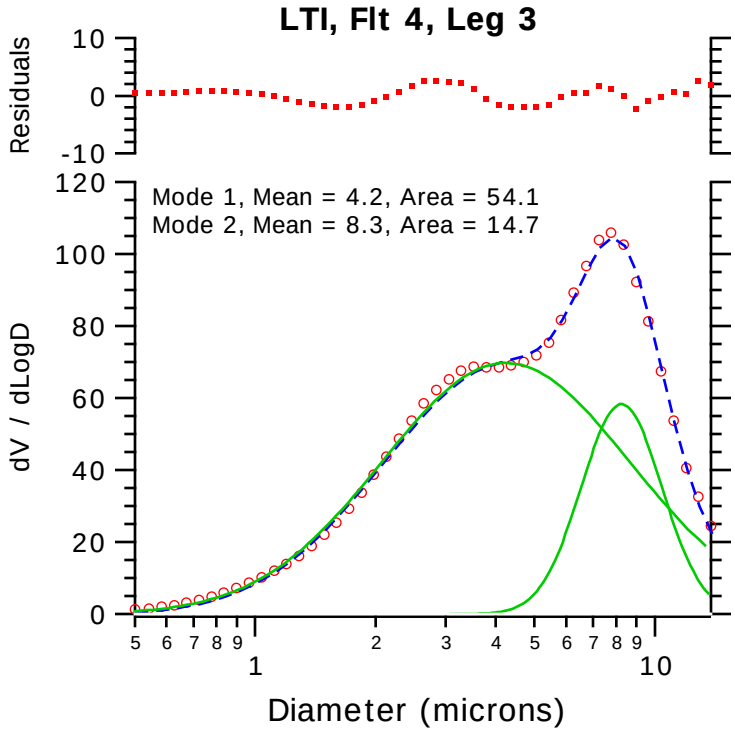

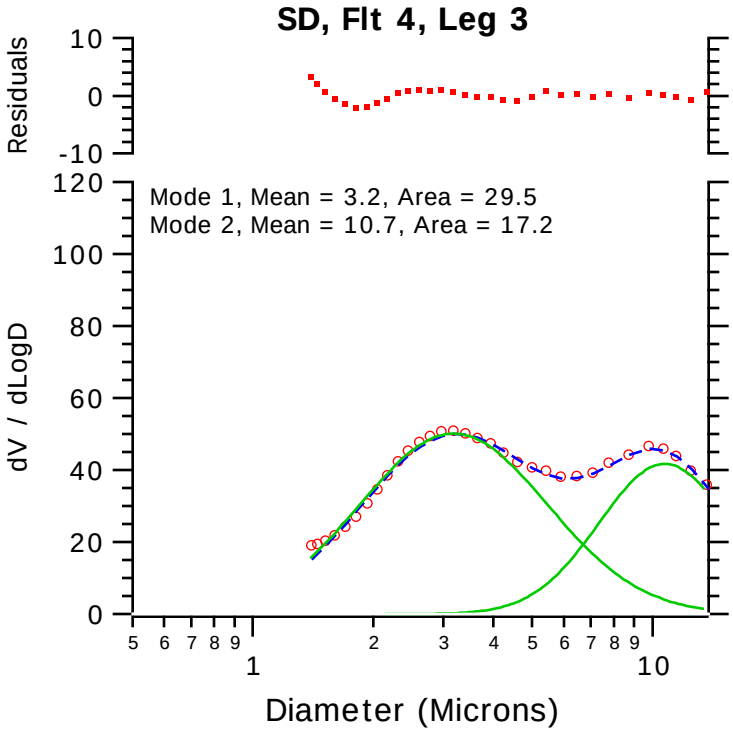

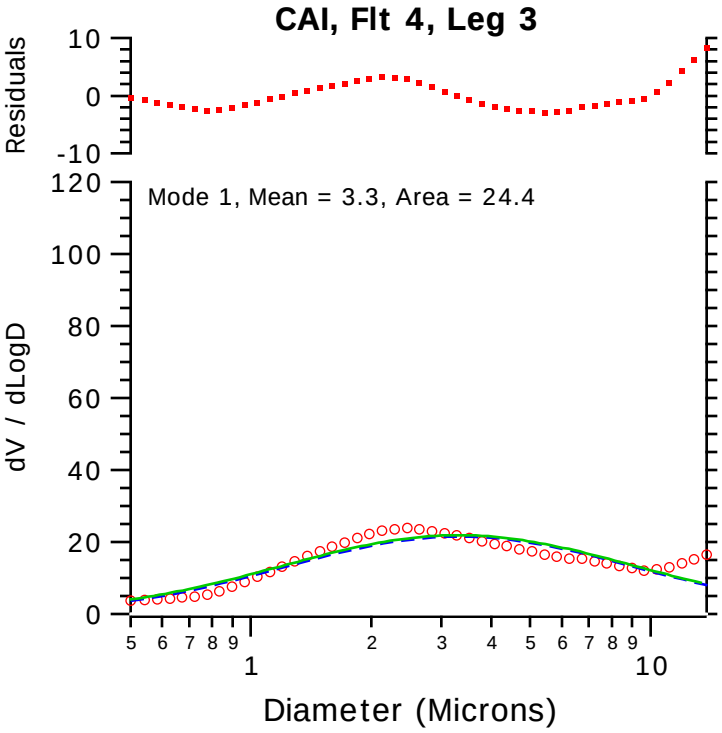

Figure 3.5.12 18:47-19:46 GMT, altitude 90 m asl.

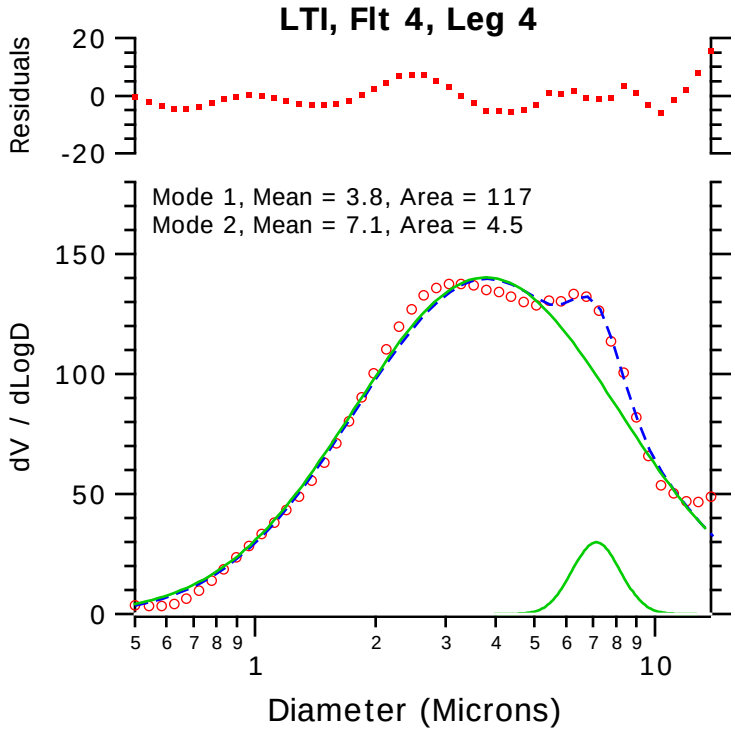

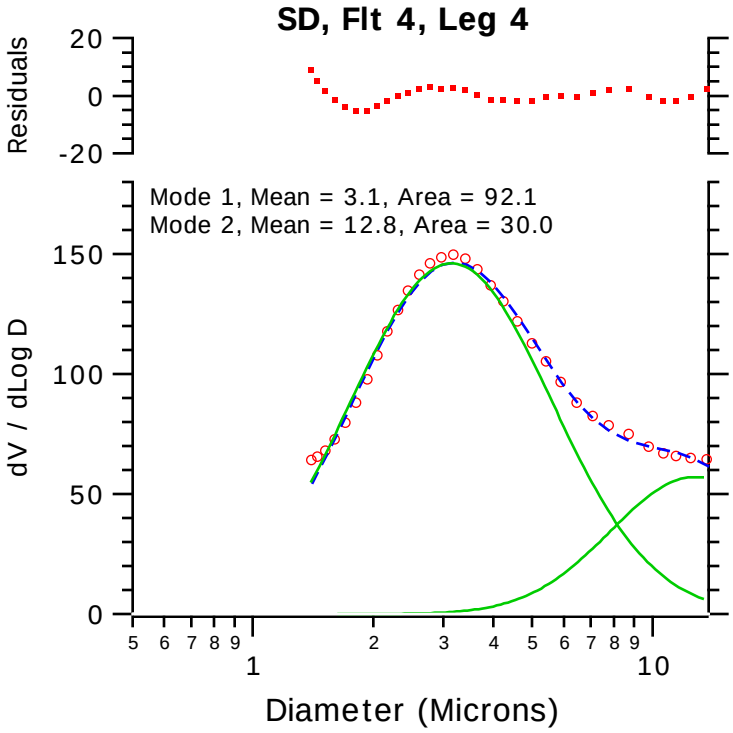

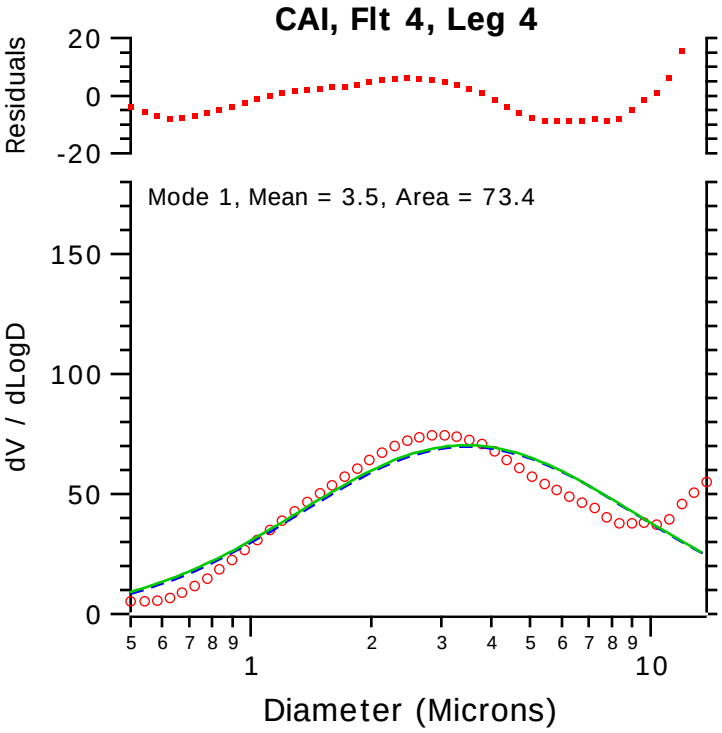

Figure 3.5.13 19:55-20:54 GMT, altitude 2000 m asl.

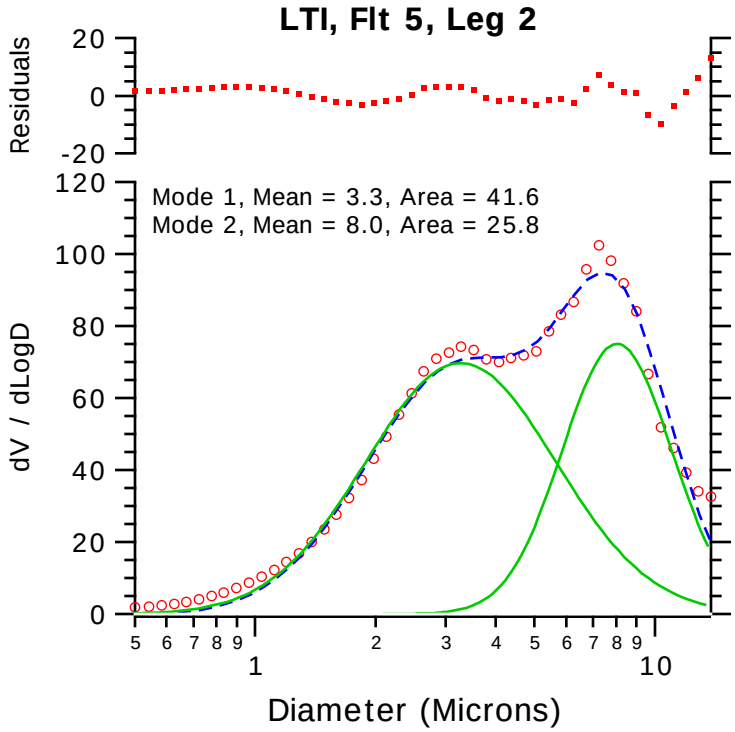

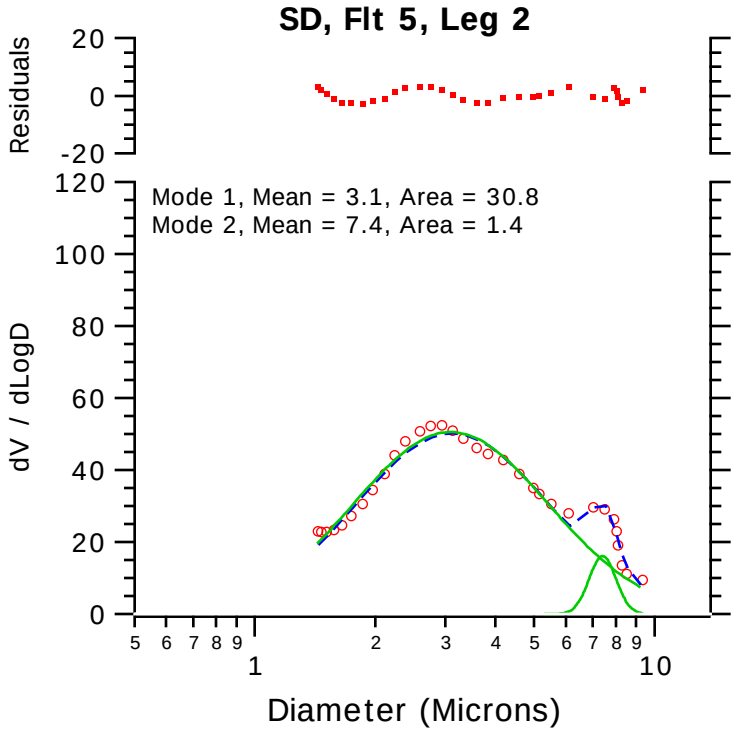

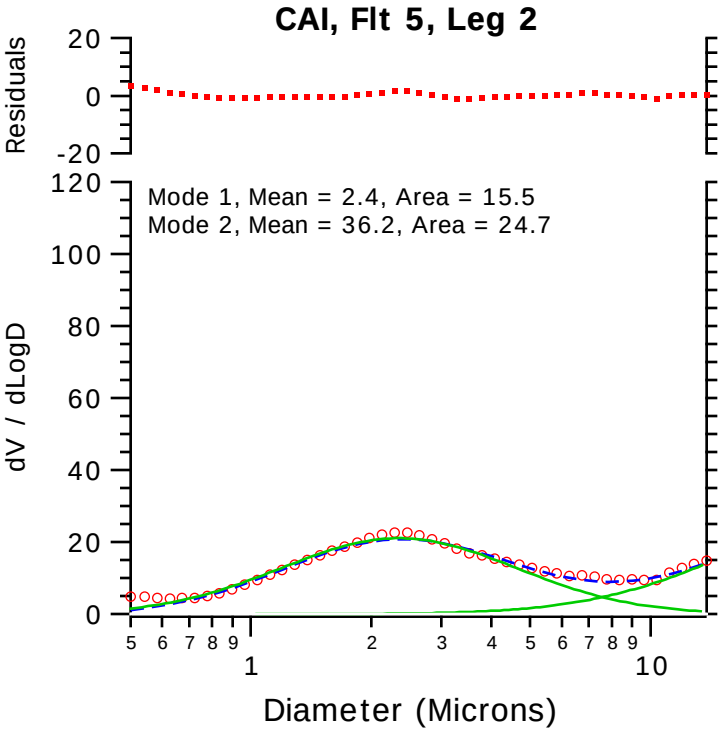

Figure 3.5.14 16:21-16:44 GMT, laminar LTI @ 120 lpm, altitude 300 m asl.

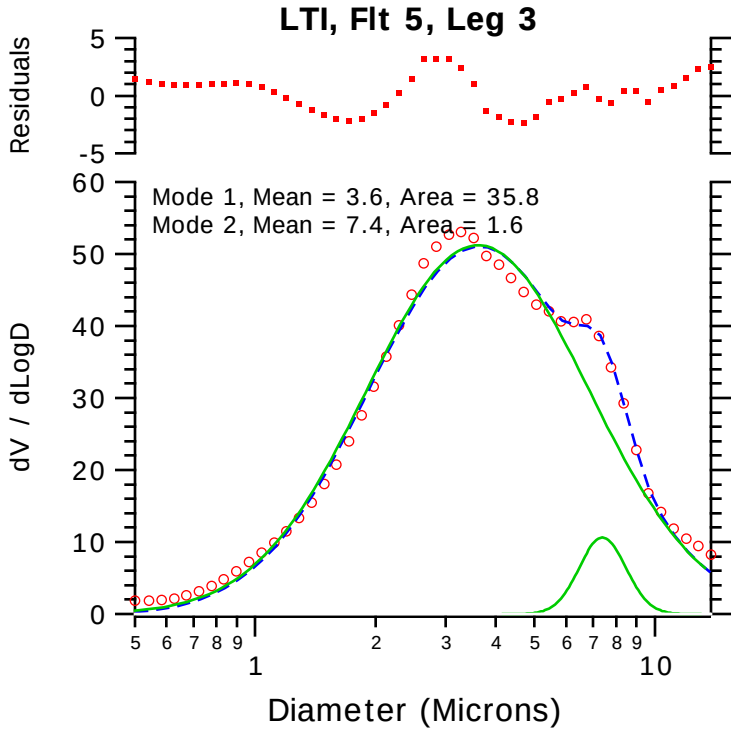

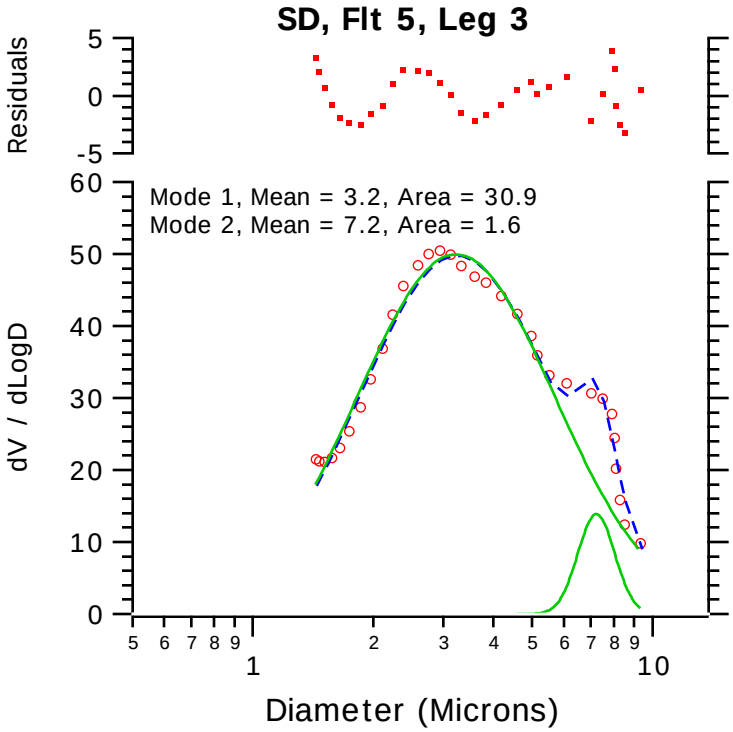

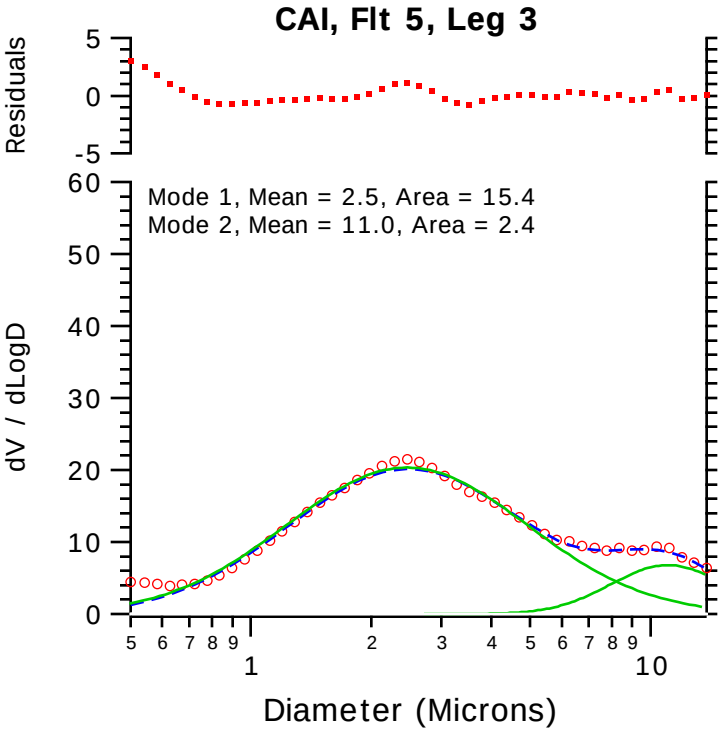

Figure 3.5.15 16:59-17:20 GMT, turbulent LTI @ 200 lpm, altutude 300 m asl.

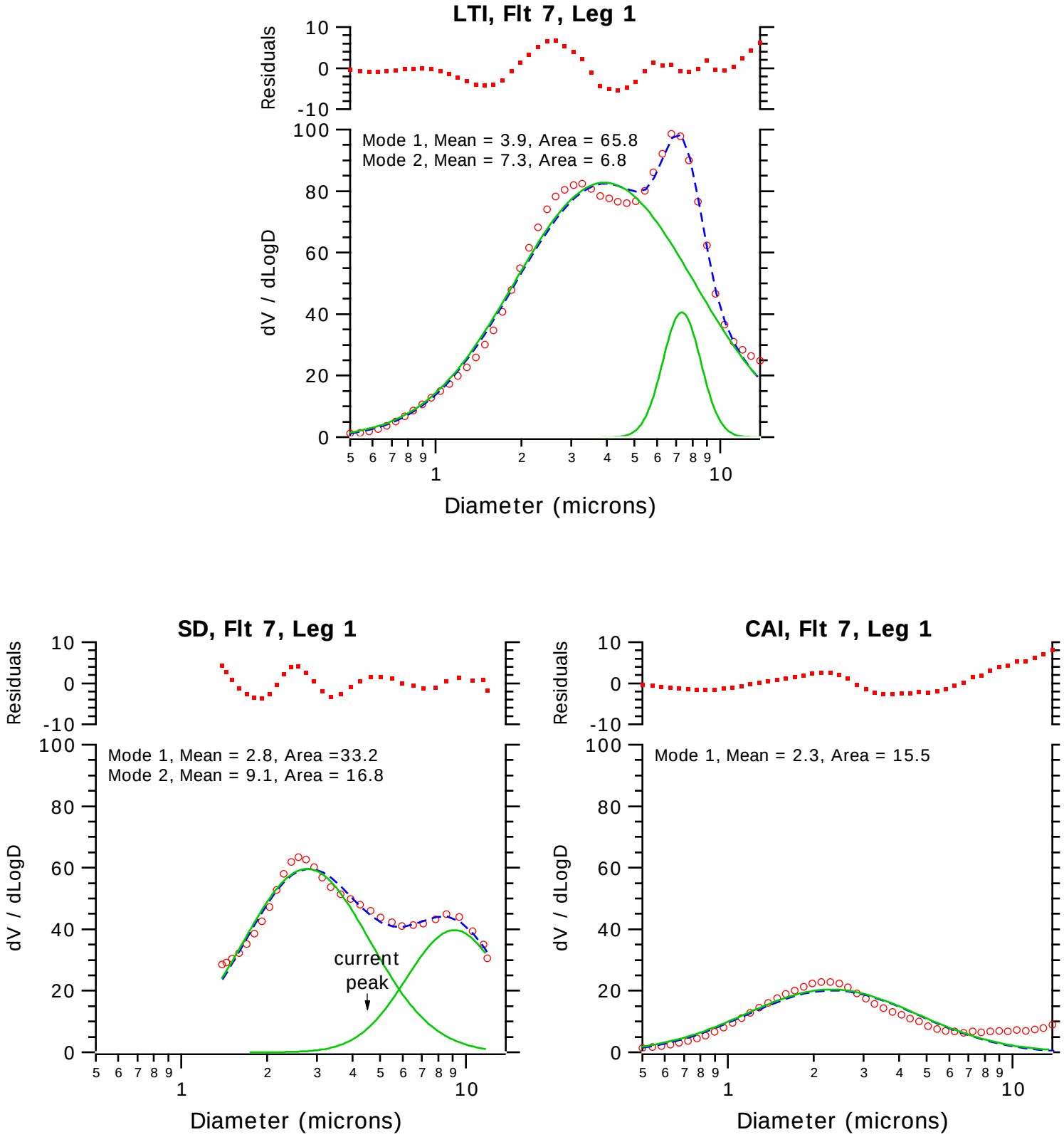

Figure 3.5.16 15:36-16:20 GMT, laminar LTI @ 120 lpm, altitude 30 m asl.

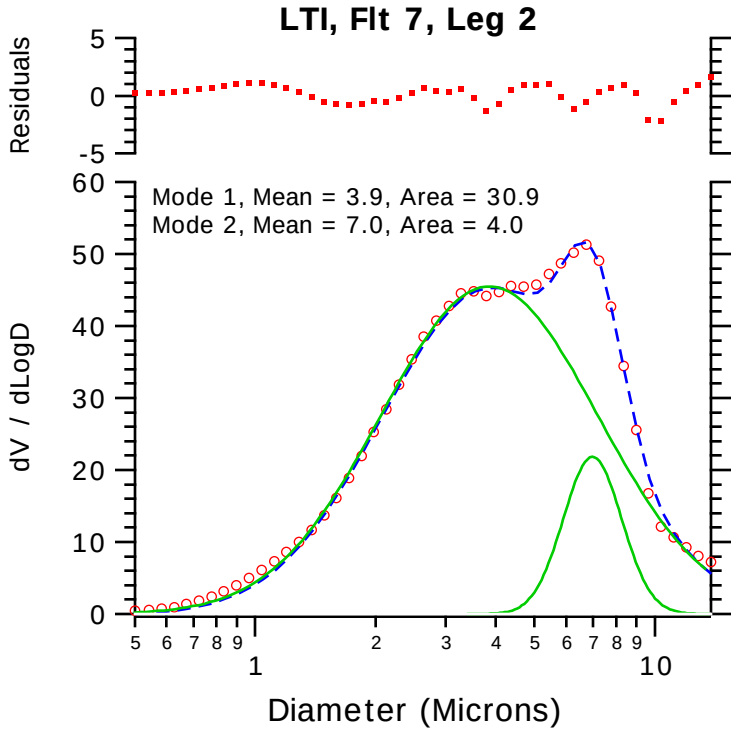

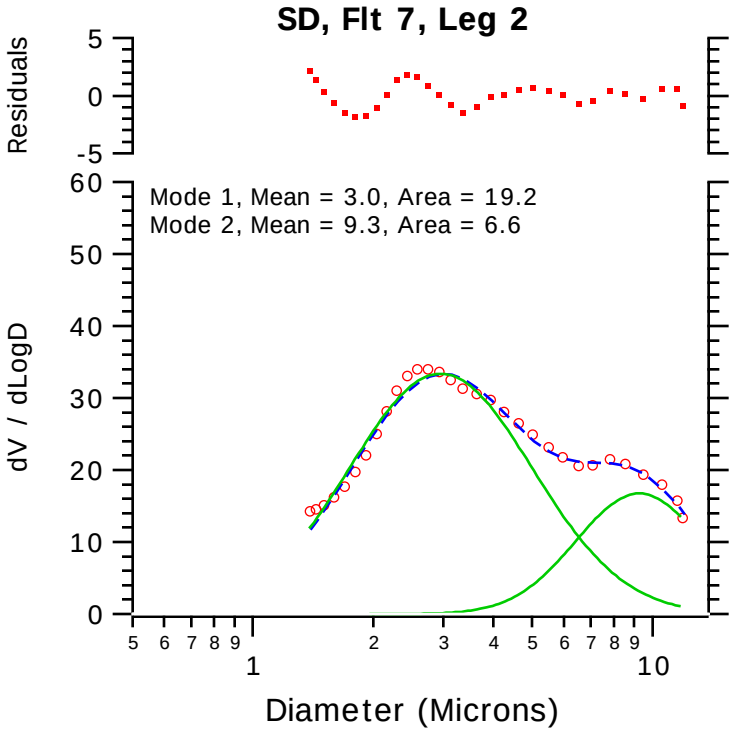

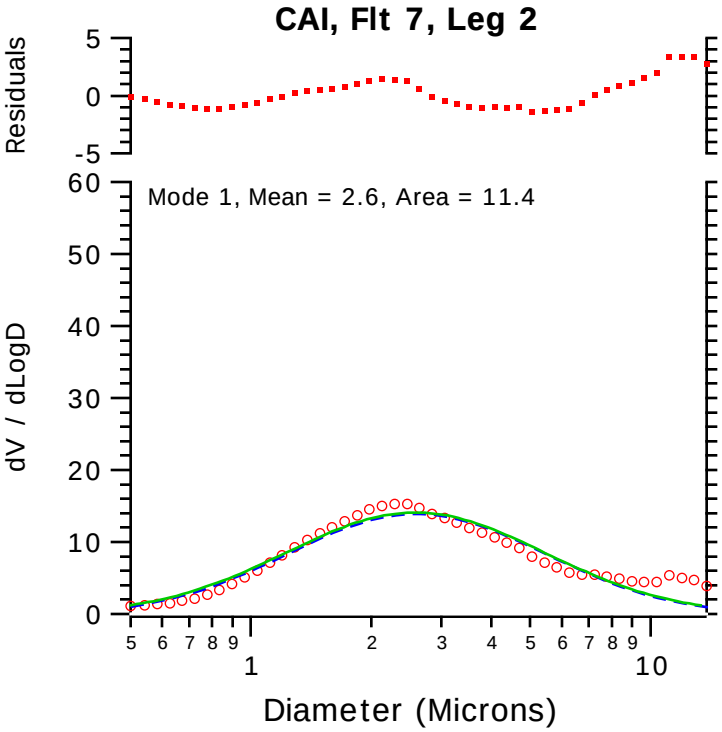

Figure 3.5.17 16:28-17:20 GMT, turbulent LTI @ 200 lpm, altitude 30 m asl.

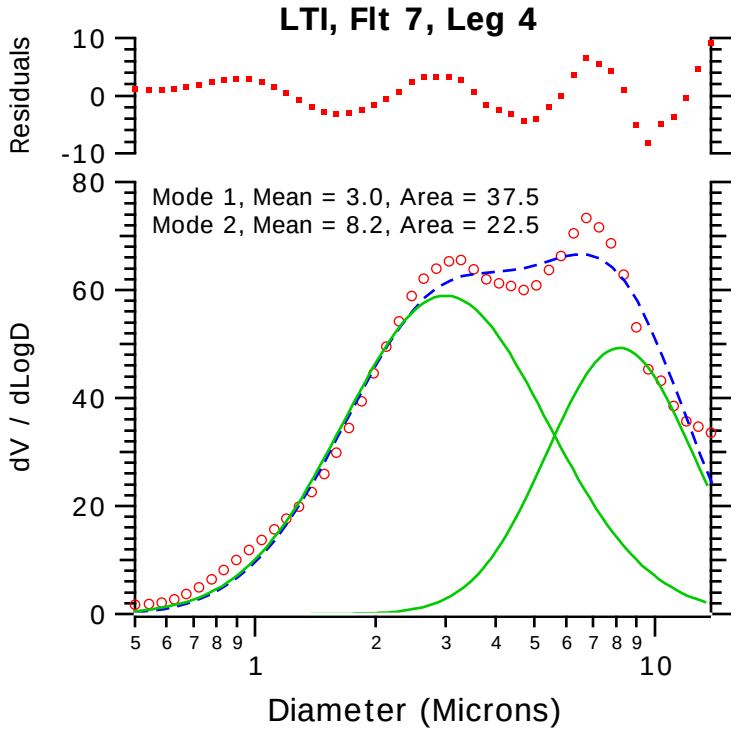

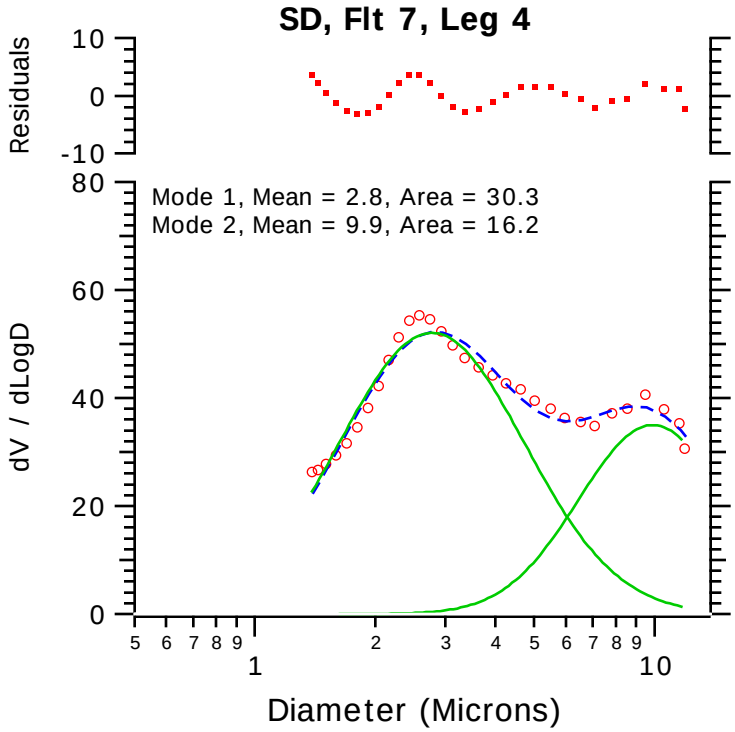

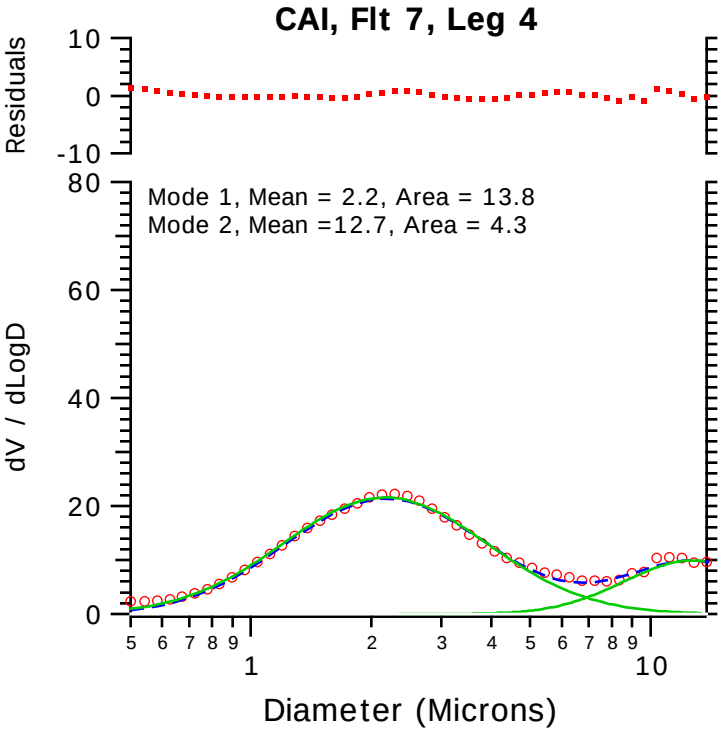

Figure 3.5.18 18:57-19:38 GMT, laminar LTI @ 120? lpm, altitude 230 m asl.

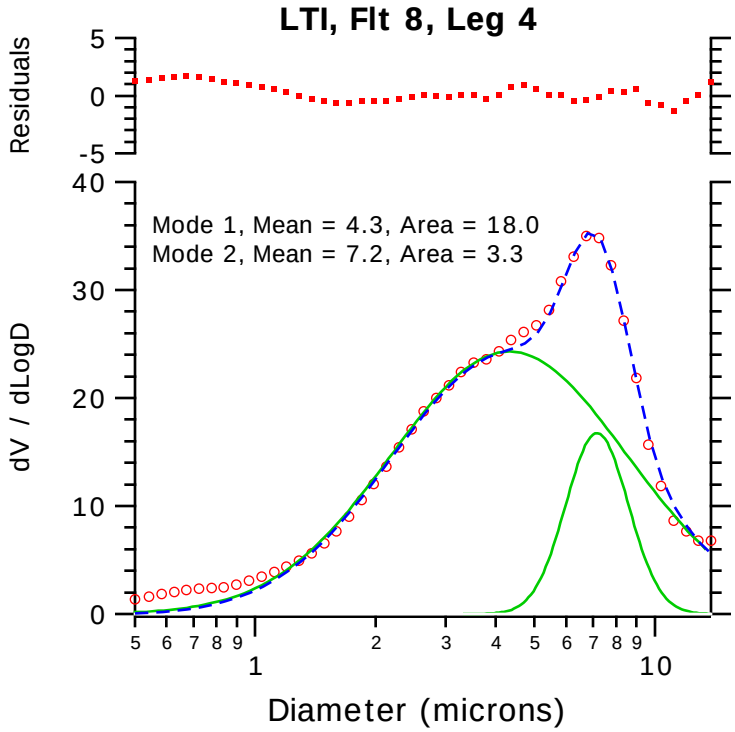

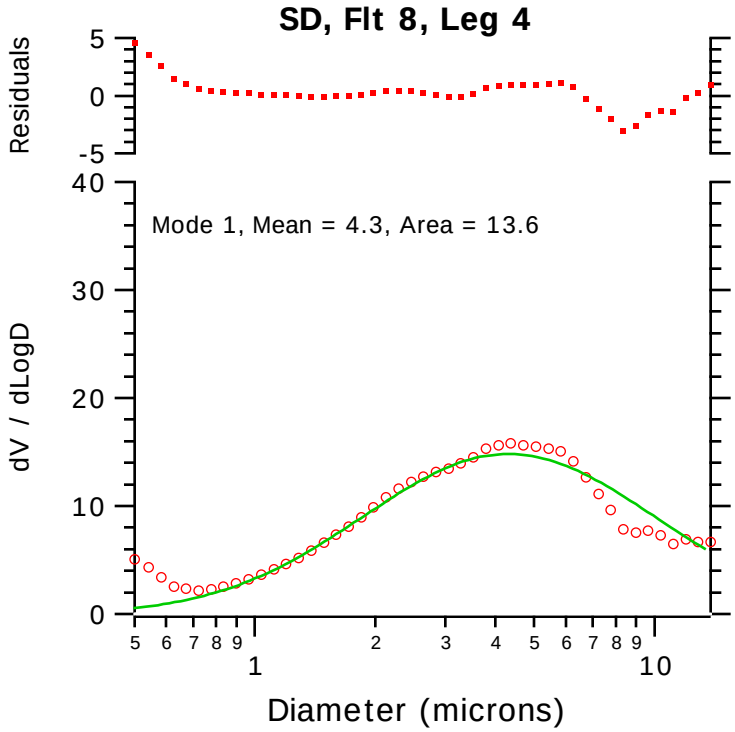

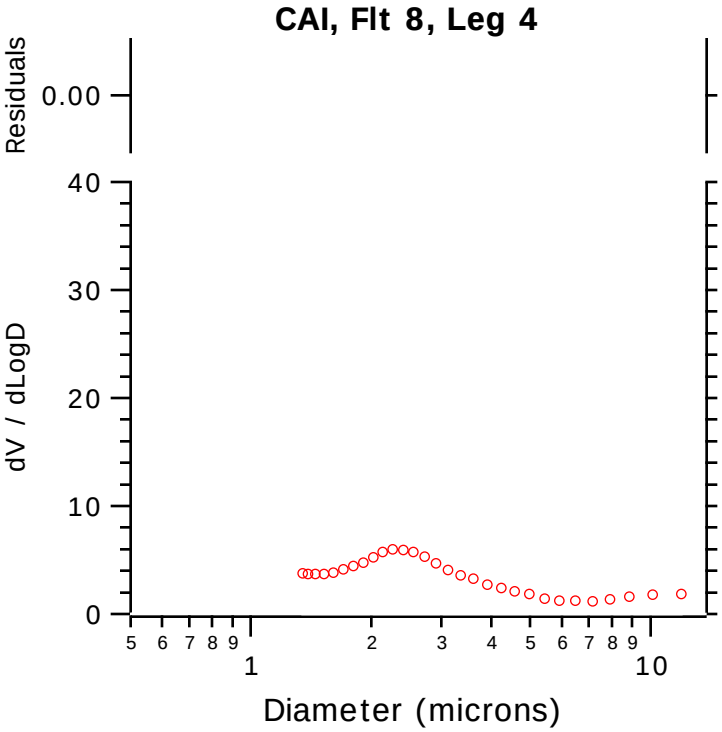

Figure 3.5.19 18:00-19:01 GMT, altitude 30 m asl.

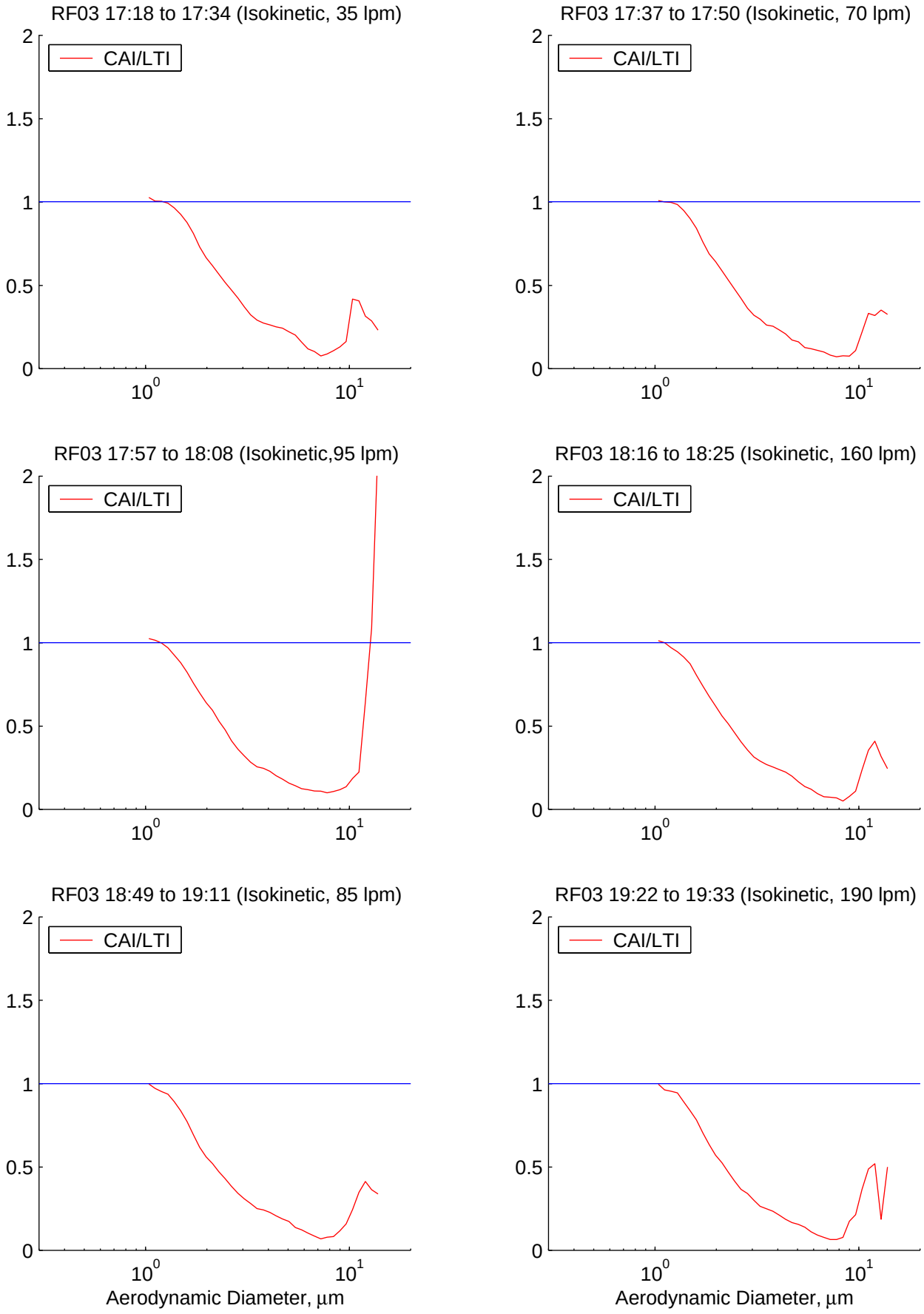
RF03 17:18 to 17:34 (Isokinetic, 35 lpm)
RF03 17:37 to 17:50 (Isokinetic, 70 lpm)
RF03 17:57 to 18:08 (Isokinetic,95 lpm)
RF03 18:16 to 18:25 (Isokinetic, 160 lpm)
RF03 18:49 to 19:11 (Isokinetic, 85 lpm)
RF03 19:22 to 19:33 (Isokinetic, 190 lpm)
CAI/LTI
2
1.5
1
0.5
0
10^0
10^1
Aerodynamic Diameter, µm

Figure 3.5.20

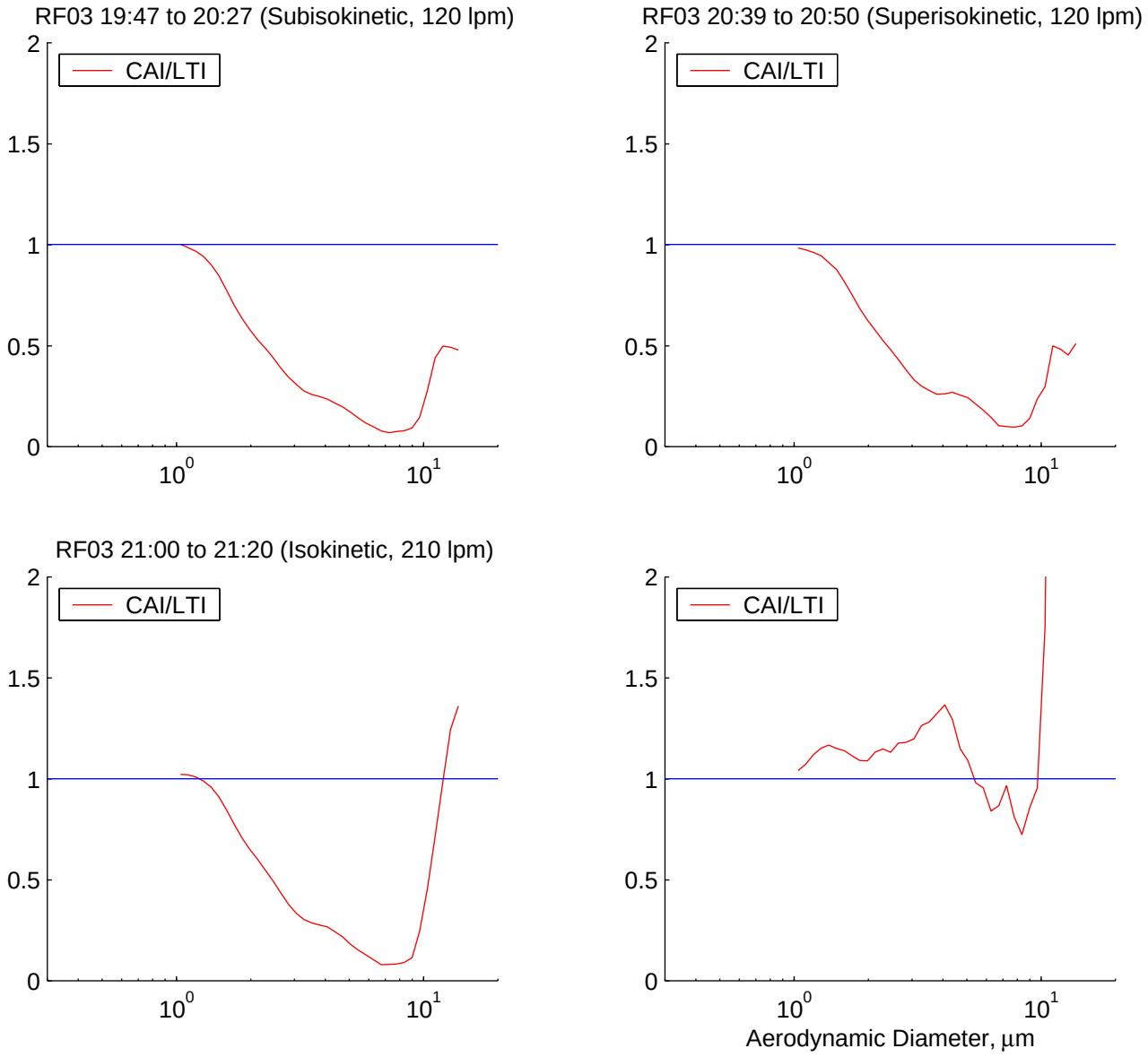

Figure .5.20 cont'd.

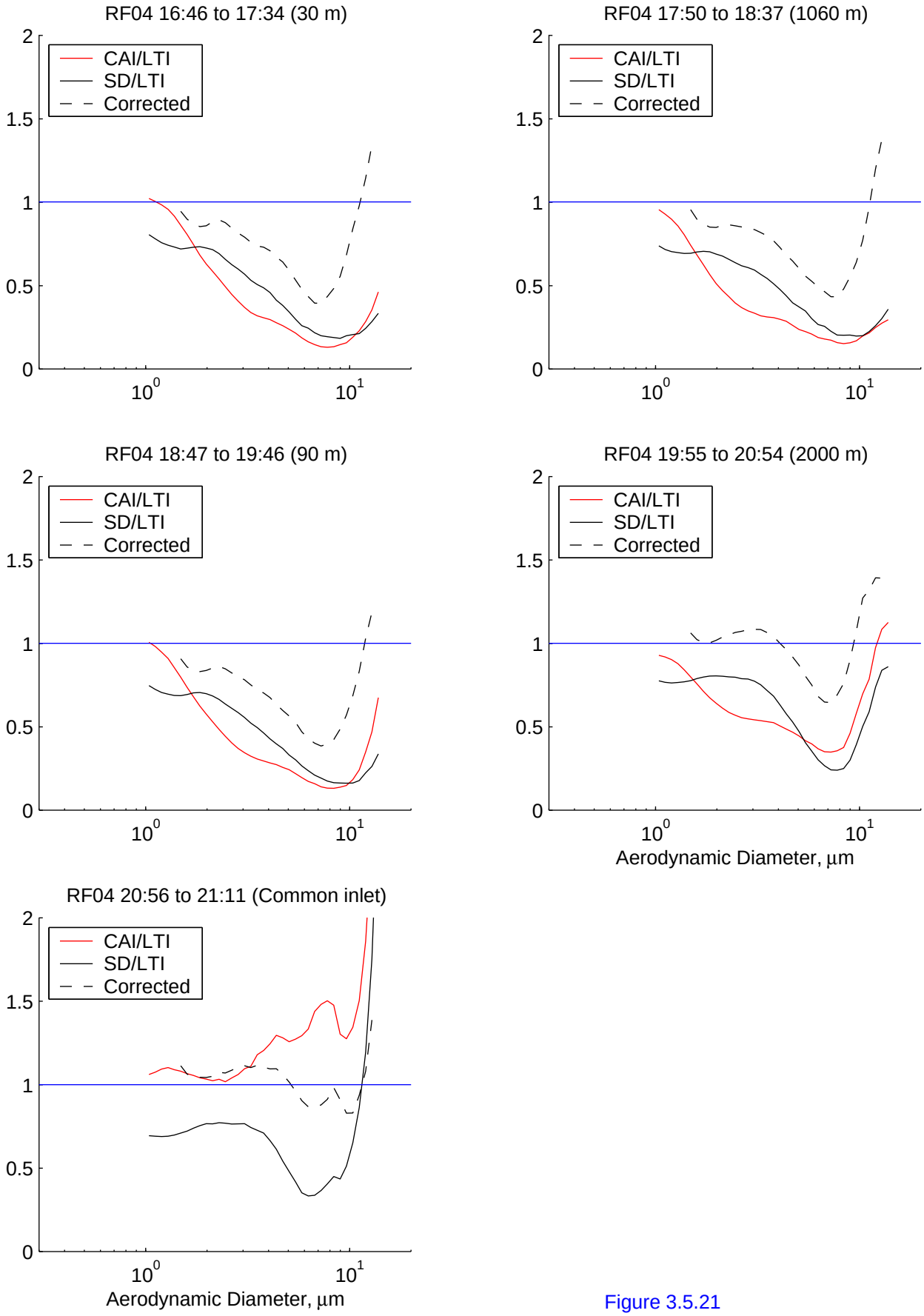
RF04 16:46 to 17:34 (30 m)
RF04 17:50 to 18:37 (1060 m)
RF04 18:47 to 19:46 (90 m)
RF04 19:55 to 20:54 (2000 m)
RF04 20:56 to 21:11 (Common inlet)
CAI/LTI
SD/LTI
Corrected
0
0.5
1
1.5
2
10^0
10^1
Aerodynamic Diameter, µm

Figure 3.5.21

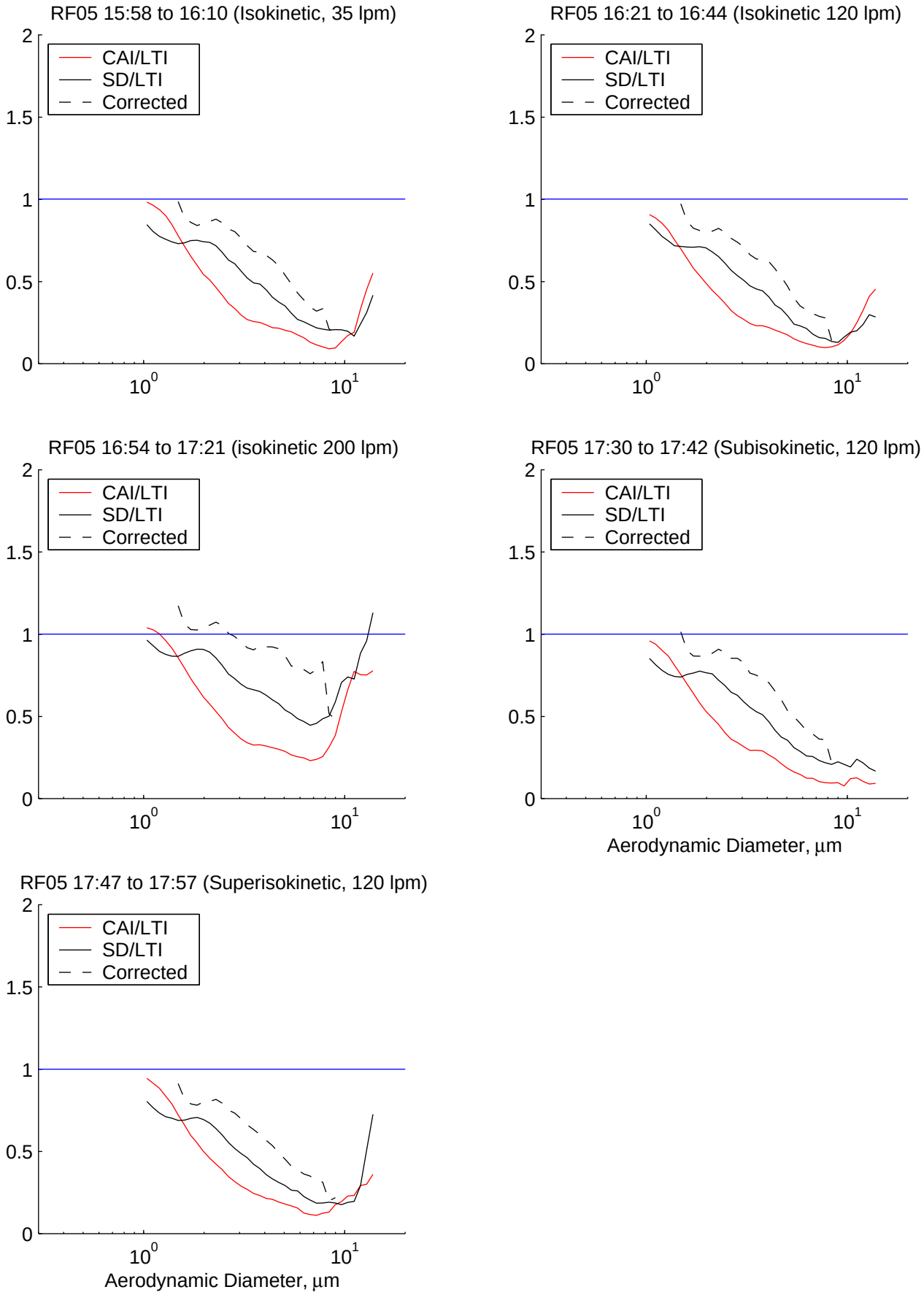
RF05 15:58 to 16:10 (Isokinetic, 35 lpm)
RF05 16:21 to 16:44 (Isokinetic 120 lpm)
RF05 16:54 to 17:21 (isokinetic 200 lpm)
RF05 17:30 to 17:42 (Subisokinetic, 120 lpm)
RF05 17:47 to 17:57 (Superisokinetic, 120 lpm)
CAI/LTI
SD/LTI
Corrected
2
1.5
1
0.5
0
10^0
10^1
Aerodynamic Diameter, µm

Figure 3.5.22

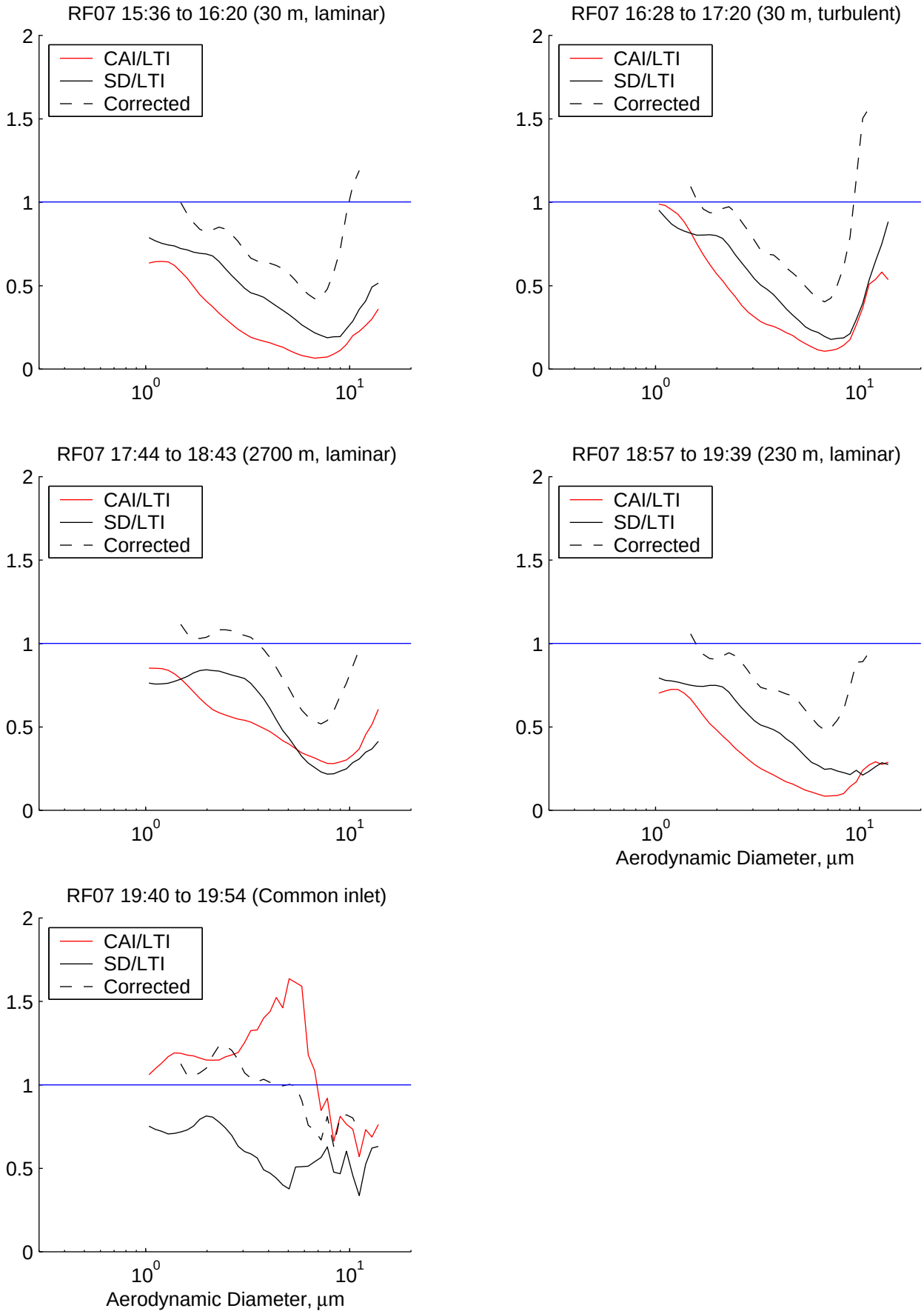
RF07 15:36 to 16:20 (30 m, laminar)
RF07 16:28 to 17:20 (30 m, turbulent)
RF07 17:44 to 18:43 (2700 m, laminar)
RF07 18:57 to 19:39 (230 m, laminar)
RF07 19:40 to 19:54 (Common inlet)
CAI/LTI
SD/LTI
Corrected
2
1.5
1
0.5
0
10^0
10^1
Aerodynamic Diameter, µm

Figure 3.5.23

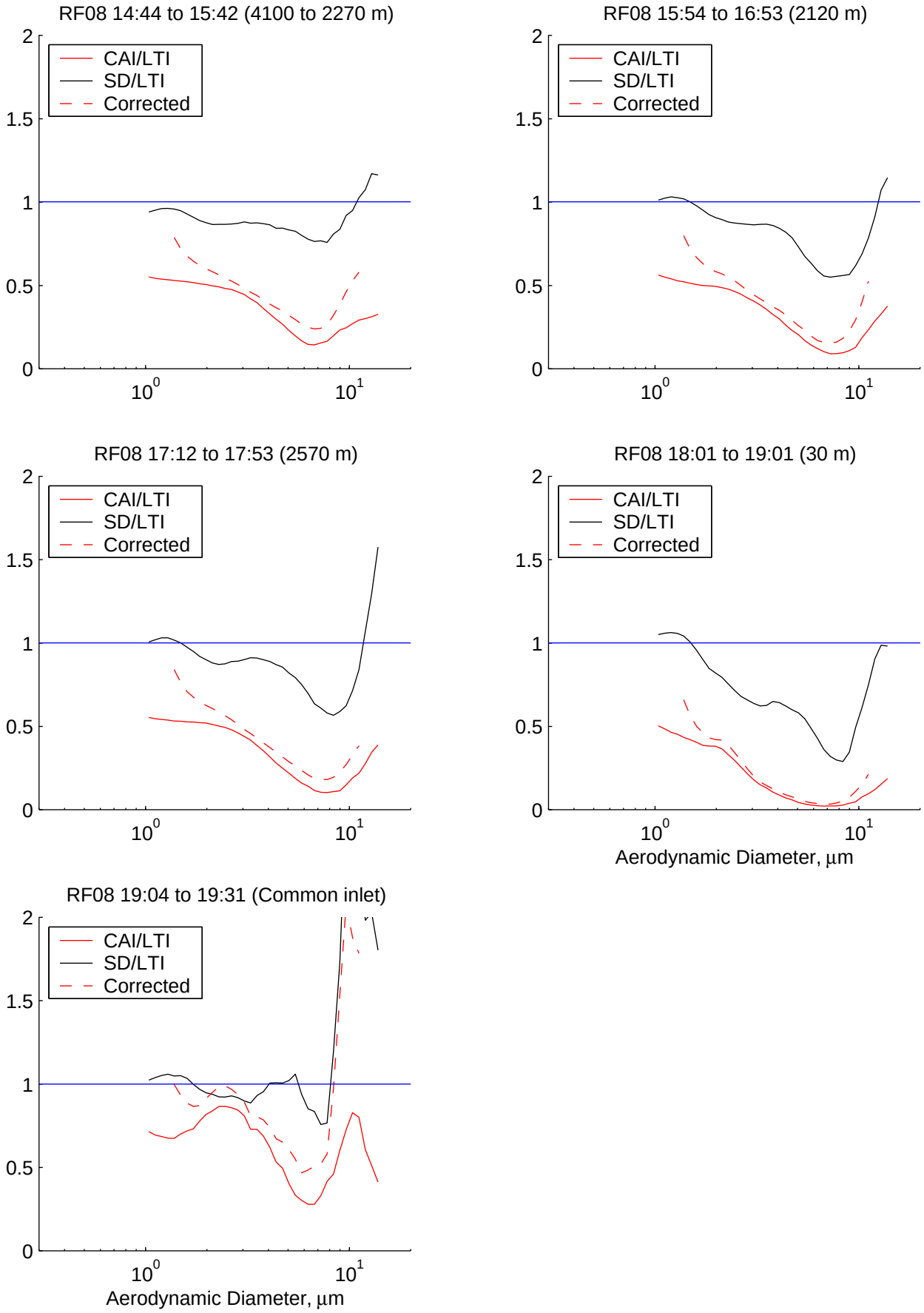
RF08 14:44 to 15:42 (4100 to 2270 m)
RF08 15:54 to 16:53 (2120 m)
RF08 17:12 to 17:53 (2570 m)
RF08 18:01 to 19:01 (30 m)
RF08 19:04 to 19:31 (Common inlet)
CAI/LTI
SD/LTI
Corrected
2
1.5
1
0.5
0
10^0
10^1
Aerodynamic Diameter, µm

Figure 3.5.24

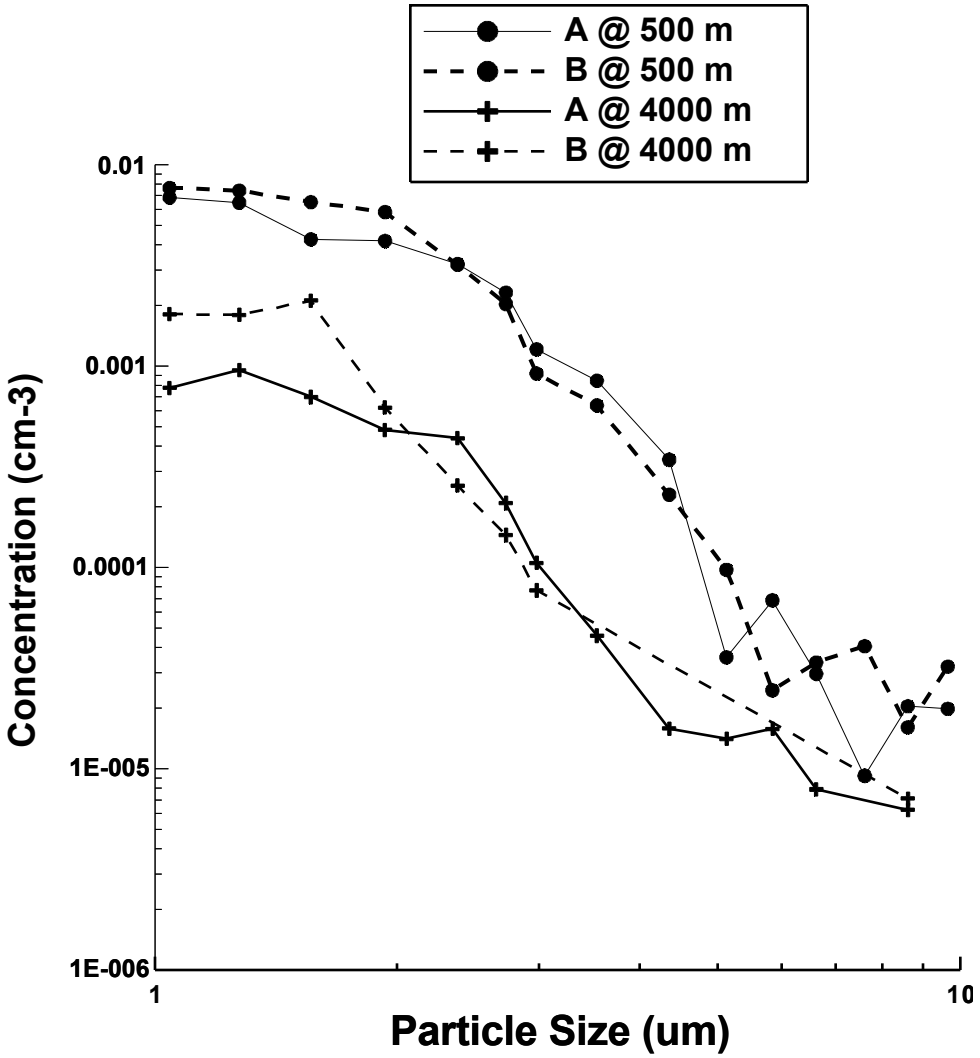

Figure 3.6.1 Comparison of FSSPs when both were wing-mounted

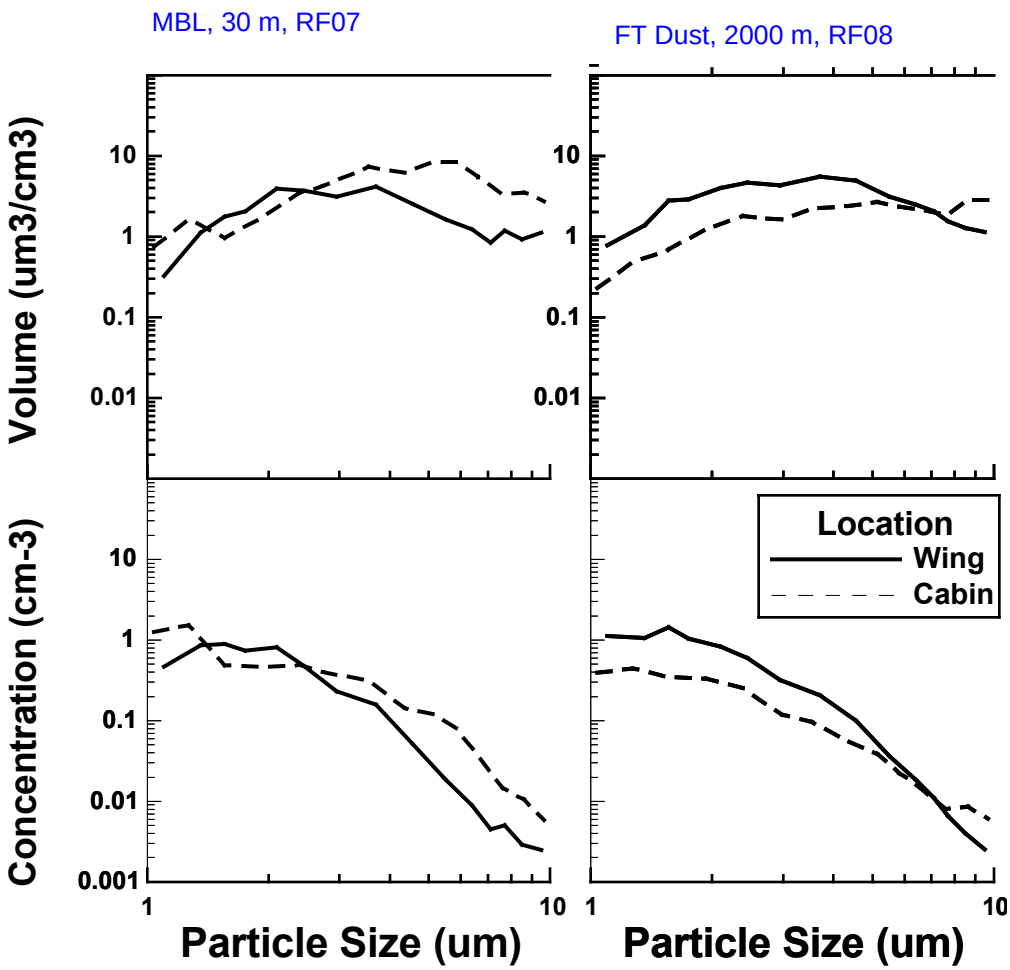

Figure 3.6.2, Wing and Cabin FSSPs, with corrections for airspeed.

In some circumstances and sizes the cabin 300 counted more particles, while in others the wing 300 recorded higher counts. The resulting ratios are out of the range that can be explained by numerical modeling, leading us to question the impact of the modified flow path in the cabin FSSP on its response.

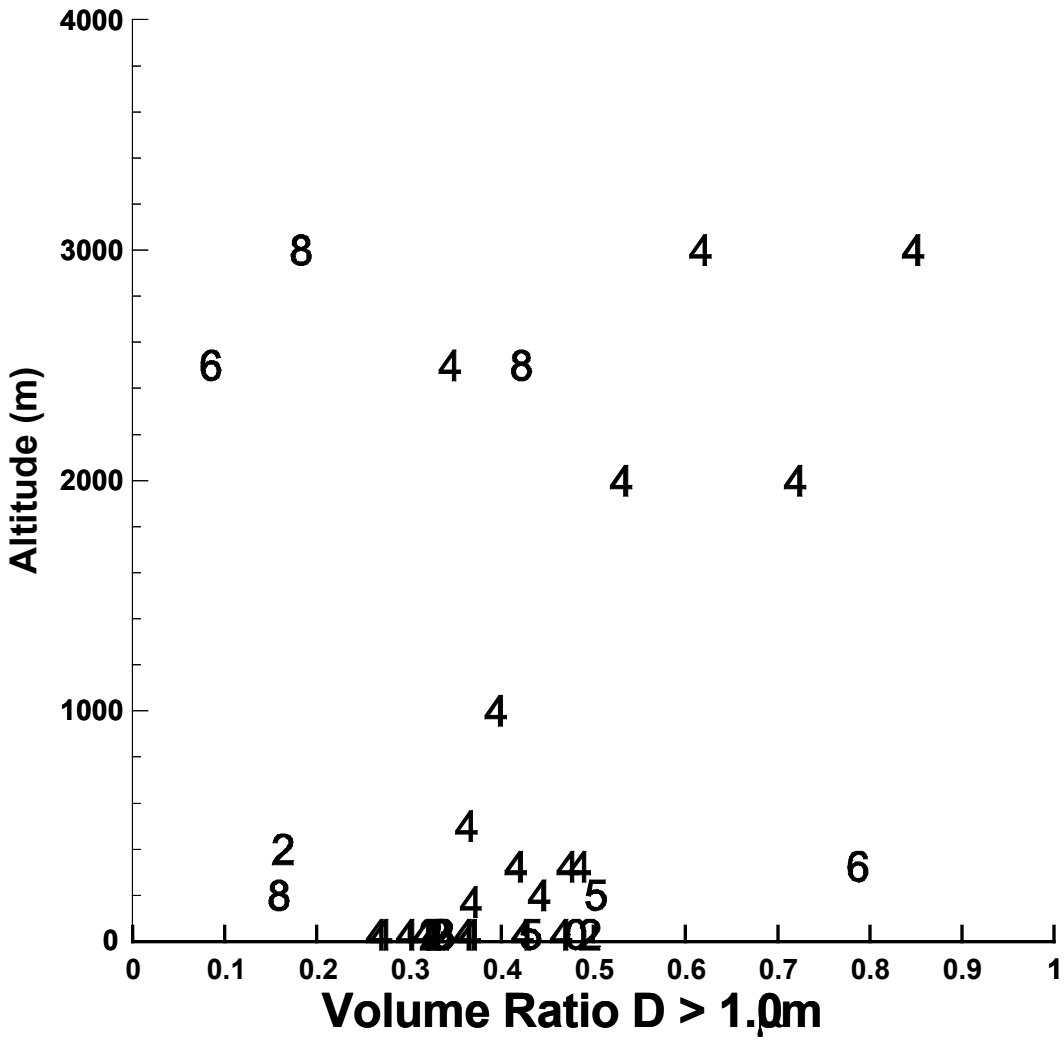

Figure 3.6.3 FSSP Wing/Internal Volume Ratio, stratified by flow (4 = 40 lpm)

The wing/cabin volume ratio varied widely with conditions. Most of the data was collected at 40 lpm (4's in the plot), for which there seems to be a relationship with altitude. Clearly, however, the flowrate through the internal FSSP impacts the ratio strongly, in ways we do not understand at this time. We cannot, therefore, consider this ratio to be a defendable test of the efficiency of the LTI.

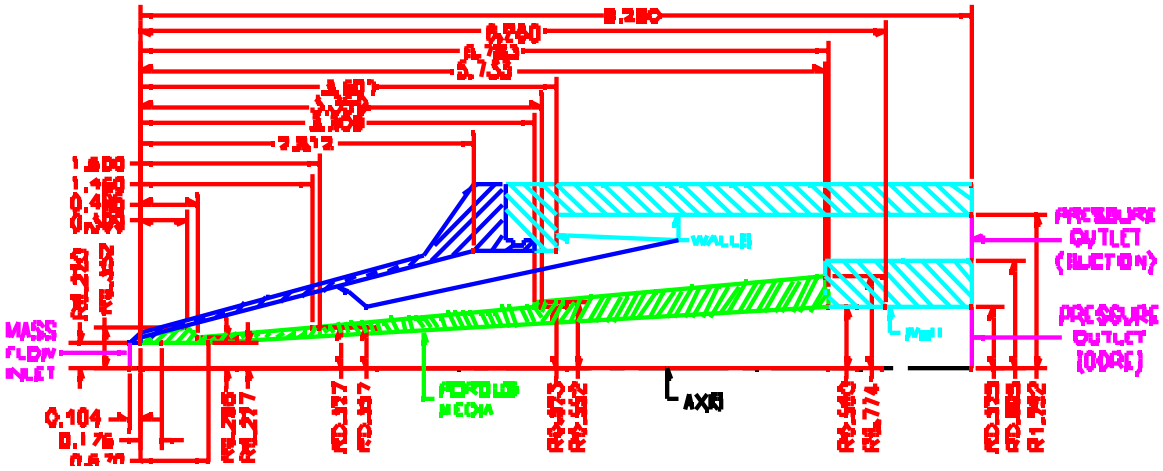

Figure 3.8.1. LTI Geometry and CFD Boundaries

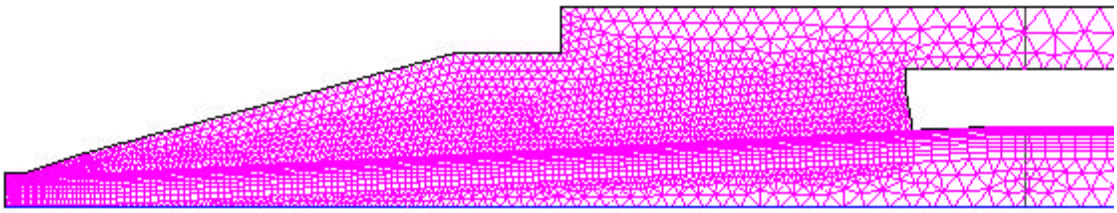

Figure 3.8.2. LTI Grid

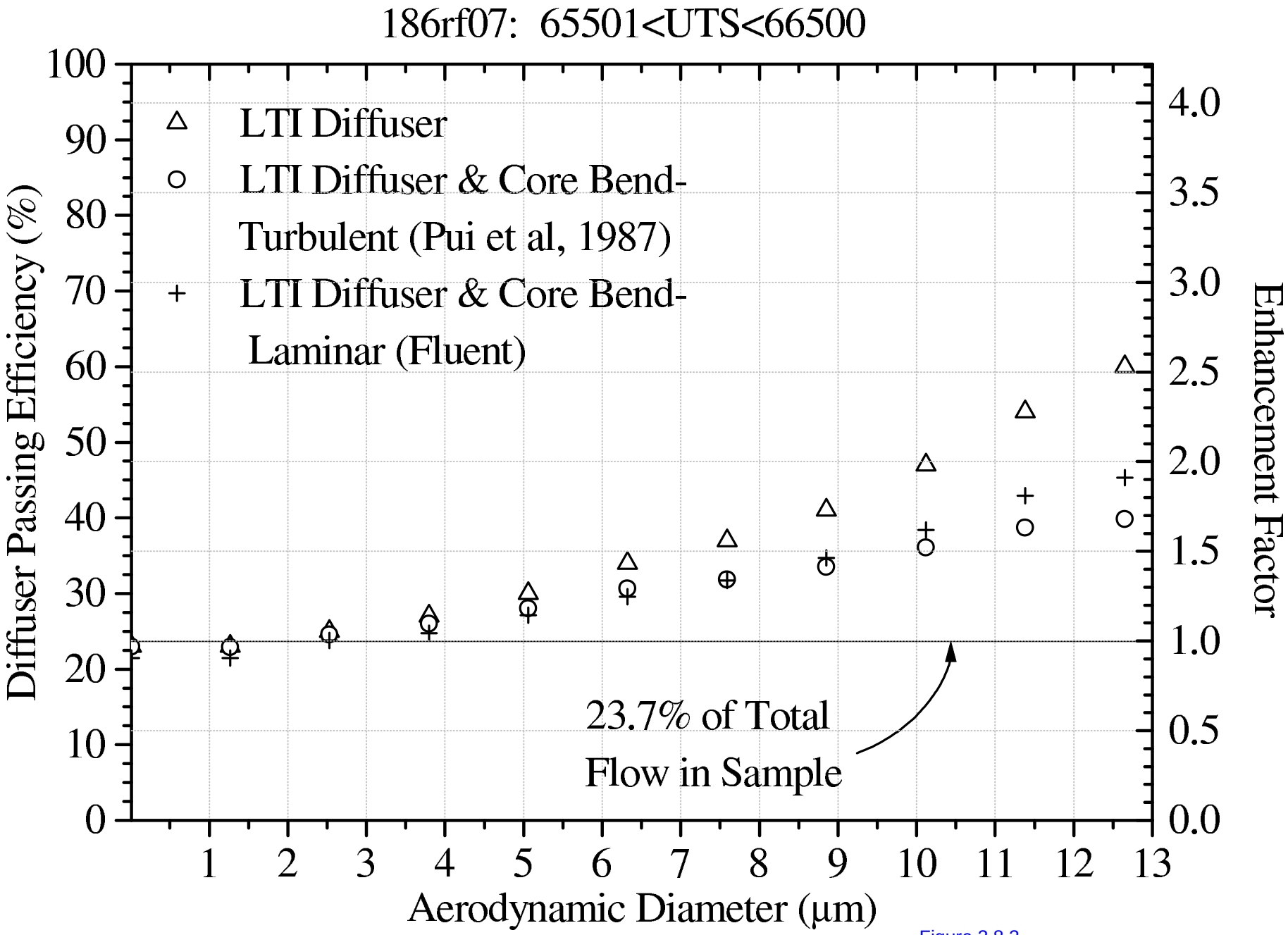
186rf07: 65501<UTS<66500
LTI Diffuser
LTI Diffuser & Core Bend-
Turbulent (Pui et al, 1987)
LTI Diffuser & Core Bend-
Laminar (Fluent)
23.7% of Total
Flow in Sample
Diffuser Passing Efficiency (%)
Enhancement Factor
Aerodynamic Diameter (µm)
0
10
20
30
40
50
60
70
80
90
100
0.0
0.5
1.0
1.5
2.0
2.5
3.0
3.5
4.0
1
2
3
4
5
6
7
8
9
10
11
12
13

Figure 3.8.3

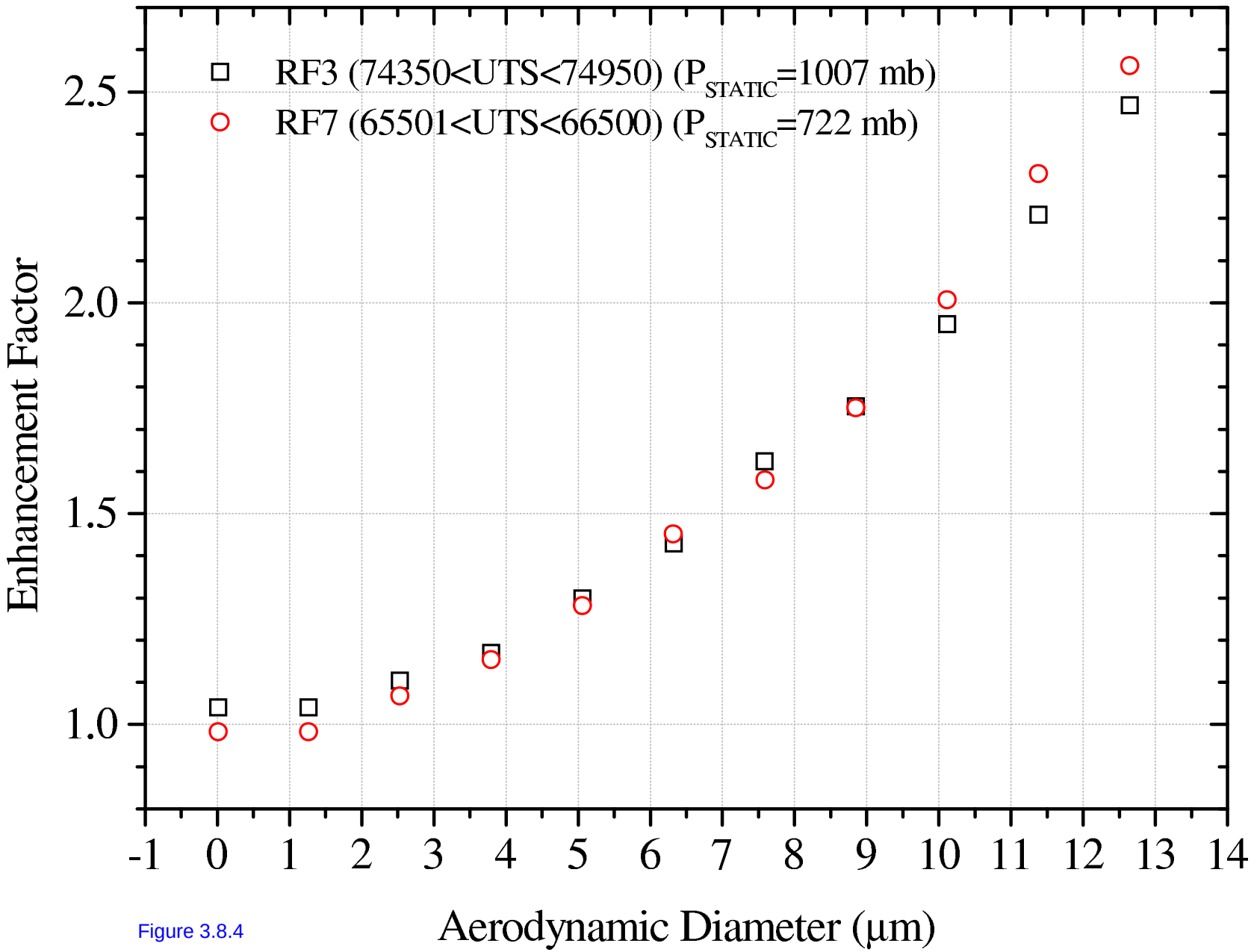
RF3 (74350<UTS<74950) (P_STATIC=1007 mb)
RF7 (65501<UTS<66500) (P_STATIC=722 mb)
Enhancement Factor
2.5
2.0
1.5
1.0
-1
0
1
2
3
4
5
6
7
8
9
10
11
12
13
14
Aerodynamic Diameter (µm)

Figure 3.8.4

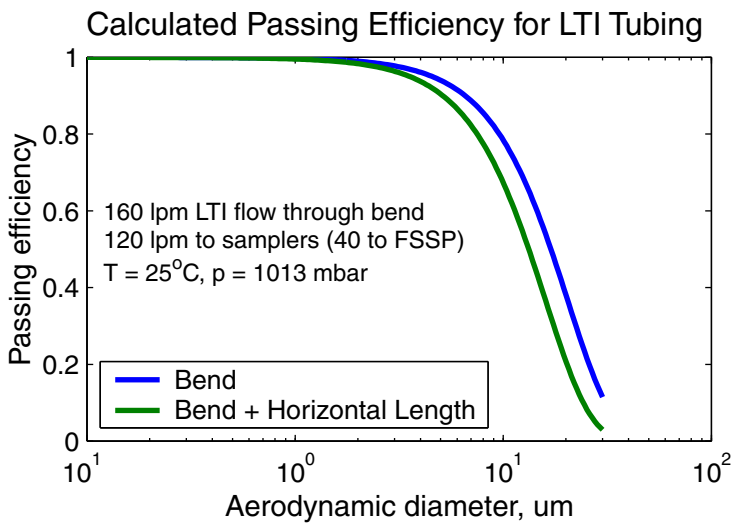

Figure 3.8.5 The difference between the two curves is the impact of sedimentation losses in the long transfer tube (Figure 2.3.5).

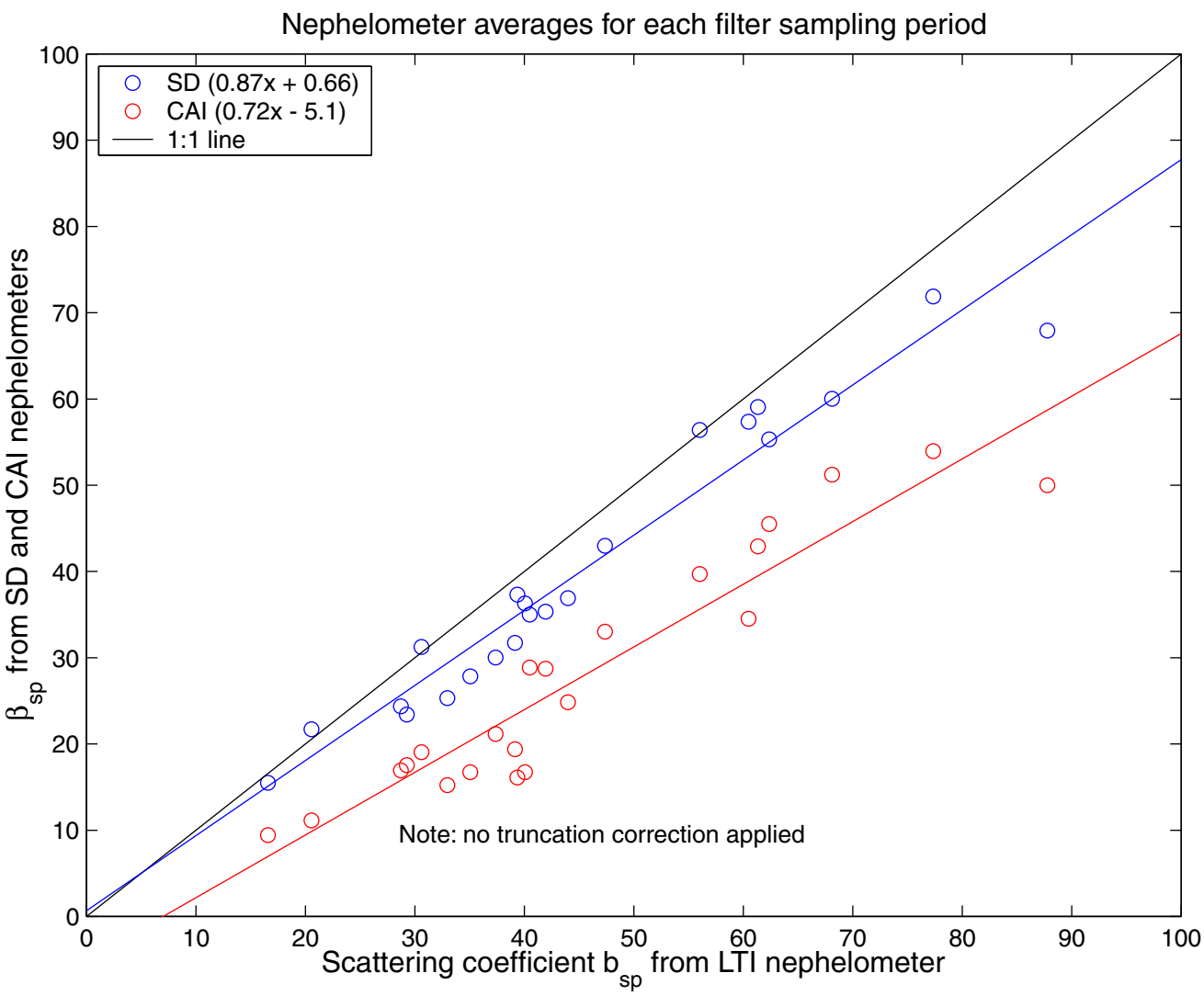

Figure 3.9.1 Comparison of nephelometers, corrected for common-inlet calibrations.

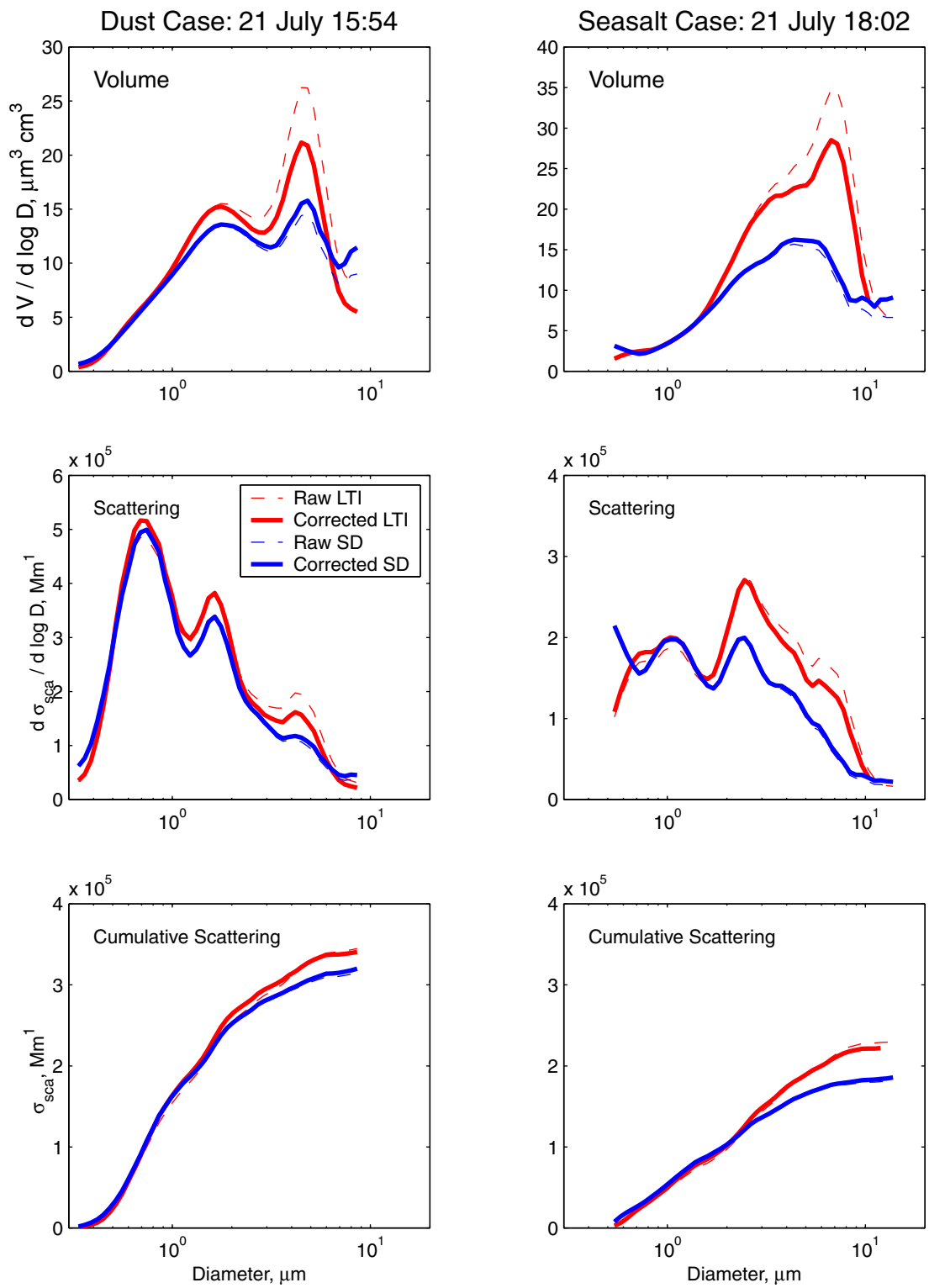

Figure 3.9.2. Accuracy of derived optical properties from the LTI and SD. The left panels are for a dry dust case, the right panels for a sea salt leg. The top panels show the best-guess corrections of both inlets for enhancement and tubing losses. The second panels use Mie theory to compute the scattering based on the size distributions and assumtions about the density and refractive indices of dust and sea salt. The bottom panels show the cumulative scattering. The leveling off at larger sizes is due to the fact that the mass scattering efficiency drops for larger particles, so they have little radiative impact.